MEASUREMENT OF THE TOPOLOGICAL BRANCHING RATIOS OF THE τ LEPTON USING THE OPAL DETECTOR AT LEP

James Edward Bloomer

Thesis submitted for the degree of
Doctor of Philosophy

School of Physics and Space Research
Faculty of Science
University of Birmingham

September 1997

Synopsis

Using data collected by the OPAL detector at LEP during the 1992 - 1995 physics runs, a sample of approximately 138000 $e^+e^- \to Z^0 \to \tau^+\tau^-$ decays were isolated. These decays were divided into two subsets by the angular region of the detector in which they were observed, denoted as the barrel region and the endcap region. The backgrounds for these selections were estimated initially from Monte Carlo and then checked using control samples obtained from the data. The relative inclusive decay rates to one, three and five charged particles ("prongs"), known as the topological branching ratios, B1, B3, B5 were calculated separately for each year. They were then combined in a weighted average to obtain a measurement for the two regions of the detector. These measurements are:

B1 = (84.59±0.10±0.14)%

B3 = (15.25±0.09±0.12)%

B5 = (0.164±0.026±0.047)%

for the barrel region and :

B1 = (84.69±0.17±0.27)%

B3 = (15.03±0.16±0.25)%

B5 = (0.259±0.047±0.042)%

for the endcap region.

These results are consistent with the measurement made by OPAL with data from the years 1990 and 1991, the separate three and five prong OPAL analysis using 1991-1994 data, and also the world averages. The results indicate that the "one

prong deficit" problem has been resolved and that there are no further significant problems in the tau sector.

The Author's Contribution

Due to the nature of the field of research present in this thesis the work was carried out within the OPAL collaboration. This collaboration consists of several hundred physicists and technicians, each with their own area of expertise. As a large number of people are necessary to maintain the experiment and perform the analysis it is often difficult to distinguish an individual's work. Therefore in this section I wish to highlight the contribution I have made to OPAL in the last three years.

The Birmingham University OPAL group is responsible for the maintenance and smooth running of the Muon Endcap subdetectors, which were built in conjunction with the Rutherford Appleton Laboratory. Whilst resident at CERN for a year I acted as Birmingham's representative for the endcap. This involved sharing the daily monitoring of checks of the gas and high voltage systems, attending weekly OPAL status meetings and responding to any problems from the pit at any time of the day or night, "thanks" to the "Beep".

During my first year at Birmingham I started working on my analysis of the topological branching ratios as part of the OPAL Tau working group. This analysis was further extended in my third year to include new data and the previously unexplored (for this measurement) endcap region. The working group met monthly whereupon I would present my progress, receive comments from other group members on my work and view their analyses. The analysis work presented in this thesis, although based on methods developed by the tau working group, was performed entirely independently.

Acknowledgements

I would like to thank Professors George Morrison, John Dowell and John Kinson for providing me with the opportunity to do this PhD and Doctor Mark Brummell without whom I would never have got the place. I would also like to thank the British Taxpayer for funding me during my three years, their funds were administered by PPARC. A big thank you to John Wilson who was always willing to answer all my questions and provide help and also to Pete Watkins whose help on my analysis was invaluable. Hal Evans and the tau working group also provided me with many ideas and answers to problems, and Jim Homer got me started on the whole thing and has been a great help throughout. I would also like to thank Laurie Lowe whose computer expertise and patience aided me greatly throughout my work. A big thank you must go to Michael Davis for persuading me that I really should do physics and that (in his own words) "computers are boring".

I would also like to give a very big thankyou to all my friends. You all know who you are and why I'm thanking you.

Thankyou as well to those people whom I have never met but have influenced my life profoundly, usually via inspiration and joy.

Finally and most importantly I would like to thank all my family for their love and support over the years. I would especially like to thank my "little" brother Jonathan who is the best musician I have ever met, and Mom and Dad whom I can never thank enough. Thankyou.

James, September 1997

This thesis is dedicated to Megan Elizabeth Studart and Hetty Beatrice Bloomer both of whom are sorely missed.

Karma police arrest this man he talks in maths....

Radiohead

We used to believe in invisible gods: now we put our faith in streams of electrons fizzing through spaces which are too small to see. Once again our understanding is handed over to the unperceivable, as if there is some fundamental need in humanity which requires the inexplicable to be at the heart of our lives, which requires that our destiny be shaped by intangible forces.

Spares, Michael Marshall Smith

Contents

List of Figures

List of Tables

Chapter 1

Introduction and Theory

1.1 Introduction

Man has always been driven to delve deeper and deeper into the structure of his surroundings in an attempt to understand the world that he lives in. Particle physics is responsible for providing models which describe the behaviour of matter on the smallest scales, and thus representing the furthest limit of our understanding of the structure of the universe. The beginning of these models was the discovery of the electron a hundred years ago, which was followed by the description of the nucleus and its constituent neutrons and protons. Our present day understanding of matter relies on experiments which have been conducted over the last 30 years. It is from these experiments that the Standard Model has evolved, which describes our world in terms of "elementary" particles known as quarks, leptons and gauge bosons.

1.2 Standard Model

The Standard Model [1] is the current theory of particle interaction on a small scale and describes the effect of the electromagnetic, weak and strong interactions on the fundamental particles. These particles can be divided into two groups, fermions and bosons. Fermions are the basic constituents of matter upon which the forces act and bosons are the gauge field quanta which mediate these forces. To avoid misunderstanding it should be emphasised that although the Standard Model is called a "model" it is in fact one of the most carefully verified mathematical theories there has ever been in science.

1.2.1 The Elementary Fermions

All fermions have spin $\frac{1}{2}$ and can be further divided into two categories, quarks and leptons. Both are assumed to be point-like particles in this theory and also, with the exception of neutrinos, all appear in nature as both right handed and left handed particles, (where a right handed particle is defined as having its spin and momentum vectors parallel and in left handed particles they are anti-parallel). Only left handed neutrinos are observed experimentally.

There are six variations, or *flavours*, of lepton, e, μ, τ and their respective neutrinos (ν_e, ν_μ, ν_τ). Three have an electric charge of one unit (e, μ, τ) and the three neutrinos are neutral.

There are also six *flavours* of quarks, *up, down, strange, charm, bottom* and *top.* The *charm, up* and *top* quark have a charge of $+\frac{2}{3}e$ while the *down, strange* and *bottom* quarks have a charge of -$\frac{1}{3}e$, where e is the charge of an electron. There is a further division within the quarks called "colour". This property of quarks, of which there are three types denoted by Red, Green and Blue, is treated as another quantum number. The theory of this colour charge is known as Quantum Chromodynamics (QCD) [2]. All of these quarks have been inferred by experiments in hadronic spectroscopy; no free quarks have been observed and they are not expected in QCD. Instead the quarks form bound colourless states known as baryons (qqq) and mesons ($q\bar{q}$). The observation of the top quark was only made recently [3].

Considering the properties of these fermions it seems sensible to group them together into generations (Table 1.1). It is not understood why there is more than one generation, but it is known that there are only three. The universe we live in today is composed entirely of the lightest generation of lepton. The heavier generations existed early in the life of the universe but as the universe cooled all these heavier particles decayed into the lighter ones. Hence the necessity for accelerators to create these particles for study.

Generations		
I	II	III
$\begin{pmatrix} u \\ d \end{pmatrix}$	$\begin{pmatrix} c \\ s \end{pmatrix}$	$\begin{pmatrix} t \\ b \end{pmatrix}$
$\begin{pmatrix} \nu_e \\ e^- \end{pmatrix}$	$\begin{pmatrix} \nu_\mu \\ \mu^- \end{pmatrix}$	$\begin{pmatrix} \nu_\tau \\ \tau^- \end{pmatrix}$

Table 1.1: The fermion generations.

More formally the quark doublets are written as

$$\begin{pmatrix} u \\ d' \end{pmatrix} \begin{pmatrix} c \\ s' \end{pmatrix} \begin{pmatrix} t \\ b' \end{pmatrix}$$

where (d', s', b') are the weak eigenstates obtained from the mass eigenstates by the following equation

$$\begin{pmatrix} d' \\ s' \\ b' \end{pmatrix} = V_{\rm CKM} \begin{pmatrix} d \\ s \\ b \end{pmatrix}$$

here V_{CKM} is the Cabibbo Kobayashi Maskawa (CKM) [4] matrix, its elements are measured experimentally and have the following values

$$\begin{pmatrix} |V_{ud}| & |V_{us}| & |V_{ub}| \\ |V_{cd}| & |V_{cs}| & |V_{cb}| \\ |V_{td}| & |V_{ts}| & |V_{tb}| \end{pmatrix} = \begin{pmatrix} 0.9745 \text{ to } 0.9757 & 0.218 \text{ to } 0.224 & 0.004 \text{ to } 0.014 \\ 0.219 \text{ to } 0.224 & 0.9736 \text{ to } 0.9750 & 0.034 \text{ to } 0.046 \\ 0.002 \text{ to } 0.005 & 0.036 \text{ to } 0.046 & 0.9989 \text{ to } 0.9993 \end{pmatrix}$$

It can be seen that the diagonal elements, $|V_{ud}|$, $|V_{cs}|$, $|V_{tb}|$ are clearly dominant. The high value of $|V_{cs}|$ reflects the experimental fact that charm particles prefer to decay into strange particles. Also the fact that $|V_{cb}|$ is greater than $|V_{ub}|$ reflects the fact that B mesons prefer to decay into charm particles. This matrix and its implications aided the search for the top quark as it was known that their experimental signature would be a cascade decay into the lighter quarks.

Each of the particles mentioned above also have anti particles which have the same mass as the particle but opposite charge and magnetic moment. Anti-particles were first described in theory by Dirac in 1928 [5] and have since been well investigated.

1.2.2 Gauge Bosons

In addition to the matter particles described in the previous section there are particles which transmit the fundamental forces. These particles are called bosons and have an integer spin. Since quantum field theory allows the calculation of the behaviour of the particles and this theory is a gauge theory these bosons are known as gauge bosons. The fermions interact by exchanging virtual gauge bosons and hence experiencing one of the four fundamental forces.

The force we are most familiar with everyday is gravity. This force is very weak compared to the other forces and can be neglected when considering elementary particles. It is however dominant on a large scale. The graviton is thought to be the gauge boson for gravity but it has not yet been discovered. Electromagnetism is the force that couples electric charges and the photon is the propagator. Because the photon is massless and has no charge electromagnetism has an infinite range. The theory which describes electromagnetism is called Quantum Electro Dynamics [6] and is the most accurate theory known at this time. The next force is known as the Weak force, this force couples to all fermions. The Weak force is mediated by two very massive gauge bosons, the W and the Z. Because of their high mass and therefore short lifespan (by the Uncertainty Principle [7]) the range of the force is limited to short distances. The Weak force and the Electromagnetic force have been united in the Electroweak theory, which elegantly describes both forces. Finally Quantum Chromodynamics is the theory which describes the interaction of the colour force, that is the force between quarks. This force is very strong and is mediated by the gluon. The gluon is massless but has a colour charge which means that it can interact with itself. This action limits the range of the force to very small distances and maybe responsible for quark confinement.

All Gauge bosons are assigned a spin of 1 in the Standard Model. The graviton which is not described by the Standard Model is assigned a spin of 2.

1.2.3 Gauge Field Theories

It is seen that the quantum mechanical description of experiments on charged particles can be made invariant under local phase (or "gauge") transformations on the particle wavefunction. This is done by introducing a long range field coupled to a charge and then making suitable simultaneous local gauge transformations of the electromagnetic potential. This is known as Quantum Electro Dynamics (QED) and is the simplest type of Gauge Theory. QED has successfully predicted electromagnetic interactions to a very high precision. The basis for all these gauge theories is that the theory should be invariant under local gauge transformations. The exact transformation depends on which gauge theory is being used. In QED it is the phase of the wavefunction that is allowed to change under a transformation of the U(1) group. In other words it should be possible to choose the phase of the wavefunction at each space-time point without affecting the physical measurement, by introducing a single gauge boson field - the photon.

The strong and weak interactions can also be described by gauge theories, however it is not as straightforward as QED due to the requirement of more complicated gauge transformations.

1.2.4 Renormalisation

The theories described, no matter how elegant, must be able to make predictions which experiments can then test. It is in the application of these theories to the real world that a problem occurs. The theory is applied using perturbative techniques, and in doing this divergent integrals are introduced. These integrals diverge due to infinity occurring in the calculations. It is the cancelling of these infinities in all physical observations, to make the theory calculable, which is known as renormalisation.

As an attempt to describe where these infinities come from one must consider how the calculations are made, and it is helpful to look at the Feynman diagrams for the process. Feynman was one of the architects of QED and his diagrams not only help visualise interactions but are an important tool for calculations. In considering a simple QED scattering process we can look at the vertex of an electron and photon. The zeroth order vertex and the first order correction (1.1 (a) and (b)) can both be calculated and compared to results from precise scattering experiments. The problem occurs at second order effects as shown in figure 1.1 (c) and (d), it can be seen that the virtual photon is entirely internal to one of the lines in the diagram. The momenta of this internal line is free and so has to be integrated over an infinite range, and these integrals are found to diverge.

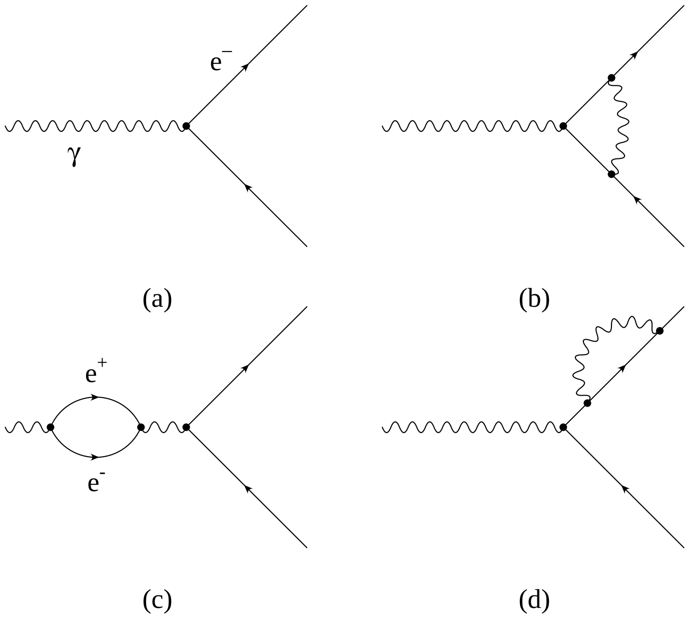

Figure 1.1: The Feynman diagrams for the $\gamma - e^-$ scattering process. Diagram (a) shows the basic zeroth order process and diagram (b) shows the first order correction. The processes shown in (c) and (d) cause the integrals in the amplitude calculations to become divergent.

To overcome these problems the divergences are absorbed into the fermion lines at the cost of introducing a finite number of arbitrary parameters, charge, mass and so on, which can then be calculated from experiment. Now for an electron there must be some "bare charge" which is shielded by the higher order processes. As the energy of the probe used to examine the electron is increased then the closer it will get to the "bare charge" and therefore feels a stronger electromagnetic force. This is in fact exactly what is seen in experiments with the coupling constant α varying from $\approx 1/137$ at $Q^2 = M_e^2$ to $\approx 1/128$ at $Q^2 = M_Z^2$. Due to the range in values of α it is known as a "running" coupling constant.

A theory is said to be renormalisable if the predicted amplitudes for physical processes remain finite at all energies, at the cost of adding arbitrary parameters as mentioned. It can be proved that all Gauge Theories in the Standard Model can be renormalised [8].

1.2.5 Electroweak Theory

In the 1960's Weinberg and Salam showed that Electromagnetic interactions and weak interactions could be combined into one gauge theory [9].

Due to the parity violating nature of the weak interaction the particles are divided into left handed doublets and right handed singlets.

$$\begin{pmatrix} \nu_e \\ e \end{pmatrix}_L \begin{pmatrix} u \\ d \end{pmatrix}_L \quad e_R \quad u_R \quad d_R$$

These left handed doublets can be transformed by the $SU(2)_L$ transformation [1]. To compensate for these local changes three fields need to be introduced, a neutral, positive and negative field. The charged fields can be linked directly to the $W^\pm$ bosons.

The $SU(2)_L$ transformation cannot describe neutral currents on its own as it is known that these currents contain both left and right handed particles. Therefore to transform the singlets one needs to introduce the $U(1)_Y$ transformation where Y is the hypercharge defined by :

$$Q = T^3 + \frac{Y}{2} \tag{1.1}$$

where Q is the charge and T^3 is the third component of the weak isospin *i.e.*0 for singlets and $\pm\frac{1}{2}$ for doublets. The neutral currents can then be formed by combining $SU(2)_L$ and $U(1)_Y$ and correspond to the Z^0 and γ which are given by :

$$\mathrm{Z}^0 = W_3 cos\theta_W - B sin\theta_W \tag{1.2}$$

$$A = W_3 sin\theta_W + B cos\theta_W \tag{1.3}$$

where W_3 is the neutral weak isospin field, B is the weak hypercharge field and θ_W is the weak mixing angle, sometimes known as the Weinberg angle, and describes the mixing of the fields.

This theory predicts the two charged bosons $W^\pm$ and the two neutral bosons Z^0 and γ. However the theory predicts them to be massless. This area was where Weinberg and Salaam made the breakthrough on the theory, which was originally postulated by Glashow in 1961 [10]. To overcome this problem they incorporated the *Higgs mechanism* [11] to “give” mass to the bosons and maintain the symmetry. The expense of this mass is that another massive, neutral, scalar boson must exist, known as the Higgs boson. The model predicts the behaviour of the Higgs boson with regard to its couplings to the fermions and other bosons but it does not predict its mass. The Higgs boson has not been identified at present although limits on its mass are in place from studies on its couplings to the W and Z bosons. The current limits on the mass of the Higgs are 465 GeV$> M_H >$ 77GeV [12]. The Higgs boson remains one of the last areas of the Standard model unverified.

1.2.6 Boson couplings and Parity Violation

To aid in the understanding of the physical processes it is useful to use Feynman graphs to describe them in a visual manner. These graphs demonstrate the coupling of the bosons to the fermions and the four most important electroweak couplings, $W^\pm$, Z^0 and γ are shown in figure 1.2. In the coupling to the $W^\pm$ the term $(1-\gamma^5)$

projects out the left handed components of the fermions, hence excluding any interaction with the right hand components of the fermions. This describes mathematically the "V-A" interaction and produces parity violation in weak decays via the $W^{\pm}$.

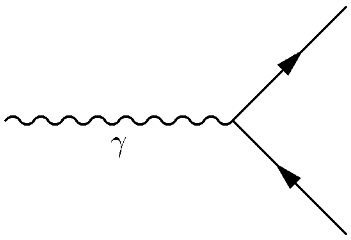

Vertex factor is $ieQ_f\gamma_\mu$

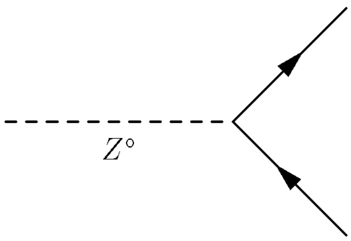

Vertex factor is $ig\gamma_\mu(C_V^f - C_A^f\gamma_5)\frac{1}{2cos\theta_W}$

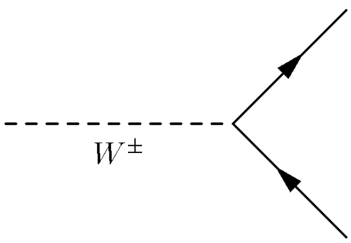

Vertex factor is $ig\gamma_\mu(1-\gamma_5)\frac{1}{2\sqrt{2}}$

Figure 1.2: Coupling terms for the electro-weak gauge bosons to fermions.

As can be seen from figure 1.2 the coupling to the Z^0 is more complex due to different couplings to the left and right handed components. This can be seen more clearly if the equation is split into these parts which act on the left and right handed components:

$$\gamma_\mu(C_V^f - C_A^f\gamma^5) \equiv \frac{1}{2}(C_V^f - C_A^f)\gamma_\mu(1+\gamma^5) + \frac{1}{2}(C_V^f + C_A^f)\gamma_\mu(1-\gamma^5) \quad (1.4)$$

where the coupling factors are :

$$C_V^f = T_3^f - 2Q_f sin^2\theta_W \quad (1.5)$$

$$C_A^f = T_3^f \quad (1.6)$$

Q_f is the charge of the fermion and T_3^f is the third component of the weak isospin. The value of these parameters are summarised in table 1.2 for the leptons and quarks. For a neutrino the term $C_V^f - C_A^f$ is zero predicting that right handed neutrinos will not interact, and are therefore not seen in nature. For a charged fermion the Z^0 couples to both left and right handed components. However for charged leptons the values of C_A^f and C_V^f are very similar producing parity violating effects such as the tau polarisation (see chapter 3).

f	Q_f	C_A^f	C_V^f
ν_e, ν_μ,..	0	$\frac{1}{2}$	$\frac{1}{2}$
e^-, μ^-,..	-1	$-\frac{1}{2}$	$-\frac{1}{2} + 2sin^2\theta_W \approx -0.03$
u, c,..	$\frac{2}{3}$	$\frac{1}{2}$	$\frac{1}{2} - \frac{4}{3}sin^2\theta_W \approx 0.19$
d, s,..	$-\frac{1}{3}$	$-\frac{1}{2}$	$-\frac{1}{2} + \frac{2}{3}sin^2\theta_W \approx -0.34$

Table 1.2: Summary of the Z^0 to fermion vertex factors

1.3 Physics at LEP

An excellent test of the Standard Model can be made at LEP where electrons and positrons are collided together at energies close to or on Z^0 peak. Below the Z^0 peak the interactions involved in the annihilation are predominantly electromagnetic and mediated by the photon. This shifts however to interactions mediated by the Z^0 when near or on the peak. The Z^0 bosons produced at LEP decay into fermion and anti-fermion pairs, with the combined products of the decay being neutral due to charge conservation, as follows:

$$e^+e^- \to Z^0 \to \ell\bar{\ell}$$
$$e^+e^- \to Z^0 \to q\bar{q}$$

Over the six years that LEP ran on the Z^0 peak many of the electroweak parameters were measured to a great accuracy. The results were often enhanced by the fact that LEP contains 4 detectors, obtaining independent results. These results are not only a good cross check but also they can often be combined, increasing the accuracy of the measurement. Table 1.3 shows a list containing some of these parameters, the current world average values and a comparison to the standard model values. It can be seen that there is extremely good agreement between the measured experimental values and the values predicted by the Standard Model theory.

Quantity	Measured Value	Standard Model Value
Mass of Z^0 , M_Z (GeV)	91.1884±0.0022	Input
Total Width of Z^0 Γ_Z (GeV)	2.4963±0.0032	2.497±0.001±0.002
Hadronic Pole Cross section, σ_{had} (nb)	41.488±0.078	41.45±0.002±0.004
Partial width to hadrons of Z^0 Γ_{had} (MeV)	1744.8±3.0	1743.8±0.2±1.2
Partial width to leptons of Z^0 Γ_l (MeV)	83.93±0.14	83.97±0.01±0.06

Table 1.3: Summary of electroweak parameters measured by experiment compared to the standard model calculation values.

Chapter 2

The Detector

To make a detailed study of the electro-weak interaction the W and Z particles must be investigated. It was for this purpose that the Large Electron Positron collider (LEP) was built at CERN [13].

2.1 The LEP Collider

The LEP collider (figure 2.1) is a (roughly) circular tunnel lying on average 100m underground under the French-Swiss border. Its circumference is 27km making it the biggest piece of scientific equipment in the world. The collider is a synchrotron which collides bunches of electrons and positrons with each other by circulating them in opposite directions in the same vacuum pipe. These collisions are examined at four interaction points at which the four LEP detectors are built: OPAL [14], ALEPH [15], DELPHI [16] and L3 [17]. The OPAL detector will be discussed in detail later in this chapter. The centre of mass energy of the collisions is designed to range from 80 GeV to around 200 GeV. To achieve this LEP running has been split into two main phases LEP1 and LEP2, LEP1 has an interaction energy straddling the Z^0 peak. It has been run with the interaction energy equal to that of the Z^0 peak and has also run with the interaction energy equal to approximately $\pm$ 2GeV of the peak. This "scanning" across the Z^0 peak was carried out during the 1991, 1993 and 1995 data collection. LEP2 which was first operable in 1996, has run at a higher energy (161 and 174 GeV) which is above the threshold for producing Z^0 and also W^+W^- pairs. LEP2 is presently running at 183 GeV. During 1995 LEP also ran at an intermediary stage known as LEP1.5. This served as a test of the equipment needed for LEP2 but also provided an opportunity to search for any new particles [18]. All data used in this analysis were obtained during the running of LEP1.

2.1.1 The Injection System

Before the electrons and positrons enter LEP they first go through a series of pre-accelerators to get them to a sufficiently high energy such that LEP can accelerate the particles to the target energy. Firstly comes the LEP Injector Linac (LIL). This uses a heated filament to produce electrons by thermionic emission. These electrons are accelerated at 200 MeV toward a tungsten target. The electrons are then decelerated and bremsstrahlung emission causes an electron-positron pair to be created. The electrons and positrons are then separated and stored in the Electron Positron Accumulator (EPA) at 600 MeV. When sufficient numbers of each particle are attained they are injected into the Proton Synchrotron (PS) and accelerated to 3.5 GeV. Then they are injected into the Super Proton Synchrotron (SPS) and accelerated up to 20 GeV. Finally they are injected into LEP and accelerated up to full interaction energy.

2.1.2 The Accelerating System

As an accelerating charged particle loses energy ($\Delta E \sim \frac{E^4}{R}$ where E is the beam energy and R is the radius of the accelerator) some system is needed to replace this energy. The radio frequency cavities (RF) serve this purpose. LEP1 had 128 copper RF cavities powered by 16 1MW klystrons. The power consumption of the accelerating system can be approximated from the following. There are four bunches of electrons and four bunches of positrons (eight bunches of both from 1994), the average number of particles per bunch being 10^{11}. At the Z peak the average energy loss due to synchrotron radiation is 250 MeV per electron (or positron) per cycle producing a power demand of approximately 10^6W. As the energy to which the particles are accelerated is increased this power demand increases rapidly, hence most of the RF cavities have now been replaced for LEP2 with more efficient superconducting RF cavitities (there are now 52 copper cavities and 240 superconducting cavities).

2.1.3 The Beam Transport System

It is clearly advantageous to maintain the circulating beams for as great a period of time as possible. This will allow a larger number of possible interactions to take place before another batch of particles need to be injected. To do this the beam pipes are lowered to a pressure less than 3×10^{-9} torr. To keep the beams in the (roughly) circular orbit of LEP over 3000 bending (dipole) magnets and 2000 focusing(quadrupole) magnets are used.

2.2 The OPAL detector

Around the LEP ring there are four interaction points which are used[a] for the collision of electrons and positrons. At each of these interaction points there are large detectors of which OPAL (Omni Purpose Apparatus for LEP) is one. OPAL is a multipurpose apparatus which has been designed to detect all types of interactions occurring in e^+e^- collisions (except for $\nu\bar{\nu}$ final states). The apparatus aims to reconstruct these events accurately and classify them unambiguously by providing precise measurements of charged particles and electromagnetic energy.

To cover most of the 4π solid angle around the interaction vertex, and detect as many of the emerging particles as possible, the detector was designed as a series of concentric cylinders, with the ends sealed by endcap detectors. These layers of detector form individual "sub-detectors" which are each designed for a specific task.

The beam pipe runs directly through the centre of the detector. Moving outward from the interaction point one first meets the vertex detectors which are designed to identify very short lived particles (eg. τ, charmed and bottom particles) that decay

[a]There are in fact eight intersection points around the LEP ring but the beams are separated vertically at the odd intersections

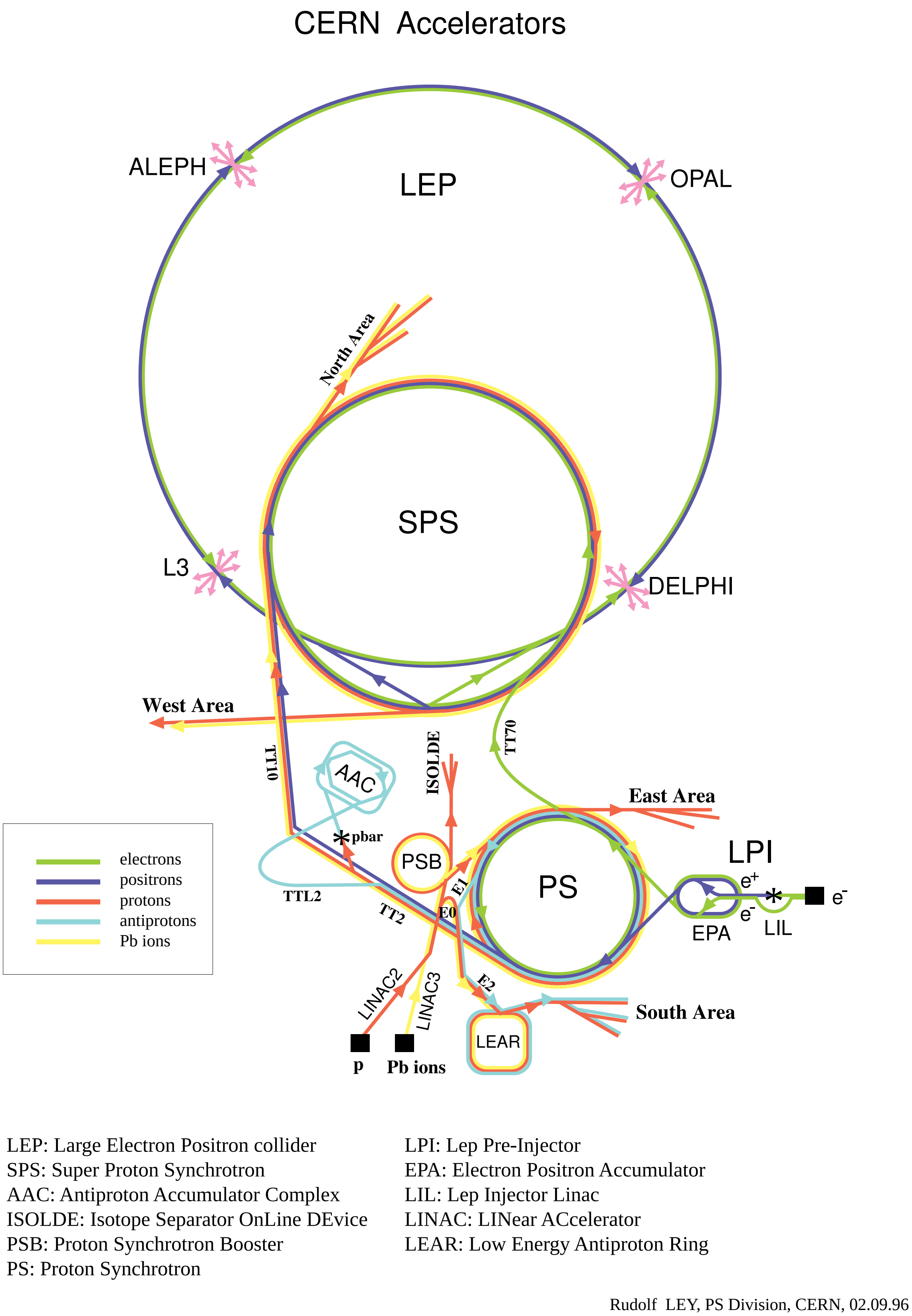

Figure 2.1: The LEP injection and Acceleration system. The AAC and LEAR are now closed.

within a small distance of the interaction point. Next are the tracking chambers which lie within an applied solenoidal magnetic field, parallel to the beam direction. These chambers allow measurements of the charged particle directions, momenta, and through their energy loss, dE/dx, the identification of particles. Outwards from the tracking chambers are the calorimeters which cause particles, neutral or charged, to interact and produce showers of secondary particles. The resulting shower direction and energy provides a measure of the momentum of the incident particle. The first of these calorimeters is the electromagnetic calorimeter which is specifically designed to absorb and measure the energy of photons and electrons. After emerging from the electromagnetic calorimeter particles reach the hadronic calorimeter. The hadronic calorimeter absorbs and measures the energy of hadrons entering it. Finally particles reach the muon chambers which specifically detect muons since they pass through the rest of the detector with little interaction.

The following sections describe in detail the various subdetectors. A perspective view and a cross-section of the OPAL detector are shown in figures 2.2 and 2.3.

In describing the subdetectors the OPAL coordinate system is referred to for ease. The main coordinate system is the right handed Cartesian system, with the origin defined as the centre of the the jet chamber, approximately the e^+e^- interaction point. The z axis is defined by the direction of the electron beam passing through OPAL, with the x axis pointing towards the centre of the LEP ring and the y axis being approximately vertical. It is only approximately vertical because the LEP ring is inclined at 0.8° to the horizontal. Another system frequently used however is the spherical polar co-ordinate system (r, θ, ϕ), as seen in the previous figure (2.2). The azimuthal angle ϕ is measured about the z axis with the positive x axis defining ϕ=0. The polar angle θ is measured from the positive z axis and finally r is the spherical radius from the origin.

2.2.1 Central Tracking Detector

The Central Detector consists of a Silicon Microvertex detector and three drift chamber devices, the vertex detector, jet chamber and surrounding Z-chambers. The drift chambers are situated inside a pressure vessel at 4 bar which is positioned between

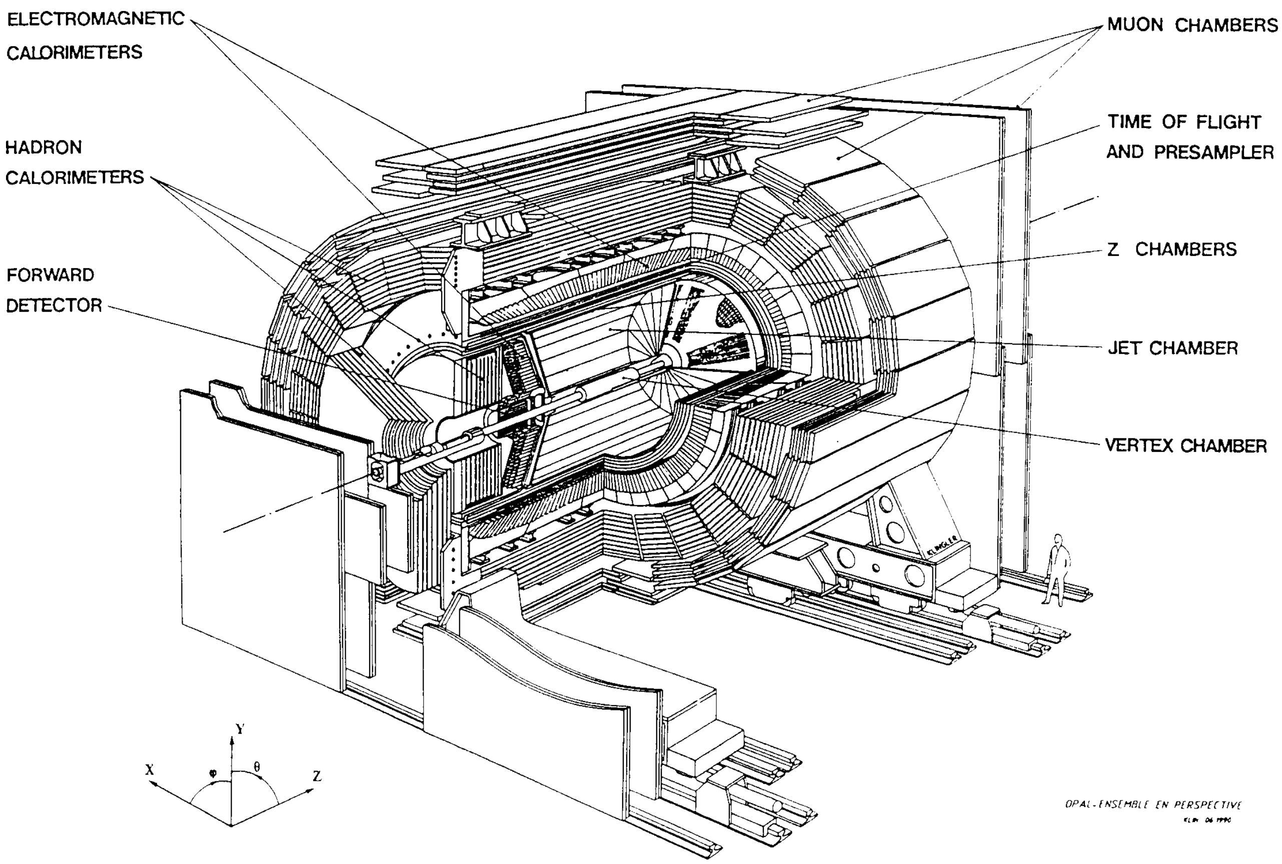

Figure 2.2: A perspective view of the OPAL detector

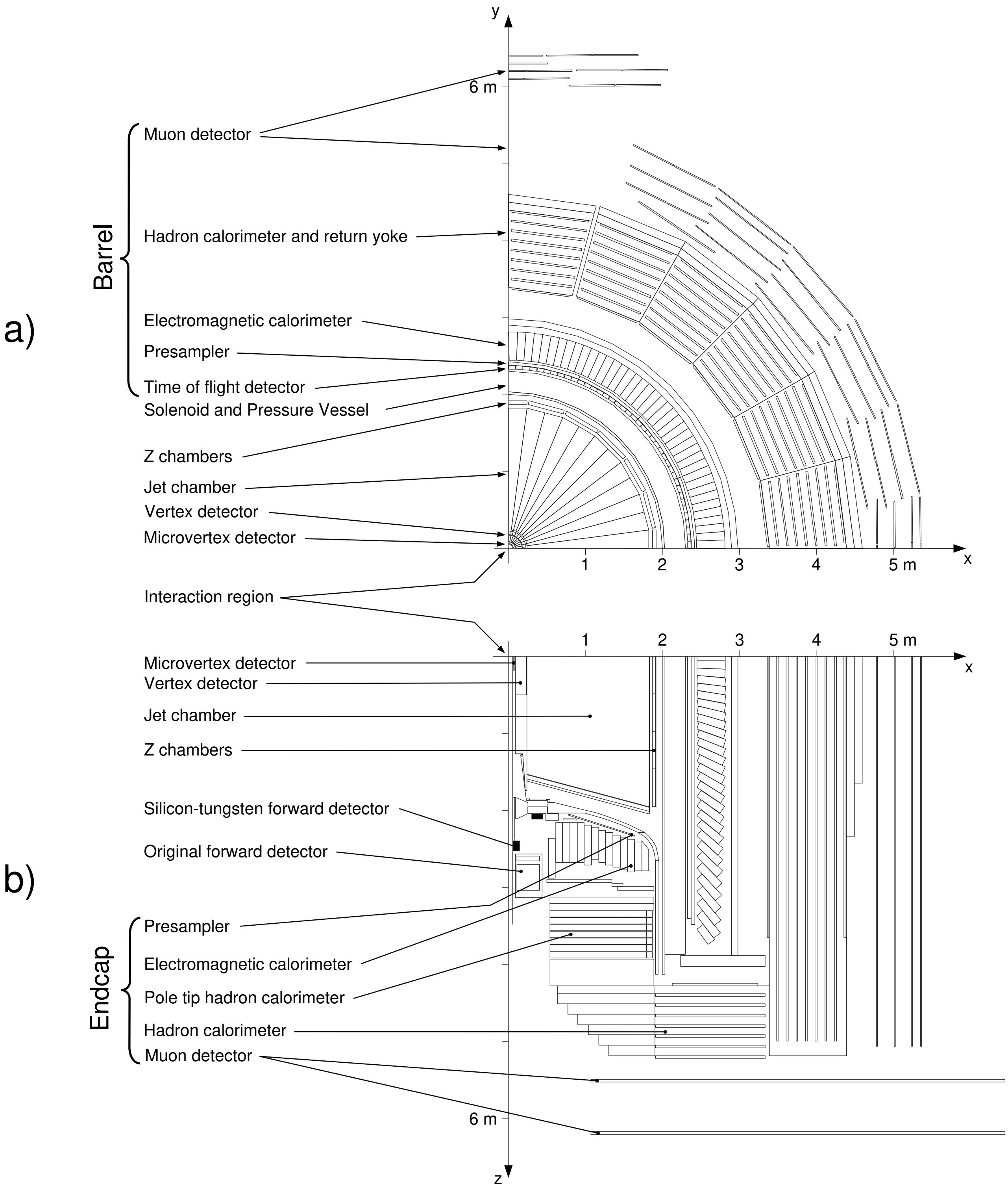

Figure 2.3: Cross section of the OPAL detector

the Silicon Microvertex detector and the magnet coil.

Silicon Microvertex Detector

The Silicon Microvertex Detector(SI) [19] was installed originally in 1991 and upgraded in 1993 to measure r-z coordinates as well as the original r-ϕ coordinates. It consists of two concentric cylinders of double sided silicon with diameters 12cm and 15cm (Fig 2.4 and Fig 2.5). The inner layer consists of 11 "ladders" and the outer of 14. Each ladder is 18cm long and consists of 3 silicon wafers daisy chained together. The spatial resolution is 5-10 microns in r-ϕ as its main purpose is measuring the impact parameter and reconstructing vertices. The impact parameter is defined as the distance from the point of closest approach of the track to the origin of the coordinate system. A vertex is the point from which two or more tracks appear to emanate.

For 1995, the detector was further upgraded. The number of ladders was increased to 12 and 15 and the ladders tilted to close gaps. The outer layer was also extended from 3 to 5 wafers by the addition of a layer of 2 wafer ladders at the -z end. The interaction point was still at the centre of the 3 ladder detector.

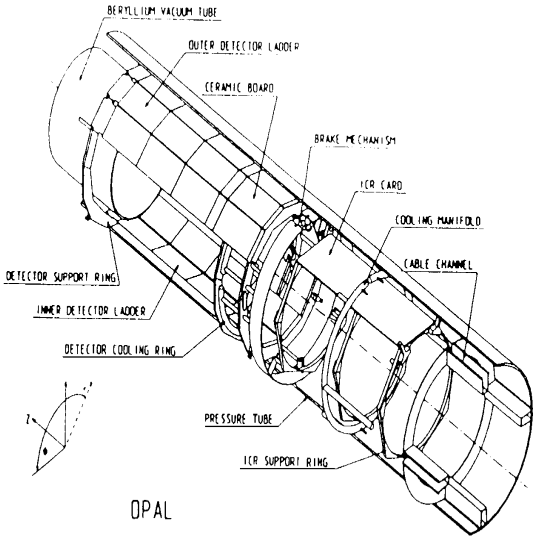

Figure 2.4: Cut off diagram of Si detector

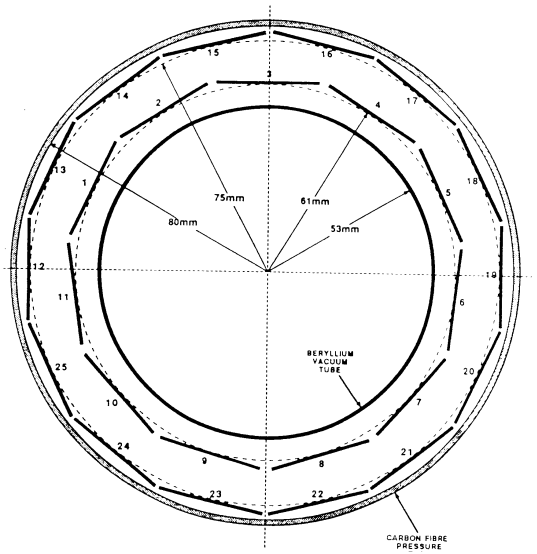

Figure 2.5: Layout diagram of the original Si detector installed in 1991.

Vertex Detector (CV)

The vertex detector (CV) is a high precision cylindrical jet drift chamber. It is 100cm long with a radius of 23.5cm and consists of two parts, one with a small radius and the other with a larger radius, each divided into 36 sectors in azimuth. The inner layer contains the axial sectors, each containing a plane of 12 sense wires strung parallel to the beam direction. The wires range radially from 10.3 to 16.2cm with a spacing of 0.583 cm. The outer layer contains the stereo sectors each containing a plane of 6 sense wires, inclined at an angle of $\pm 4°$ to the beam axis (Fig 2.6) . The stereo wires lie between the radii 18.8 and 21.3cm with a spacing of 0.5 cm.

A precise measurement of the drift time on to the axial sector sense wires allows the position to be calculated. The resolution obtained in r-ϕ is 55μm. Measuring the time difference between signals at either end of the sense wires allows a fast but relatively coarse z coordinate that is used by the OPAL track trigger and in pattern recognition. A more precise z measurement is then made by combining axial and stereo drift time information offline.

Jet Chamber (CJ)

This is a cylindrical jet chamber [20] 4m long with an outer diameter of 3.7m and an inner diameter of 0.5m and is divided into 24 identical azimuthal sectors. Planes of cathode wires mark the boundaries between the sectors and are inclined at 7.5° to the anode planes which run down the centre of the sectors. All wires are parallel to the beam direction (and therefore the cylinder axis) and the wire planes are radial. The anode planes consist of 159 sense wires which are each separated by potential wires. The signal wires are each offset from the potential wires by $100\mu m$ transversely, the direction of the offset alternates between the left and right of the potential wire. These offsets allow the chamber to identify which side of the anode plane the particle track is.

In the range $43° < \theta < 137°$ CJ measures 159 points along each track, and at least 8 points on a track are obtained over a solid angle of 98% of 4π.

It is this section of the detector which allows much information about the passing particle to be learned. Firstly the particles ionise the gas mixture in the chambers,

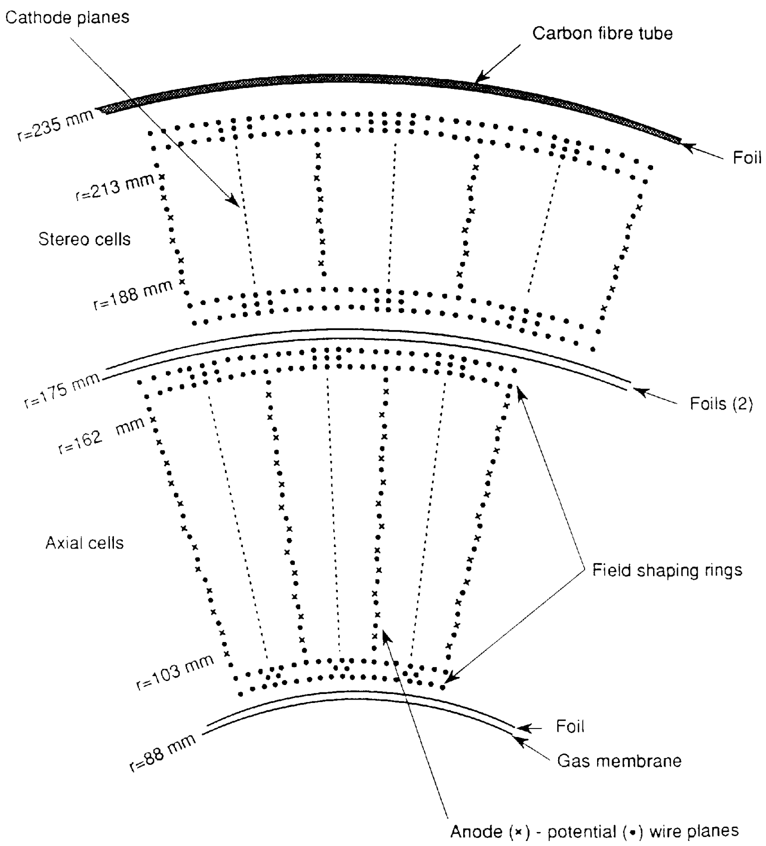

Figure 2.6: Layout diagram of CV detector

then the time taken for the electrons to drift to the wire gives a position in the r-ϕ plane. Secondly the quantity of charge reaching each end of the wire allows determination of the z coordinate and finally the total charge received by the wire allows the rate of loss of energy dE/dx to be determined. The quantity dE/dx is an important variable used for identifying particles, particularly for discriminating between charged hadrons. Full details of the particle identification method can be found in [21] but a quick summary follows.

Firstly the pulse shapes are recorded at both ends of the sense wires and are digitised by FADCs. After correcting for the nonlinearity of the electronics the pulses are integrated and then gas and electronic gain are corrected for. Next the 30% highest charges associated with each particle track are discarded. This truncated mean method eliminates the sample with the largest energy loss which are those due to hard collisions. Finally the charges of both wires ends are added together giving the total signal per charge wire ie. the differential energy loss per sample. The resolution of the dE/dx identification can be seen in figure 2.7.

The detector provides an average resolution in r-ϕ of 135 μm at a mean drift distance of 7cm and an average resolution in z of 6cm.

Z chambers(CZ)

The Z-chambers [22] provide a precise measurement of the z coordinate of tracks as they leave the jet chamber. They consist of a barrel region around CJ covering a polar angle from 44°to 136°and covering 96% of the azimuthal range. It is constructed of 24 drift chambers, 4m long, 50cm wide and 59mm thick. Each chamber is split lengthwise into eight sections and to achieve a good z coordinate resolution each section has 6 anode wires at right angles to the beam axis. The resolution of the z coordinate achieved is around 300μm.

The Magnet

The central detector is inside a solenoid supplying a uniform (to $\pm 0.5\%$) axial magnetic field of 0.435T. The magnet consists of a water cooled aluminium/epoxy solenoid coil ($\simeq 1.7 X_0$ where X_0 is the radiation length) inside an iron yoke con-

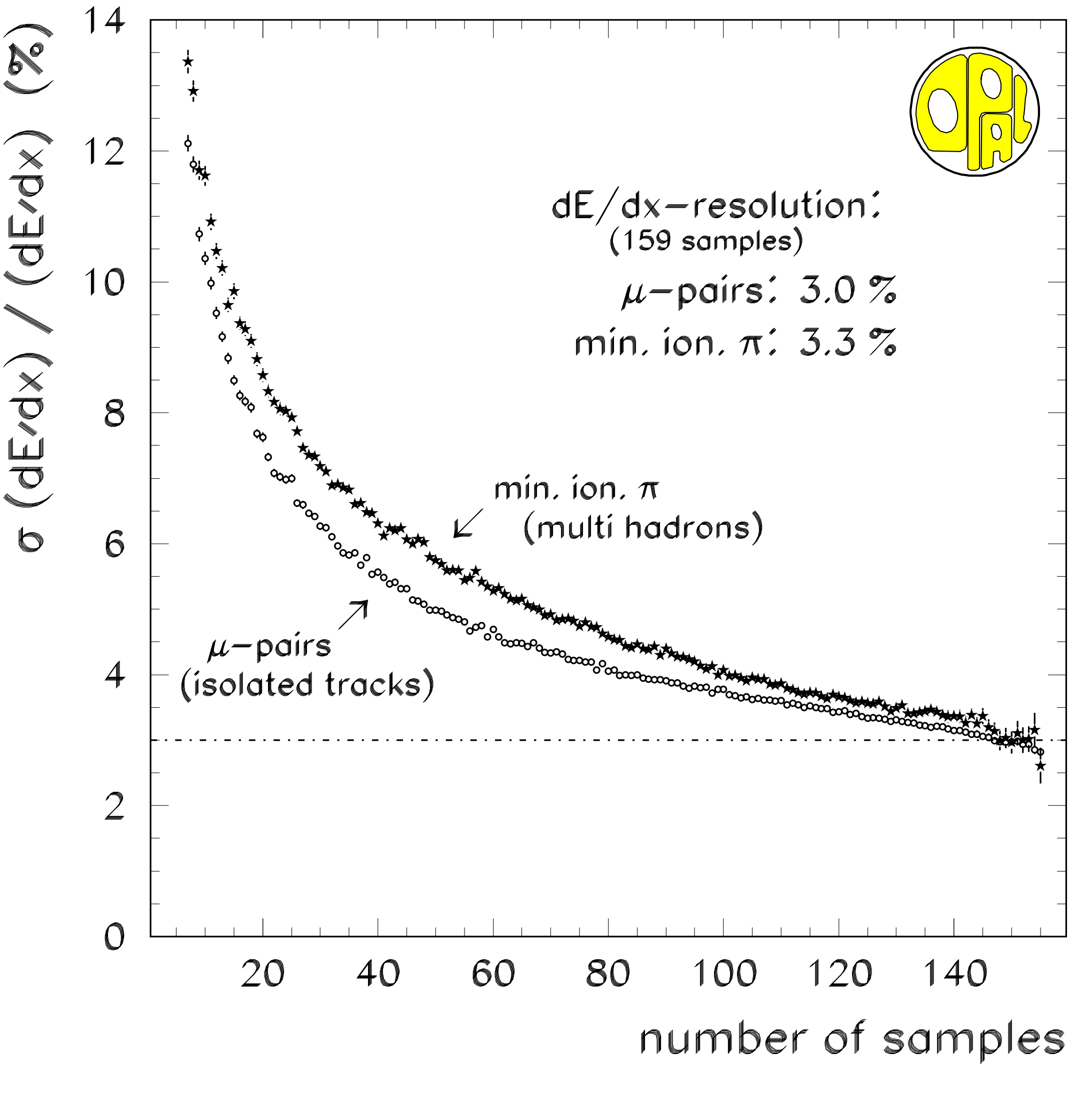

Figure 2.7: The dE/dx resolution for muon-pairs (isolated tracks) and for minimum ionising pions (p = 0.4 - 0.6 GeV/c) within multihadrons (dense track environment) as function of the number of dE/dx hits. The dotted line represents the best resolution of 3.0%.

structed from soft steel plates. The iron also acts as showering material for the subsequent hadron calorimeter. To produce the required magnetic field a current of 7000A is used, approximately 5MW of power is consumed. The coil was wound as one unit to reduce the residual field outside the coil to a few mT.

2.2.2 Time Of Flight (TOF)

The Barrel time-of-flight (TB) system provides charged particle identification in the range 0.6 to 2.5 GeV, fast triggering information and an effective rejection of cosmic rays. It consists of 160 scintillation counters forming a barrel layer 684cm long at a mean radius of 236cm surrounding the OPAL coil covering the polar angle range $|cos\theta| < 0.82$

In 1996 the Tile Endcap (TE) system was added to enhance the triggering information available from the forward region, and to identify which bunches in a bunch train are responsible for a particular observed collision. It consists of a 10mm thick scintillator layer, between the endcap presampler and the endcap electromagnetic calorimeter (EE), divided into tiles and read out using embedded wavelength-shifting fibres.

2.2.3 Electromagnetic Detector

The function of the electromagnetic calorimeter [23] is to detect and identify electrons and photons. It consists of a lead glass total absorption calorimeter split into a barrel and two end cap arrays. This arrangement together with two forward lead scintillator calorimeters of the forward detector makes the OPAL acceptance for electron and photon detection almost 99% of the solid angle.

Presampler

A presampler [24] is needed because there is a substantial amount of material in front of the lead glass calorimeter (mostly due to the solenoid and pressure vessel) and most showers start to develop before entering the lead glass. Therefore the presampler measures the position and energy before the calorimeter. It consists of a cylinder of limited streamer mode chambers. In the barrel there are 16 chambers in total at a total radius of 2.39m and a length along the beam pipe of 6.62m. Each chamber has two layers of streamer mode chambers with the wires running axially. The endcap region uses narrow-gap multiwire proportional chambers instead of the limited streamer mode chambers due to a lack of space. The total angular coverage is $|cos\theta| < 0.95$.

Electromagnetic Calorimeter (ECAL)

The function of this is to measure accurately the position and energy deposited by electrons and photons. To do this 9440 lead glass blocks are used in a cylindrical array with the endcaps being covered by domes of 1132 lead glass arrays. In the barrel the blocks have a cross section of $\sim 10 \times \sim 10\text{cm}^2$ and a depth of 37 cm. In the endcap there are three different depths of block 38cm, 42cm and 52cm, with the cross section being approximately the same as in the barrel .

In order to maximise detection efficiency the longitudinal axis of each block is angled to point at the interaction region. The focus of this pointing geometry is slightly offset from the collision point in order to reduce particle losses in the gaps between blocks.

Cerenkov light from the passage of relativistic charged particles through the lead glass is detected by 3 inch diameter phototubes at the base of each block.

2.2.4 Hadronic calorimeter

The hadron calorimeter(HCAL) [25] is built in three sections - the barrel, the endcaps and the pole-tips, and measures the energy of hadrons emerging from the ECAL. The detectors are positioned between layers of the magnet return yoke giving coverage of 97% of 4π and offering at least 4 interaction lengths of iron absorber to particles emerging from the electromagnetic calorimeter. Most hadrons are absorbed at this stage leaving only muons to pass on into the surrounding muon chambers.

The barrel consists of 9 layers of limited streamer tube chambers, alternating with 8 iron slabs and spans radii from 3.39m to 4.39m. The iron slabs are 100mm thick with 25mm gaps and provide 4 or more interaction lengths of absorber. The barrel ends are then closed off by 'D' shaped endcap regions (HE) which consist of 8 layers of chambers sandwiched between 7 slabs of iron.

Finally the pole-tip (HP) extends the coverage of hadron calorimetry down to $|cos\theta| = 0.99$. The number of samples in this region is increased to 10 in an effort to improve the OPAL energy resolution in the forward direction. The detectors themselves are 0.7cm thick multiwire proportional chambers, strung with anode wires at a spacing of 0.2 cm.

2.2.5 Muon Detector

The Muon detector is also split into a barrel detector (MB) and an endcap detector (ME). The aim of the muon detector is to be able to identify muons from potential hadronic background. This background is however very low due to particles incident on the muon detector having traversed the equivalent of 1.3m of iron, reducing the probability of a pion not interacting to less than 0.001.

Muon Barrel

The barrel region (MB) [26] consists of 110 drift chambers that cover the acceptance $|cos\theta| < 0.68$ for four layers and $|cos\theta| < 0.72$ for one or more layers. The chambers are each 1.2m wide and 90mm deep and their lengths are either 10.4m, 8.4m or 6.0m in order to fit between the magnet support legs.

Each chamber is split into two adjoining cells each containing an anode signal wire running the full length of the cell, parallel to the beamline. The coordinate in the ϕ direction can be determined from the drift time to the anode wire to an accuracy of better than 1.5mm. The inner surfaces of the cells have a system of diamond shaped cathode pads allowing a z measurement to an accuracy of 2mm.

Muon endcap

The muon endcap detectors [27] extend the coverage of the muon detector up to $|cos\theta| = 0.985$. Each endcap consists of four "quadrant" chambers which are approximately 6m square and 2 "patch" chambers that are 3m by 2.5m. This arrangement of quadrants and patches is necessary to give maximum coverage around the beam pipe, cabling for inner detectors and structure supports. The quadrants and patches consist of an arrangement of two layers of limited streamer tubes in the plane perpendicular to the beam line. Each streamer tube is 1cm by 1cm in cross section and the gas mixture in the streamer tubes is 25% Argon and 75% Isobutane (which is used to quench the charge avalanche caused by the ionisation). The pairs of planes are separated in z by 67cm and so provide two measurements of x and y across a significant lever arm. Each of the two layers of streamer tubes has two layers of readout strips, these strips are aligned both parallel and perpendicular to each tube. The spatial resolution achieved by the parallel wires is 3mm and 1mm by the perpendicular wires. Therefore x and y coordinates of a track can be measured once accurately and once relatively coarsely.

2.2.6 Forward Detector and SiW Luminometer

The forward detector (FD) [28] consists of an array of devices whose primary objective is to detect low angle Bhabha scattering events as a way of determining the LEP luminosity for the normalisation of measured reaction rates from decays. The detectors consist of an electromagnetic calorimeter, some drift chambers and a scintillator and are positioned at 2.6m from the interaction point. These detectors cover an angle between 47 and 120 mrad from the interaction point, with the only obstructions being the beam pipe and 2 mm of aluminium from the central detector pressure vessel.

In 1993 a silicon tungsten detector (SW) sampling calorimeter was installed to improve the accuracy of the luminosity measurement. There are two calorimeters, each 2.4m from the interaction point with an angular acceptance of 25 mrad to 59 mrad. Each calorimeter consists of 19 layers of segmented silicon detectors interleaved with 18 layers of tungsten sheets and have measured the luminosity to a level of 0.07% [29].

2.2.7 Trigger

LEP bunch crossings occur every 22 μs ie. at a rate of 45 kHz. This is far too fast to reconstruct every event as the reconstruction takes around 22 ms. To bring this rate down to an acceptable 1 to 5 kHz without losing physics a trigger system is used [30]. This trigger system uses information from the subdetectors to select crossings with possible e^+e^- interactions. This lower rate can then be handled by the data acquisition system. The trigger has to decide with a high efficiency which events are e^+e^- interactions and at the same time reject backgrounds such as cosmic rays, detector noise or interactions with the beam pipe. The trigger information from the subdetectors is divided into two categories. Firstly there are 'stand-alone' signals from the subdetectors such as multiplicity counts or energy sums. These give a high degree of flexibility, allowing efficiencies to be calculated for each subdetector.

Secondly the solid angle covered by the OPAL detector is divided into a matrix of 6 overlapping θ bins and 24 overlapping ϕ bins. Subdetectors[b] provide inputs to this matrix and the OPAL central trigger logic decides if the event should be processed further.

The various parts of the trigger can be split into 5 parts and these are discussed briefly below :

Track Trigger Information from CV and CJ is processed with the aim of finding tracks. For each hit in either subdetector a quantity z/r is determined and fed into the $\theta - \phi$ matrix discussed above. Charged tracks can be thought of as straight in the r-z projection. If originating from the vertex, the hits along the track will have the same z/r value. If not, then z/r will have a radial dependence. For speed only 4 annular groups of 12 adjacent wires are used. One annulus is totally within CV and the other 3 are in CJ at various radii. The efficiency of this trigger is estimated to be >98%.

Time-of-Flight Trigger The primary purpose of this trigger is to reject cosmic rays. A coincidence on each end of a scintillator counter is demanded within 50 ns of a LEP bunch crossing. A trigger is generated if more than a quarter

[b] CV, CJ, TB, EB, EE, MB, ME, FD and SW.

of the scintillator counters satisfy the coincidence condition. The efficiency of this trigger is measured to be >90%.

Electromagnetic Trigger The barrel and endcap electromagnetic calorimeters are divided into groups of 48 lead-glass blocks to form a binned $\theta - \phi$ array. Energy in these bins is discriminated at 4 GeV to produce stand-alone triggers. Discrimination at 1 GeV allows the signals to be combined with other trigger signals and entered into the main $\theta - \phi$ matrix.

Muon Trigger The barrel and endcap are treated separately. In the barrel, 3 out of 4 layers must fire over a ϕ bin of around 15°. This trigger is never used stand-alone as it suffers from the cosmic ray background. A trigger signal is generated in the endcaps if charge deposited in half the layers is above a lower threshold and the muon track segment can be associated with a central detector track. The x-y co-ordinates of the track are transposed into $\theta - \phi$ and entered into the main trigger matrix. The endcap trigger is only used with a left-right coincidence in the stand-alone mode to reduce the cosmic ray background rate. The overall efficiency of the muon trigger is measured as >95%.

Luminometer Trigger The FD trigger signal is made up from energy sums in the presampler, calorimeter and fine luminosity scintillators. Left-right coincidences of these signals are used to produce stand-alone triggers. The trigger signals are also combined with other detectors for $\gamma\gamma$ event detection. The efficiency of this trigger is measured to be $> 98.5\%$. The silicon tungsten calorimeter provides a trigger by requiring the energy from either end to exceed a low threshold. This is checked against an independent FD trigger formed from energy sums at both ends of the detector and is measured to be ~100% efficient.

For the tau analysis described in this thesis the most important triggers are:-

- A coincidence between the track trigger and the EM trigger.

- A coincidence between the track trigger and the Muon trigger.

- A coincidence between the EM trigger and TOF trigger.

- A coincidence between the track trigger in one endcap and EM trigger in other endcap.

- The track trigger flagging the tracks as collinear.

- The EM energy cluster being above the threshold.

When LEP started colliding 8 bunches of electrons and 8 bunches of positrons the crossing rate increased to 90Hz. To cope with this increase a pre-triggering system was introduced [31]. The pre-trigger system is similar to the trigger system, subdetector pretrigger signals divide into 'stand-alone' signals from energy sums, and lower threshold signals from 12 bins in θ/ϕ . The reduction in number of bins from the main trigger system allows the whole process to function much more rapidly. The pretrigger processor makes its decision by multiplicity counting and possibly forming correlations in θ/ϕ between subdetectors, together with the stand-alone signals. This pretriggering system was retained when LEP reverted to 4 by 4 bunch crossings.

If the event does not pass the trigger analysis then the subdetectors are sent a signal to reset in readiness for the next bunch crossing.

2.2.8 Data Acquisition

This is broken down into several levels.

Front end processing

When a beam crossing is selected by the trigger as containing a potentially interesting event, the subdetectors are read out. Each one of the sixteen subdetectors is read out separately by its own special front-end readout electronics into its local system crate(s) ('LSC'). The LSCs acquire data, format and prepare it for the software filter. For most of the subdetectors two LSCs are used with one of them acting as the master LSC.

Event builder and filter

The event builder [32] consists of two crates. The event builder crate synchronises all the LSC readouts and the sub events are formatted into a complete event. The system can handle 10Hz of on average 100kb events. The filter [33] then performs a fast analysis of each event. The events are classified into various physics categories and background can be rejected or downscaled. To classify the events several sources of information are used: calibrated calorimeter signals, time of flight information, muon chamber information and jet chamber tracks.

ROPE

The final part of the process is the OPAL reconstruction package known as ROPE [34], Reconstruction of OPAL Events. The input to ROPE is raw data produced by either the detector or the OPAL simulation package GOPAL. The ROPE code outputs summaries of calculated quantities such as energy clusters, momenta and so on. This is then stored on Data Summary Tapes (DST) or on Optical Disks.

2.2.9 Simulation of the OPAL detector

The OPAL Monte Carlo simulation program is known as GOPAL [35] which stands for GEANT at OPAL (GEANT [36] is a general material simulation package) . This provides a model of the detector including all the material, geometries and densities. Particles are generated from Monte Carlo event generators such as KORALZ [37], JETSET [38] and TAUOLA [39]. These event generators simulate the decay of a Z^0 and are designed to work efficiently for different Z^0 decay channels. ie. JETSET is used to study of multihadronic decays, KORALZ for the study of leptonic decays.

Then they are run through GOPAL and the output is an accurate simulation of the data. All hits, energy clusters and so on are recorded just as if the particles were real data. Noise, inefficiency and resolution effects are also included to give a more accurate model.

The output of the program is the same as the OPAL raw data and are also stored on DST's, however there is an extra block containing all the Monte Carlo information. The output is finally passed through ROPE to produce the data summaries in the same way as the data. The GOPAL output is checked against real data taken in physics runs and any modeling errors found can be corrected.

Chapter 3

Tau Physics

3.1 Introduction

The tau particle is important for many reasons. It is the third generation charged lepton, and also the heaviest of the leptons. This large mass of the tau opens up a new range of physics as it is the only lepton which can decay into hadrons. The existence of its partner in the third generation, the tau neutrino, has still only been established indirectly from tau decay data. This is in contrast to the other two neutrinos which have been detected from direct interactions with nuclei. The upper limit on the tau neutrino mass also allows it to be considered in astrophysics for the role of dark matter.

As a check of the Standard Model two questions need to be asked: "Are the tau and its neutrino truly elementary?" and "Is the tau a sequential lepton with the same vertices and couplings as the electron and muon?"

The experimental approach to answering these questions is to:

- Measure the static properties of the tau and its neutrino, particularly their masses.
- Study their production and decay by the electroweak current.
- Search for interactions of tau neutrinos and possible interactions between these and other neutrino species.

- Investigate the hadronic decay modes of the tau which provide a method of studying low energy effects of the strong interaction in a "clean" environment.

Due to the increasing data sample (particularly from LEP experiments) the tau is now producing some of the most accurate tests of the Standard Model. These tests cover a wide range of effects from measurements of the electroweak charged and neutral current to QCD tests to direct searches for physics beyond the Standard Model.

3.2 The History of the τ

The τ lepton was discovered in 1975 [40] by the MARK1 collaboration, for which Martin Perl received the Nobel Prize in 1995. This discovery was in part due to the newly developed electron-positron storage rings at SLAC and used the SPEAR e^+e^- collider.

The discovery of the tau stemmed from speculation that the electron and muon were just the two lightest members of the lepton family and that further heavy members also existed. It was assumed that these new leptons would obey their own lepton conservation and that the mass of the charged lepton would be much larger than that of the neutrino. These assumptions simply followed the observations recorded about the electron and muon.

The first evidence for the tau was published by Perl *et al.* [41] as 'Evidence for Anomalous Lepton Production in e^+e^- Annihilation' and presented decays of the following type :

$$e^+e^- \rightarrow e + \mu + \text{missing energy} \tag{3.1}$$

The paper concluded that a possible explanation for these events was the production and decay of a new pair of particles having a mass between 1.6 GeV and 2.0 GeV.

It took three years to verify the discovery of the tau, measure its major properties and confirm that it was a lepton. Most of the work being done at the SPEAR storage ring at SLAC [42] and also the DORIS ring at DESY [43]. The first important discovery in this period was the so called 'Anomalous μ events' ;

$$\mathrm{e}^{+}\mathrm{e}^{-} \rightarrow \mu^{+} + \mathrm{hadrons} + \mathrm{missing\,energy} \tag{3.2}$$

where the μ comes from the decay of one τ and the hadrons from the decay of the other τ [44]. The confirmation of the leptonic nature of the tau was not arrived at until the indirect discovery of the ν_τ. All the deduced properties of the ν_τ are consistent with it being a conventional neutrino although no direct observation has been made yet.

3.3 The Tau Mass

The masses of particles are not predicted by the Standard Model and so must be obtained by experiment. Although not predicted by the model, the mass of the tau is an important parameter used in, for example, the leptonic branching ratio calculation where it enters as a term to the fifth power. The mass is also very important with respect to discriminating between lepton generations as this is expected to be the only difference.

The most precise measurement of the tau mass has been obtained using the Beijing Spectrometer (BES) at the Beijing Electron-Positron Collider (BEPC) [45]. The method used was to measure the $\mathrm{e}^{+}\mathrm{e}^{-} \rightarrow \tau^{+}\tau^{-}$ cross section within a few MeV of the tau threshold, as this is the region where the cross section is most sensitive to m_τ. If the tau is assumed to be a spin half particle then the cross section is given by the following equation:

$$\sigma(\mathrm{e}^{+}\mathrm{e}^{-} \rightarrow \tau^{+}\tau^{-}) = \frac{4\pi\alpha^2}{3\mathrm{s}}\beta\frac{3-\beta^2}{2} \tag{3.3}$$

where s is the centre of mass energy squared, α is the QED fine structure constant and $\beta = \sqrt{1 - 4m_\tau^2/s}$. Therefore this experiment not only measures the mass but it is also a sensitive test of the spin of the tau.

The initial sample used at BES consisted of τ pairs where one τ decayed into an e and the other decayed into a μ. This provided a very pure sample of tau events but the statistics were very low. Recent re-analysis uses a sample consisting of not only di-lepton decays but also lepton-hadron decays, which provides greater statistics. The method is then to fit the measured cross-sections with a likelihood fit and obtain a value of m_τ. The value of the mass obtained from the BES is :

$$M_\tau = 1776.96^{+0.18+0.20}_{-0.19-0.16}\,\mathrm{MeV} \tag{3.4}$$

and the cross section at the tau threshold can be seen in figure 3.1.

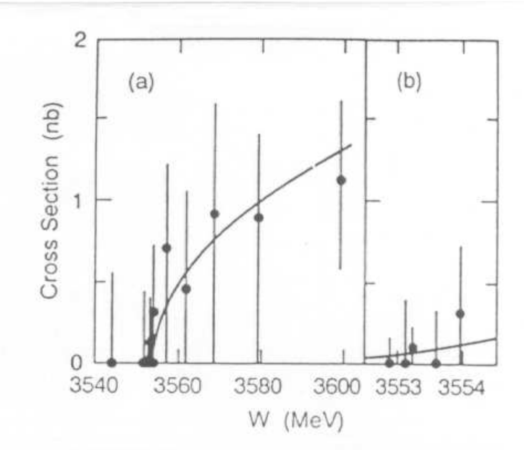

Figure 3.1: The cross section for $e^+e^- \rightarrow \tau^+\tau^-$ near the threshold measured by BES. The curve is the theoretical prediction using the value of m_τ from a maximum likelihood fit. (b) is a closeup of (a) near threshold.

Another method of obtaining the mass is used by ARGUS [46] and CLEO [47]. This method uses events where one tau decays to three pions and the other decay goes to one charged particle. By kinematics the mass of the tau can be reconstructed if the properties of the decay products are known. Unfortunately the neutrino will escape detection and therefore direct calculation from the tau decay products is impossible requiring a pseudomass to be defined using the pions as follows :

$$(m_\tau^*)^2 = 2(E_\tau - E_{3\pi})(E_{3\pi} - p_{3\pi}) + m_{3\pi}^2 \tag{3.5}$$

This pseudomass will tend to the mass of the tau as the mass of the neutrino tends towards zero. The measured spectrum of this pseudomass is plotted and reveals a sharp drop corresponding to the mass of the tau as shown in figure 3.2. Using the previous kinematic method the following measurements of the mass have been obtained:

$$m_\tau = 1776.3 \pm 2.4 \pm 1.4\text{MeV} \quad \text{(ARGUS)} \tag{3.6}$$

$$m_\tau = 1777.8 \pm 0.7 \pm 1.7\text{MeV} \quad \text{(CLEO)} \tag{3.7}$$

which agree well with the measurement made by the BES.

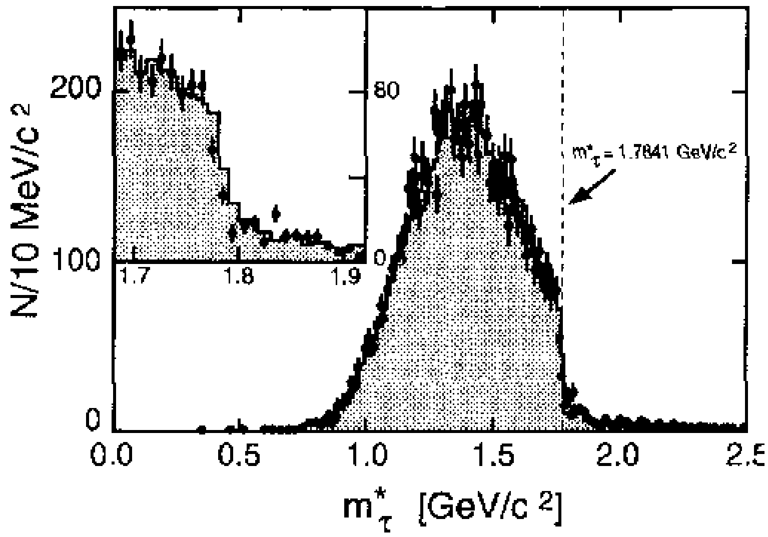

Figure 3.2: The pseudomass distribution from $\tau^- \rightarrow \pi^-\pi^-\pi^+\nu_\tau$ collected by the ARGUS collaboration, showing data (points with error bars) and Monte Carlo (shaded histogram)

3.4 Production of τ's from e^+e^- Collisions

Although taus have been observed in hadron collisions the greatest contribution to the knowledge of the tau comes from e^+e^- collisions. These experiments provide an insight into the electroweak neutral current interactions of the tau. There are four main regions that can be explored from these interactions:

The threshold region explored at SPEAR and BEPC.

The heavy quark resonance region investigated by CESR and DORIS.

The electroweak interference region, PETRA, PEP and TRISTAN.

And finally the Z region which SLC and LEP have explored in great detail.

As the cross-section to leptons is enhanced by the Z^0 pole the rates are high and the relative contribution to QED is small, making the Z^0 region the most favourable for the study of the tau. The Feynman diagram for this process is shown in figure 3.3. The production cross section, angular distribution and polarisation of the tau are used to study its neutral current couplings and following is an explanation of these terms.

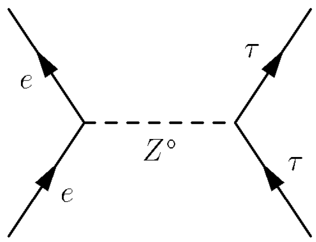

Vertex factors are $ig\gamma_\mu(C_V^f - C_A^f\gamma_5)\frac{1}{2cos\theta_W}$

Figure 3.3: A Feynman diagram illustrating the production of tau leptons from e^+e^- collision

Above the threshold the cross section for $e^+e^- \to \tau^+\tau^-$, at Born level, can be decomposed into three terms,

$$\sigma^0(s) = \sigma^0_\gamma + \sigma^0_Z + \sigma^0_{\gamma Z} \tag{3.8}$$

Where the first term is the purely electromagnetic contribution, the second term is the contribution due to Z^0 exchange and the third term is the interference term. The interference term gives a small contribution to the total sum at all energies. If the discussion is now specialised to charged leptons then the following relation can be written for the scattering angle θ, defined as the angle between the incoming e^- and the outgoing τ^-.

$$\frac{d\sigma}{d\Omega} = \frac{\alpha^2}{4s}[a_0(1 + cos^2\theta) + a_1 cos\theta] \tag{3.9}$$

Where a_0 is a symmetric term and a_1 is an antisymmetric term:

$$a_0 = 1 + C_V^e C_V^\tau 2Re(\chi) + ((C_V^e)^2 + (C_A^e)^2)((C_V^\tau)^2 + (C_A^\tau)^2)|\chi|^2 \tag{3.10}$$

$$a_1 = C_A^e C_A^\tau 4Re(\chi) + C_V^e C_V^\tau C_A^e C_A^\tau 8|\chi|^2 \tag{3.11}$$

both of which are dependent on the electroweak coupling parameters C_A^l and C_V^l and also on a pole term χ.[a]

$$\chi = \frac{G_F}{\sqrt{8}\pi\alpha}\frac{sM_Z^2}{(s - M_Z^2) + iM_Z\Gamma_Z} \tag{3.12}$$

At the pole this χ term is purely imaginary. These a terms lead to a sizeable forward backward asymmetry which is a measure of the relative strengths of the symmetric and asymmetric terms in the cross section. This forward backward asymmetry can be written as :

$$A_{FB} = \frac{3a_1}{8a_0} \tag{3.13}$$

And on the Z pole this becomes :

$$A_{FB}(s = M_Z^2) = \frac{3}{4}A_e A_\tau \tag{3.14}$$

Where the neutral current coupling parameters for each lepton species, l ($= e$, μ or τ), are given by :

$$A_l = \frac{2C_V^l C_A^l}{(C_V^l)^2 + (C_A^l)^2} \tag{3.15}$$

[a] Originating from the Breit Wigner peak

3.4.1 Polarisation

Due to parity being violated in both Z^0 production and Z^0 decay the result is that the τs produced will be polarised even if the initial state electrons or positrons are not polarised. (Parity is violated due to the standard electroweak theory requiring different left and right hand couplings to the Z^0, as discussed in section 1.2.6). The degree of polarisation the τ receives is dependent on the relative strengths of the axial and vector couplings and also on the scattering angle. Therefore at each scattering angle θ one can define a helicity asymmetry $A_\tau(\theta)$ which can be written at Born level as :

$$A_\tau(\theta) = \frac{A_\tau(1 + cos^2\theta) + 2A_e cos\theta}{(1 + cos^2\theta) + 2A_e A_\tau cos\theta} \tag{3.16}$$

To obtain the average final state polarisation, P_τ, one must integrate the previous equation over the scattering angle, whereupon one obtains :

$$\int_{-1}^{+1} A_\tau(\theta) dcos\theta \equiv -P_\tau = A_\tau \tag{3.17}$$

Therefore it can be seen that using equation 3.15 and the fact that $(C_V^l)^2 \ll (C_A^l)^2$, that a measurement of this polarisation can be used to determine the ratio of the axial and vector couplings of the tau lepton. To measure the corresponding coupling ratios for the electron a further quantity known as the forward-backward polarisation asymmetry is used. This expression is formed by integrating the polarisation separately over the forward and backward hemispheres and results in the following equation:

$$A_{pol}^{FB} = -\frac{3}{4} A_e \tag{3.18}$$

which can be obtained experimentally measuring the polarisations in the forward and backward hemispheres and combining with the number events observed in each of these hemispheres.

3.5 Decays of the τ by Weak Charged Current Interaction

The Standard Model imposes lepton universality of charged and neutral current couplings, meaning that the charged weak current decay of the tau should be identical to that of the muon, (except for mass effects). Therefore it is important for the study of the tau that its leptonic currents are well understood. The leptonic decay of the tau is show in figure 3.4 along with the semi-hadronic decay (discussed in detail in [49]).

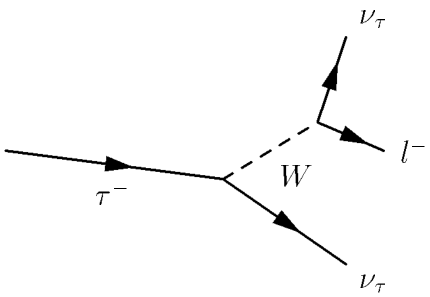

Vertex factors are $\frac{ig}{\sqrt{2}}\gamma_\mu\frac{(1-\gamma^5)}{2}$

Propagator term is $\frac{1}{(M_W^2-q^2)}$

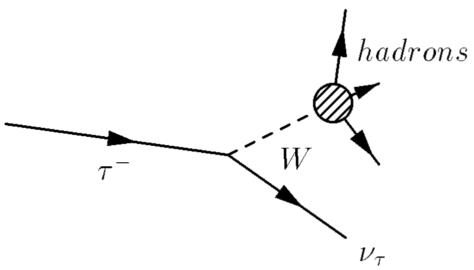

Lepton/W vertex factor is $\frac{ig}{\sqrt{2}}\gamma_\mu\frac{(1-\gamma^5)}{2}$

Figure 3.4: The leptonic and semi-hadronic decays of the tau.

The total coupling strength of the electron, muon and tau is the obvious first place to start comparisons. The total coupling strength measured by the Fermi constant G_F is defined by the following equation [48]:

$$\Gamma(\tau^- \to e^-\bar{\nu}_e\nu_\tau) = \frac{G_F^2 m_\tau^5}{192\pi^3} F_e(x) F_W F_{rad} \quad (3.19)$$

where $F_e(x)$ is the correction due to the finite mass of the final lepton state and is given by,

$$F_l(x) = 1 - 8x + 8x^3 - x^4 - 12x^2 ln(x) \quad (3.20)$$

where

$$x = \frac{M_l^2}{M_\tau^2} \quad (3.21)$$

and l represents the heaviest final state lepton.

The correction due to the finite mass of the W propagator is given by

$$F_W = 1 + \frac{3M_\tau^2}{5M_W^2} \quad (3.22)$$

Finally one must consider the adjustment necessary when the effect of the emission of real photons and fermion pairs, as well as virtual photons, are considered. This correction due to QED radiative effects is given by:

$$F_{rad} = 1 + \frac{\alpha(M_\tau)}{2\pi}\left(\frac{25}{4} - \pi^2\right) \quad (3.23)$$

with $\alpha(M_\tau)$ being the fine structure constant calculated at the tau mass.

Now the partial width can be related to the branching ratio as it is equal to the total width multiplied by the branching ratio. We also know that the total width is equal to the reciprocal of the lifetime and so can write:

$$\Gamma(\tau^- \to e^-\bar{\nu}_e\nu_\tau) = \Gamma_\tau BR(\tau^- \to e^-\bar{\nu}_e\nu_\tau) = \frac{BR(\tau^- \to e^-\bar{\nu}_e\nu_\tau)}{\tau_\tau} \quad (3.24)$$

where τ_τ is the tau lifetime.

3.5.1 τ Lifetime

The measurement of the tau lifetime has been much improved since it was first measured by MARKII in 1983 [50], this is mainly thanks to LEP and the advent of high precision vertex detectors. The vertex detectors help reconstruct secondary vertices as the tau itself decays within the beam pipe. Two main methods are used to make the measurement, the first using a mean impact parameter and the second measuring the decay length directly.

The impact parameter method [51] uses a sample of one prong tau decays and calculates the lifetime from comparison to Monte Carlo using the following equation:

$$\tau_\tau = \tau_{MC} \frac{x_{meas}}{x_{MC}} \tag{3.25}$$

where τ_{MC} is the Monte Carlo tau lifetime, x_{meas} and x_{MC} are the mean trimmed impact parameters of the data and Monte Carlo respectively. (10% trimmed means are used *i.e.*the lowest and highest 5% of the entries were removed.) The OPAL value for this method is :

$$\tau_{ip} = (290.4 \pm 3.5 \pm 2.2) fs$$

The method which measures the decay length directly [52] uses a sample of three prong tau decays, and although this method is powerful, it is this three prong selection which limits the statistics available. It does however provide a statistically independent sample from the other method making comparison of the two results a useful cross check. From the measurement of the decay length the Lorentz boosted lifetime can be directly calculated.

$$\tau_{dl} = (289.0 \pm 3.6 \pm 1.8 fs)$$

As the two methods are independent statistically the two results can be combined to give a total OPAL average of

$\tau_{ave} = (289.2 \pm 1.7 \pm 1.2) fs$ [53]

which can be compared to the current world average of

$\tau_{ave} = (291.0 \pm 1.5) fs$ [54]

3.5.2 Universality Test

Using the measurements described in the previous sections a direct test of lepton universality can be made. First the Fermi constant G_F must be factorised into effective couplings for each lepton G_l where :

$$G_F^2 \to G_\tau G_l \quad (l = e, \mu) \tag{3.26}$$

$$G_l = \frac{g_l^2}{\sqrt{32 M_W^2}} \quad (l = e, \mu, \tau) \tag{3.27}$$

Therefore it can be seen from equations 3.19 and 3.24 that these values can be used to express the branching ratios of the tau to the electron and muon as follows:

$$\frac{BR(\tau^- \to \mu^- \bar{\nu}_\mu \nu_\tau)}{BR(\tau^- \to e^- \bar{\nu}_e \nu_\tau)} = \frac{F_\mu(x) g_\mu^2}{F_e(x) g_e^2} \tag{3.28}$$

which can be translated into ratios of the coupling constants and have the following current world average :

$$\left| \frac{g_\mu}{g_e} \right| = 1.001 \pm 0.004 \tag{3.29}$$

which shows excellent agreement with the $e - \mu$ universality hypothesis. The coupling constants for the tau can also be extracted from the leptonic branching ratios and give the following result :

$$\left| \frac{g_\tau}{g_\mu} \right| = 0.999 \pm 0.003 \tag{3.30}$$

showing excellent agreement with the $\mu - \tau$ universality hypothesis.

3.6 Mass Limit calculation for M_{ν_τ}

If one assumes lepton universality then a limit on the mass of the tau neutrino can be calculated as follows. It can be clearly seen that rearranging equation 3.28 gives $F_e(x)$ in terms of the leptonic branching ratios and $\frac{g_\mu^2}{g_e^2}$. Both the branching ratios are known to a high accuracy, and lepton universality is assumed. Now one can assume that the tau neutrino is the heaviest final state lepton in the decay and hence (from 3.20 and 3.21) the function $F_e(x)$ contains the neutrino mass. As the tau mass is also known to a high accuracy one can solve this equation, which gives a value of

$m_{\nu_\tau} < 137MeV$ at a 95% confidence level [55].

This limit is not as accurate as direct searches for the neutrino but has the advantage of not being sensitive of statistical fluctuations and is completely independent of direct search results.

3.7 Topological Branching Ratios

Charge conservation implies that the tau must decay into products with a net charge of one. From the Standard Model the decays must be either to one charged lepton or to an odd number of charged mesons ($\pi^\pm$ and/or $K^\pm$). The relative inclusive[b] decay rates to one, three, five and seven charged particles ("prongs") are known as the topological branching ratios, B1, B3, B5 and B7. These values must sum to one. The topological branching ratios are relatively easy to measure at high e^+e^- centre of mass energies due to the ease of reducing multihadronic background. The decay products of the two taus are also kinematically well separated at high energies. However due to the low mass of the tau the decay products tend to lie in a narrow cone making it difficult to distinguish each decay product. Despite this the LEP experiments still have produced the most accurate measurements of the ratios. The higher multiplicity, five and seven prong branching ratios are more difficult to measure due to the multihadronic background. The seven prong decay

[b]Exclusive decays are defined as decays in which only certain specified particles are produced. In contrast inclusive decays are defined as decays where certain particles are looked for but other particles are allowed to be produced [56].

has not yet been observed but a limit on its branching ratio has been measured as $B7 < 1.7{*}10^{-5}$ [57]. It is not possible to predict the topological branching ratios from theory. However certain exclusive modes can be predicted [58] and their branching ratios can be summed to give a total one prong branching ratio. Unfortunately not all of the one prong decay modes have been predicted so to compare theory to a one prong measurement experimental results for the uncalculated modes must be used. Accurate calculation by theory of the three prong, five prong and seven prong branching ratios has not been achieved. The sum of these theoretical predictions and their comparison to experiment is discussed later in chapter 7.

The topological branching ratios are however most useful as a check of internal data consistency and as a search for new unexpected tau decays. To do this one must sum all the exclusive modes measured in each multiplicity. The sum of the one prong exclusive branching ratios should then match the measured one prong inclusive ratio. This is where the topological branching ratios have played an important role in tau physics, in trying to understand the experimental problem known as the "one prong deficit". This problem which is a decade old was that the sum of the exclusive tau decays was not consistent with the measured topological branching fractions. This problem was more evident in the one prong decays. However recent precise measurements seem to have reduced this inconsistency [59] which was mainly due to poorly measured one prong branching ratios involving kaons.

This thesis aims to measure the topological branching ratios as a test of the understanding of the tau decay.

Chapter 4

Selection of $\tau^+\tau^-$ Events

To study the interactions of the tau it is necessary to obtain a clean sample of tau pair events. This is done in three main stages. Firstly a low multiplicity requirement is made to reject the vast majority of multihadronic events, then cuts are made to suppress the non-lepton pair background, and finally, the leptons are classified as Bhabha, muon pairs or tau pairs. The following sections describe these selections in detail. It is useful in these discussions and the following chapters to define two regions of the detector, the barrel and the endcap. The barrel is defined as $|cos\theta| < 0.7$ as this is the largest angle with optimum central tracking chamber coverage, the CZ chambers end just above this angle, as does the maximum number of tracking hits available in CJ. From this the endcap region is defined as $|cos\theta| > 0.7$, although later in the analysis this definition will be changed to include an upper limit on this angle to decrease the background (see chapter 5). The selection procedure is found to be 75.18%$\pm$0.07 efficient over $|cos\theta| < 0.9$, details of which are found in [60]. This figure is of the same order as the published L3 topological branching ratios analysis [61], the recent DEPLHI analysis [62] and also the current ALEPH toplogical branching ratios analysis [63] but almost 30% higher than the selection efficiency in the published CELLO results [64].

4.1 Low Multiplicity Selection

The data obtained from LEP1 consists of e^+e^- pairs producing Z^0, which subsequently decay into $q\bar{q}$, $\nu\bar{\nu}$, e^+e^-, $\mu^+\mu^-$ or $\tau^+\tau^-$. The Standard Model predicts the following approximate branching ratios ; $Z^0 \to q\bar{q}(70\%)$, $Z^0 \to \nu\bar{\nu}(20\%)$, $Z^0 \to e^+e^-(3\%)$, $Z^0 \to \mu^+\mu^-(3\%)$ and $Z^0 \to \tau^+\tau^-(3\%)$. It is clear that the $\nu\bar{\nu}$ decays will not be seen in the OPAL detector leaving only $q\bar{q}$ or l^+l^- decays of the Z^0. The multihadronic decays typically produce 10 or more particles as can be seen in a typical event (figure 4.1), whereas leptonic decays usually have fewer than 10 tracks (figure 4.2). A simple selection to remove most of the multihadronic background events is to require that the sum of the number of charged particles ("tracks") in the central detector, plus the number of grouped energy deposits in the ECAL ("clusters"), is less than 17. The Low Multiplicity selection only considers events which are classified as good physics events by the OPAL filter. This selection is a standard OPAL procedure used for all leptonic analyses and will later be refined for the tau analyses.

4.2 Selection of Lepton Pairs

After this low multiplicity selection most of the surviving events are di-lepton events, however further fine tuning of this selection must be made to reduce the remaining non-lepton background. In particular there will still remain two photon processes, which are significant at these energies, and also cosmic ray events. The following sections describe the *preselection* [65] of the $\tau^+\tau^-$ sample used in the subsequent analysis.

4.2.1 Good Tracks and Clusters

To select lepton pairs in the preselection, each track in the central detector and each cluster in the ECAL is defined as "good" or "bad". Only those tracks or clusters flagged as good are kept and the rest are rejected.

The definition of a good track is as follows : firstly the track must have an energy

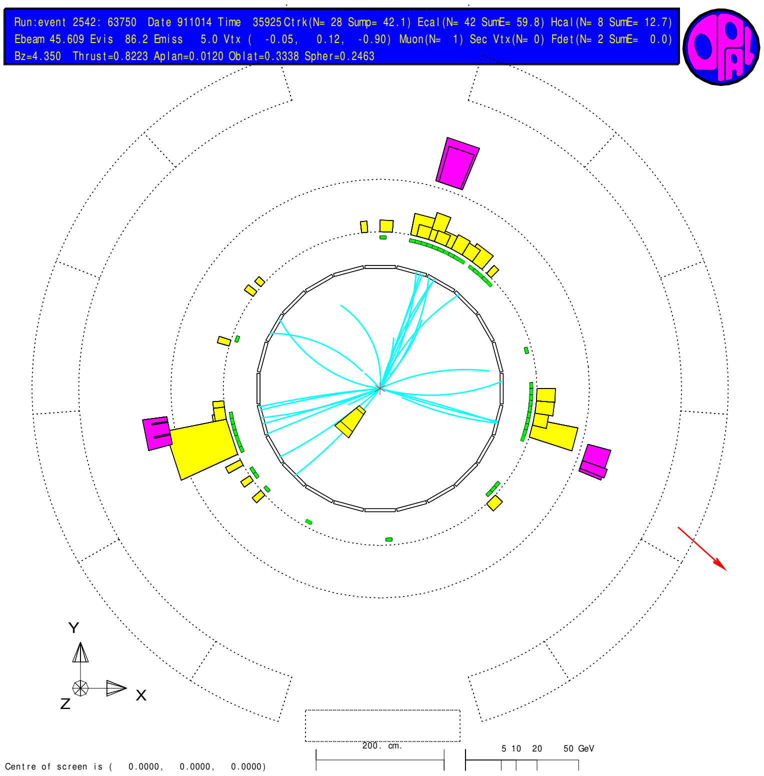

Figure 4.1: A typical 3 jet multihadronic decay. The central cluster of lines are tracks reconstructed in the central tracking chamber, the small boxes represent hits in the Presampler, the lightly shaded boxes represent hits in the ECAL, the darker shaded boxes represent hits in the HCAL and finally the arrow represents the reconstruction of a muon in the Muon detector.

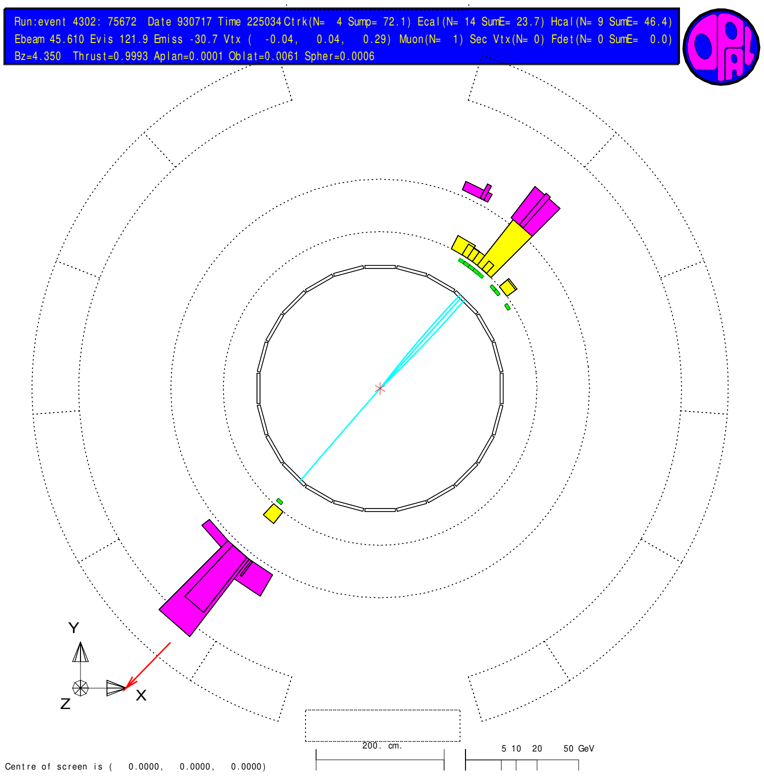

Figure 4.2: A typical tau decay.

greater or equal to 0.1 GeV and the number of hits in the CJ detector for that track must be greater or equal to 20. The first of these hits in CJ must be within a radius of 75cm of the origin. Finally $|d_0|$ must be less or equal to 2cm and $|z_0|$ must be less or equal to 75cm, where $|d_0|$ is the impact parameter and $|z_0|$ is the z coordinate at the point of closest approach to the origin.

The definition of a good cluster is slightly different in the barrel of the detector to the endcap of the detector. For the barrel region it is required that the raw energy of the ECAL cluster is greater or equal to 0.1GeV. In the endcap this is modified to 0.2 GeV and a further requirement is added that the number of ECAL blocks in the cluster is greater or equal to two.

4.2.2 Cone Definition

A candidate lepton pair event must have exactly two cones where a cone is defined by a jet finding algorithm. The jet finding treats each tau decay as a jet and associates charged tracks and clusters within a cone of half-angle 35°. The highest momentum track or highest energy cluster in the event defines the initial direction of the cone. The next highest momentum track or energy cluster within 35° of the initial direction is added and a new direction is calculated. This process continues until no more good tracks or good clusters can be added within 35° of the calculated direction. After the first cone the highest momentum track or highest energy cluster outside of the cone is taken and a new cone is formed. The algorithm stops when all good tracks and clusters in the event are associated to a cone. If a cone contains charged tracks it is known as a charged cone, however if it contains no charged tracks it is known as a neutral cone. For a cone to be classified as good the energy in the cone must be greater than or equal to 1% of the beam energy. Only good cones are used in this analysis.

4.2.3 Further Multiplicity Rejection

To reduce the remaining multihadronic background which has not been rejected by the loose Low Multiplicity cut it is required that the the total number of good charged tracks in the data is greater than 1 but less than 7 and that the total number of good ECAL clusters in the data is less than 11.

4.2.4 Cosmic Ray Event Rejection

To reject cosmic ray events requirements are made on the tracks in each event and also on the the TOF measurement of the track.

To ascertain whether the track points back to the interaction region the following parameters are used:

$|d_0|$ and $|z_0|$ as defined previously,

$|d_0|_{min}$ which is the minimum $|d_0|$ in the event,

$|z_0|_{min}$ which is the minimum $|z_0|$ in the event,

$|z_0|_{ave}$ which is the $|z_0|$ averaged over tracks with $|z_0|_{min} \leq 20$ cm.

It is then required that $|d_0|_{min} \leq 0.5$ cm, $|z_0|_{min} \leq 20$ cm and $|z_0|_{ave} \leq 20$ cm for an event to be retained and not classified as a cosmic ray event.

If the track originated from the interaction region, it must also satisfy the following TOF requirement. At least one TOF counter must satisfy;

$$|t_{meas} - t_{exp}| \quad \leq \quad 10 \text{ ns.}$$

where t_{meas} is the measured TOF and t_{exp} is the expected TOF assuming the event is created at the origin. An event is rejected if all TOF counter pairs with a separation larger than 165° in azimuthal angle, produce signals greater than 10ns apart in time.

4.2.5 Two Photon Event Rejection

Events when a photon from the incident electron interacts with one from the incident positron are called two photon events. The emitted photons may interact to produce, for example, a lepton pair, and so these must be rejected from our tau pair sample. A schematic diagram of such an event can be seen in figure 4.3. In most of these events the electron and positron deviate only slightly from their incident direction and continue down the beam pipe, this is due to the fact that the production rate of these two photon events increases as the angles θ_1 and θ_2 decrease, with these angles shown in figure 4.3. The photons from this type of event do not usually have equal momentum and so the events are often highly acollinear (*i.e.* the leptons produced are not back to back). This fact is exploited to eliminate these events as most of the lepton pairs from the Z^0 decay are collinear. Hence the following collinearity cut is used:

$$\theta_{acol} \leq 15^\circ$$

where θ_{acol} is defined as:

$$\theta_{acol} \equiv \cos^{-1}\left(-\frac{\mathbf{p_1}\cdot\mathbf{p_2}}{|\mathbf{p_1}||\mathbf{p_2}|}\right) < 15^\circ$$

and the labels are those referred to in figure 4.3.

Another variable, visible energy (E_{vis}), is also used to help eliminate these two photon events. Visible energy is defined as the maximum of either the scalar sum of the track momenta, summed over both cones, or the total cluster energy, summed over both cones. It is known that the visible energy for a two photon event will be low so the following rejection cut is applied:

$$E_{vis} \equiv \sum_{cone} Max(E_{cls}, p_{trk}) \geq 0.03\ E_{\rm CM}$$

where E_{cls} is the energy of the ECAL cluster associated to the track, p_{trk} is the momentum of the track, Max means the maximum of either E_{cls} or p_{trk}, and $E_{\rm CM}$ is the centre of mass energy of the event.

If the visible energy is above this threshold but still less than 20% of the centre of mass energy then further cuts are applied to the transverse momentum (P_t) of the charged tracks and clusters in the cones. If $E_{vis} \leq 0.20\ E_{\rm CM}$, then events are removed when either;

$P_t(cls) \leq 2$ GeV **.OR.** $P_t(trk) \leq 2$ GeV

where $P_t(cls)$ is the total transverse cluster energy in the event and $P_t(trk)$ is the total transverse track momentum of the event.

After these cuts the majority of two photon events are rejected from the sample.

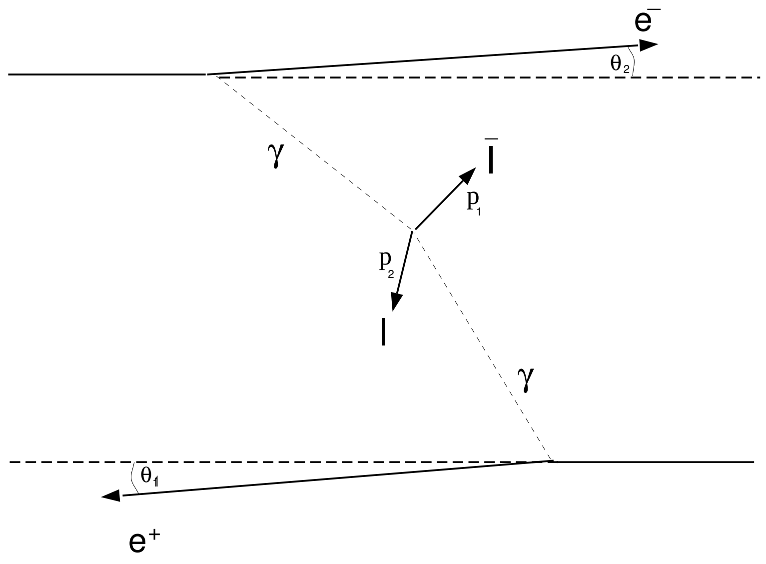

Figure 4.3: A schematic diagram of a two photon event. It should be noted that the interaction is *not* pointlike, this diagram is a schematic representation not a Feynman diagram.

4.3 Classification of each lepton pair

After all non-lepton background has been suppressed, the sample must be classified in terms of lepton pair type. Then electron pair ($e^+e^- \rightarrow e^+e^-$) and muon pair ($\mathrm{e}^+\mathrm{e}^- \rightarrow \mu^+\mu^-$) events can be rejected leaving only a sample of tau pair events. It is useful in these discussions to define the normalised track momentum summed over all tracks in the event, E^{trk}_{sum}, and also the normalised cluster energy summed over all the ECAL clusters in the event, E^{cls}_{sum}. Both variables are normalised to the center of mass energy and are defined so that

$$E^{trk}_{sum} \equiv \sum_i E_i^{TRACK}/E_{\mathrm{CM}}$$

$$E^{cls}_{sum} \equiv \sum_j E_j^{CLUST}/E_{\mathrm{CM}}$$

$e^+e^- \rightarrow e^+e^-$ rejection

Rejection of these events depends on the total ECAL cluster energy and the total track energy. This is due to the fact that the ECAL is very efficient at absorbing electrons and therefore $e^+e^- \to e^+e^-$ events will have high track and shower energies associated with them compared to muon or tau pair events. At high energies the shower energy measurement has a better resolution than the track energy measurement so a greater reliance is placed on this. Events are rejected if the sum of the cluster energies is greater than 0.8 of the centre of mass energy :

$$E^{cls}_{sum} > 0.8$$

or if the sum of the clusters plus 0.3 the sum of the track energies is greater than the centre of mass energy :

$$E^{cls}_{sum} + 0.3\ E^{trk}_{sum} > 1.0$$

In the endcap a slightly different cut is made due to the increase in the number of bhabha events in this region, events are rejected by the following requirements:

$$E^{trk}_{sum} > 0.8\ \textbf{.AND.}\ (E^{cls}_{sum} + E^{trk}_{sum}) > 1.05$$

.OR.

$$E^{trk}_{sum} \geq 0.8\ \textbf{.AND.}\ E^{cls}_{sum} > 0.25$$

e$^+$e$^-$ $\to \mu^+\mu^-$ rejection

From events surviving the above electron pair rejection, we select events with two associated cones identified as a muon. These events could be double $\tau \to \mu\nu\bar{\nu}$ decays from $e^+e^- \to \tau^+\tau^-$ events, or $e^+e^- \to \mu^+\mu^-$ events. Then, to separate between the $e^+e^- \to \mu^+\mu^-$ and $e^+e^- \to \tau^+\tau^-$ events, the total summed track and ECAL cluster energy is demanded to be high for the two muon candidates.

Most muons within the acceptance are characterised by a small energy deposition in the ECAL and associated signals in the HCAL and MUON subdetectors consistent with the passage of a minimum-ionising particle. Therefore to identify muons it is required that the candidate particles satisfy at least *one* of the following requirements;

- The particle be identified by the outer four MUON chamber layers;

$$N^{\rm MU}_{layers} \quad \geq \quad 2$$

  where $N^{\rm MU}_{layers}$ is the total number of layers with signals associated to the track in the barrel or endcap MUON detectors.

- The particle is identified by the HCAL ; $N^{\rm HC}_{layers} \geq 4$ **.AND.** $N^{\rm HC}_{last3} \geq 1$ **.AND.** $\mathrm{N}^{\rm HC}_{\rm hits/layer} < 2$
  where $N^{\rm HC}_{layers}$ is the number of HCAL layers containing signals associated with the track, $N^{\rm HC}_{last3}$ is the number of HCAL hits in the outer three layers of the HCAL and where $N^{\rm HC}_{\rm hits/layer}$ is the total number of HCAL signals assigned to the cone divided by $N^{\rm HC}_{layers}$.

- The particle is identified by the ECAL:

$$E^{clus}_{cone} \quad < \quad 2 \text{ GeV}.$$

To be classified as a muon pair both cones in the event must have a muon identified in each cone by at least one of the three requirements and also the total track and ECAL cluster energy must satisfy;

$E^{cls}_{sum} + E^{trk}_{sum} \geq 0.6$

which removes preferentially muon pairs from the tau pair sample.

Figures 4.4 and 4.5 show the distribution of events in terms of the normalised sum of track energies and cluster energies. Shown are the distributions for tau data, muon pair Monte Carlo, Bhabha Monte Carlo and tau pair Monte Carlo. It can be seen that, in the endcap, muons are still present in the data sample as shown clearly by the bottom right corner of figure 4.5 (d), which can be compared directly with the same plot in the barrel 4.4 (d). These muons are not identified due to their passing through areas of the endcap region not covered by the Muon endcap subdetector. This effect can be illustrated by examining events with E^{trk}_{sum} greater than 0.9. The distribution in ϕ for these events is plotted for tau data and muon pair Monte Carlo, and can been seen in figure 4.6. The figures show that there is an enhancement in the data corresponding to a decrease in the muon pair Monte Carlo. This implies that these tau events are in fact muon pairs which have not been identified. To remedy this situation a further requirement is made that all events selected as a tau pair must have the sum of E^{trk}_{sum} less than 0.9.

4.4 Estimation of Background contamination

4.4.1 Correction of Monte Carlo by Smearing

It was found [66] that the Monte Carlo models incorrectly the cluster energy and momentum resolution of tracks. To correct for this standard OPAL smearing routines were used. These are discussed in detail in [67]. In contrast to many previous analyses the smearing routine does not just apply a numerical correction to the ECAL cluster energies. Instead it uses a correction based upon the reciprocal of the normalised track momentum and also the ECAL cluster energy. These correction factors vary depending on the Monte Carlo sample used.

4.4.2 Estimation of the Contamination in the $e^+e^- \to \tau^+\tau^-$ Sample

After the previous selection the sample contains a relatively pure sample of tau pairs, however there are still background events which pass the selection and these backgrounds must be carefully measured and understood. The backgrounds in the tau sample have been investigated in the barrel region and are well understood [68]. Table 4.1 shows the multiplicative correction factors calculated from this previous work, which are then applied to the estimated Monte Carlo background in the barrel region; their comparison to the background in the endcap region is discussed at the end of this chapter. The backgrounds in the endcap region of the detector have

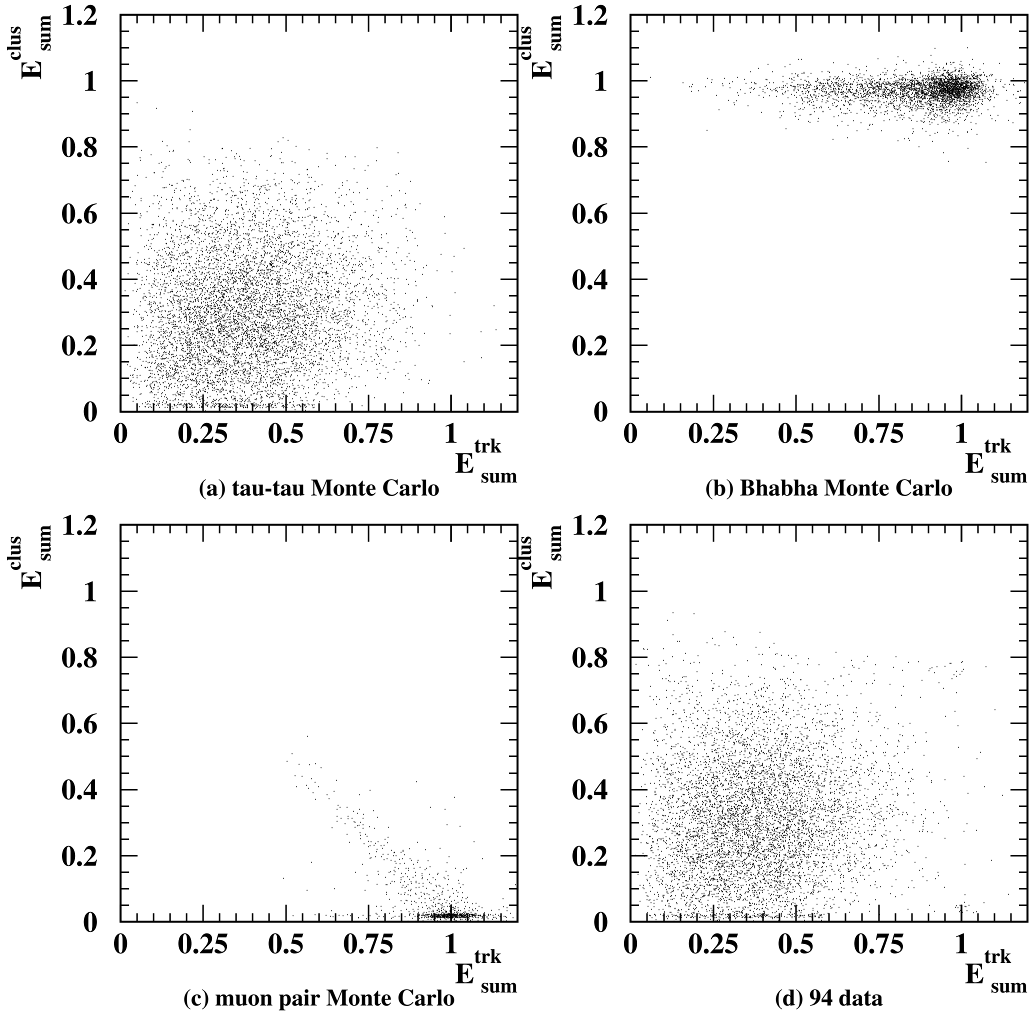

Figure 4.4: Scatter plots of E^{cls}_{sum} vs E^{trk}_{sum} for the barrel region, where the sum is over the event. The plots (a), (b) and (c) show Monte Carlo samples of tau pair, Bhabha and muon pair events, while (d) shows the data after tau pair selection.

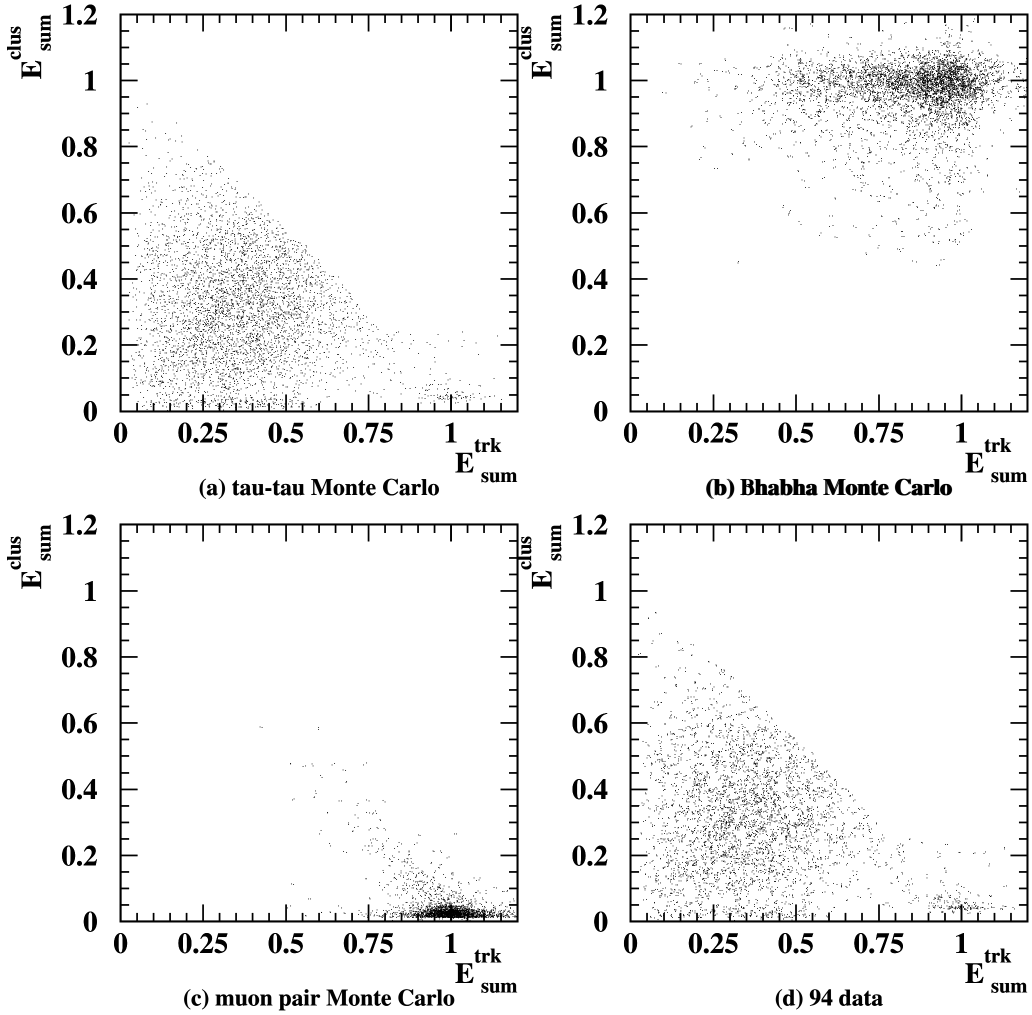

Figure 4.5: Scatter plots of E^{cls}_{sum} vs E^{trk}_{sum} for the endcap region, where the sum is over the event. The plots (a), (b) and (c) show Monte Carlo samples of tau pair, Bhabha and muon pair events, while (d) shows the data after tau pair selection. Unlike the barrel region it is necessary for an extra cut to eliminate the muon pairs which can be seen before the cut in (d). The diagonal cut-off seen in the data and tau pair Monte Carlo is due to the cut used in the endcap to eliminate bhabha events (see section 4.3).

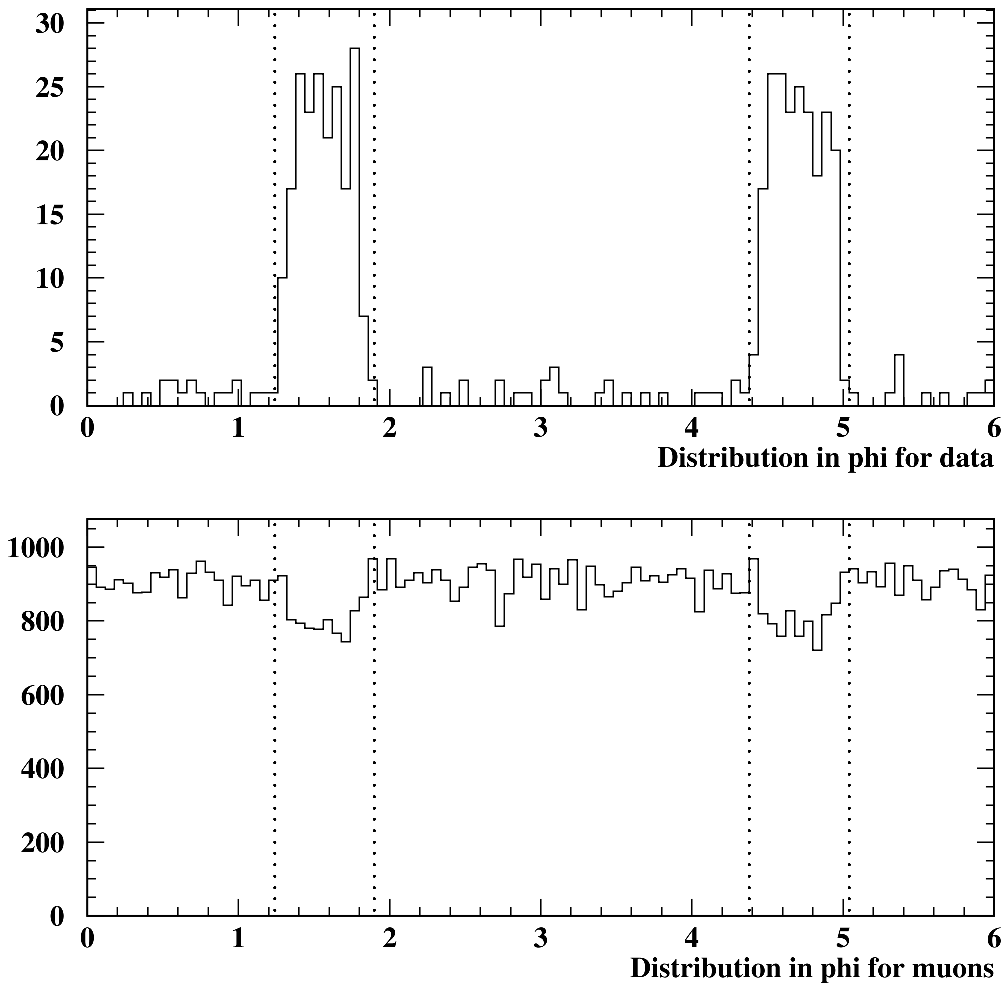

Figure 4.6: Distribution in phi of data and Monte Carlo muons in endcap with E^{trk}_{sum} greater than 0.9. The two peaks in the data distribution represent muons which pass through the gaps in ME. This is also shown in the decrease of events in the same regions on the plot for the Monte Carlo muons. The angles of the gaps in ME are bounded by the dotted lines on the plots.

not been fully investigated previously, requiring a detailed analysis which is now discussed.

Monte Carlo Sample	Correction			
	1992	1993	1994	1995
$e^+e^- \to e^+e^-$	3.15	2.16	1.70	2.05
$\mathrm{e^+e^-} \to \mu^+\mu^-$	1.57	1.33	1.44	1.06
$\mathrm{e^+e^-} \to \mathrm{q\bar{q}}$	1.00	1.00	1.00	0.69
$\mathrm{e^+e^-} \to \mathrm{e^+e^-e^+e^-}$	1.00	1.00	1.00	1.00
$\mathrm{e^+e^-} \to \mathrm{e^+e^-}\mu^+\mu^-$	1.00	0.84	0.89	1.00

Table 4.1: Correction factors for background in the barrel region.

The backgrounds are initially estimated from Monte Carlos but these estimates are corrected by data control samples to ensure that they model the data accurately. The control samples reflect the backgrounds estimated by the Monte Carlo and are obtained by selecting kinematic regions adjacent to the tau pair selection cuts so that the control data is representative of the actual backgrounds found in the data.

These selections for each data control sample represent specific channels of background for the tau pair data sample. However this control sample may itself have contamination from other sources and this is estimated from the other Monte Carlo samples and subtracted off the data control sample. For example, a sample of muon pairs is selected from the data. The predicted number of events which are not muon pairs are subtracted off before the number of muon pair events in data is compared with the Monte Carlo prediction. This produces a factor by which the Monte Carlo background must be multiplied to match the data. These numbers can be seen for the 1995 data in table 4.2.

The final details of the background are given in chapter 5 (section 5.4). The following sections describe the background correction for the 1995 data but the corresponding numbers for the other years can be found in appendix A.

Event sample	Number of events
MC $e^+e^- \to \mu^+\mu^-$	38 ± 2.0
MC $e^+e^- \to \tau^+\tau^-$	48 ± 1.6
All Data	107 ± 10.3
DATA $e^+e^- \to \mu^+\mu^-$	59 ± 10.5
Ratio $\frac{DATA(e^+e^-\to\mu^+\mu^-)}{MC(e^+e^-\to\mu^+\mu^-)}$	1.55 ± 0.29
MC $e^+e^- \to e^+e^-$	1333 ± 26.9
MC $e^+e^- \to \tau^+\tau^-$	140 ± 3.8
All Data	1740 ± 41.7
DATA $e^+e^- \to e^+e^-$	1600 ± 41.9
Ratio $\frac{DATA(e^+e^-\to e^+e^-)}{MC(e^+e^-\to e^+e^-)}$	1.20 ± 0.04
MC $e^+e^- \to q\bar{q}$	45 ± 4.2
MC $e^+e^- \to \tau^+\tau^-$	33 ± 1.8
All Data	80 ± 8.9
DATA $e^+e^- \to q\bar{q}$	47 ± 9.1
Ratio $\frac{DATA(e^+e^-\to q\bar{q})}{MC(e^+e^-\to q\bar{q})}$	1.04 ± 0.12
MC $e^+e^- \to e^+e^-\mu^+\mu^-$	536 ± 7.5
MC $e^+e^- \to \tau^+\tau^-$	0 ± 0
All Data	410 ± 20.2
DATA $e^+e^- \to e^+e^-\mu^+\mu^-$	410 ± 20.2
Ratio $\frac{DATA(e^+e^-\to e^+e^-\mu^+\mu^-)}{MC(e^+e^-\to e^+e^-\mu^+\mu^-)}$	0.76 ± 0.05
MC $e^+e^- \to e^+e^-e^+e^-$	395 ± 7.0
MC $e^+e^- \to \tau^+\tau^-$	0 ± 0
All Data	266 ± 16.3
DATA $e^+e^- \to e^+e^-e^+e^-$	266 ± 16.3
Ratio $\frac{DATA(e^+e^-\to e^+e^-e^+e^-)}{MC(e^+e^-\to e^+e^-e^+e^-)}$	0.67 ± 0.04

Table 4.2: Shown for the 1995 data are the control sample numbers for all background channels

$e^+e^- \to \mu^+\mu^-$

To select the muon pairs a muon has to be identified in both cones by either the ECAL, HCAL or muon chambers and the total energy (E^{trk}_{sum} + E^{cls}_{sum}) must lie between 0.6 and 0.75 (figure 4.7). This selection is similar to that used to antiselect muon pairs from the tau sample with the exception of the maximum total energy cut which is applied to ensure that the muon pair candidates selected are as similar as possible to the background muon pairs in the tau sample. The background predicted by the Monte Carlo is 0.87%. Comparing this with the data control sample gives a correction factor in the endcap of

$$\frac{\mathrm{DATA}(e^+e^- \to \mu^+\mu^-)}{\mathrm{MC}(e^+e^- \to \mu^+\mu^-)} = \frac{59 \pm 10.5}{38 \pm 2.0} = 1.55 \pm 0.29$$

$e^+e^- \to e^+e^-$

The bhabha selection for the background control sample uses a selection similar to that used to antiselect bhabhas in the tau sample. The main difference being that the normalised total cluster energy E^{clus}_{sum} must lie between 0.7 and 0.9, where in the anti-selection this figure is 0.8 (figure 4.7). Therefore the control sample represents data similar to that existing as background in the tau sample. The background predicted by the Monte Carlo is 0.64%. Comparing this with the data control sample gives a correction factor in the endcap of

$$\frac{\mathrm{DATA}(e^+e^- \to e^+e^-)}{\mathrm{MC}(e^+e^- \to e^+e^-)} = \frac{1600 \pm 41.9}{1333 \pm 26.9} = 1.20 \pm 0.04$$

$e^+e^- \to q\bar{q}$

To test the modelling of the multihadronic background, a sample was selected which enhanced the multihadrons compared to the taus. This was done by selecting higher multiplicity events which are rare in tau events. The specific multiplicities selected were any event where the total number of tracks is greater than 6. The background predicted by the Monte Carlo is 0.62%. Comparing this with the data control sample gives a correction factor in the endcap of

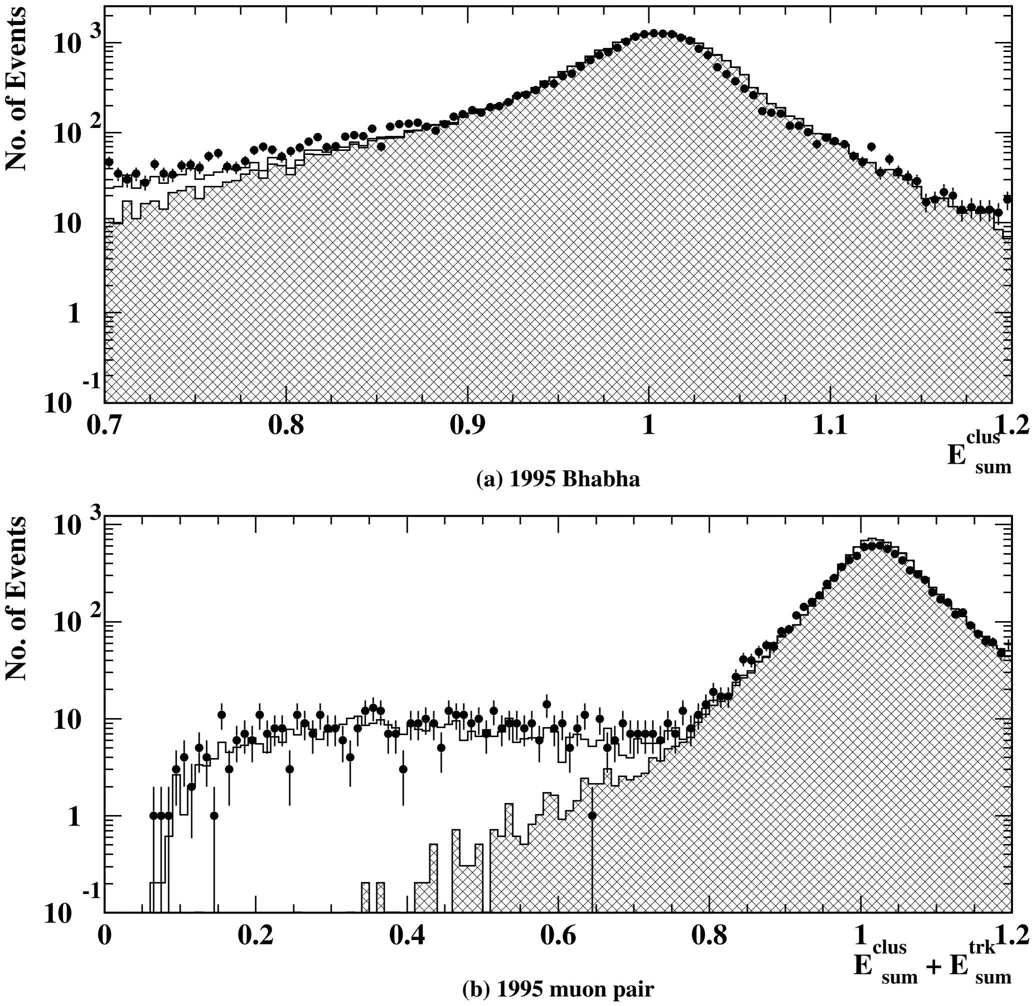

Figure 4.7: Distribution (a) is used to check the Bhabha background and shows the normalised sum of the clusters, E^{cls}_{sum} for the data (points), Bhabha Monte Carlo (hatched) and all other Monte Carlos not specifically under investigation (fullline). This later category is dominated by the tau pair Monte Carlo. The region 0.7 to 0.9 is investigated for the correction factor. Distribution (b) is used to check the muon pair background and shows the normalised sum of the tracks plus the clusters, $E^{cls}_{sum} + E^{trk}_{sum}$. The region between 0.6 and 0.75 is investigated for the corrections. The key is similar to the bhabha plot with the hatched are this time representing the muon pair Monte Carlo.

$$\frac{\mathrm{DATA}(e^+e^- \to q\bar{q})}{\mathrm{MC}(e^+e^- \to q\bar{q})} = \frac{47 \pm 9.1}{45 \pm 4.2} = 1.04 \pm 0.12$$

Two Photon Events

To select samples of two photon events ($e^+e^- \to e^+e^-\mu^+\mu^-$ and $e^+e^- \to e^+e^-e^+e^-$) leptons are rejected by the selection process used in the preselection and then it was required that the acollinearity of the two cones lies between 15° and 25° (figure 4.8). It was then required that $e^+e^- \to e^+e^-\mu^+\mu^-$ events had dE/dx≤8.5 keV/cm for each track in the cone and that a muon was identified in each cone. The $e^+e^- \to e^+e^-e^+e^-$ events were required to have dE/dx≥9.5 keV/cm for each track in the cone.

For $e^+e^- \to e^+e^-\mu^+\mu^-$ the background predicted by the Monte Carlo is 0.29%. Comparing this with the data control sample gives a correction factor in the endcap of

$$\frac{\mathrm{DATA}(e^+e^- \to e^+e^-\mu^+\mu^-)}{\mathrm{MC}(e^+e^- \to e^+e^-\mu^+\mu^-)} = \frac{410 \pm 20.2}{536 \pm 7.5} = 0.76 \pm 0.04$$

For $e^+e^- \to e^+e^-e^+e^-$ the background predicted by the Monte Carlo is 0.35%. Comparing this with the data control sample gives a correction factor in the endcap of

$$\frac{\mathrm{DATA}(e^+e^- \to e^+e^-\mu^+\mu^-)}{\mathrm{MC}(e^+e^- \to e^+e^-\mu^+\mu^-)} = \frac{266 \pm 16.3}{395 \pm 7.0} = 0.67 \pm 0.04$$

It can be seen from the previous pages and Appendix A, that the muon pair Monte Carlos requires the largest correction of all the Monte Carlo samples in the endcap region, while in the barrel the Bhabha Monte Carlo requires the largest correction. The muon pair Monte Carlos underestimate the background in all cases, as do the Bhabha Monte Carlos except for the 1994 endcap region. On the whole the two photon Monte Carlo samples overestimate the background and so these must be scaled down. Finally the mutlihadronic sample used for 1992, 1993 and

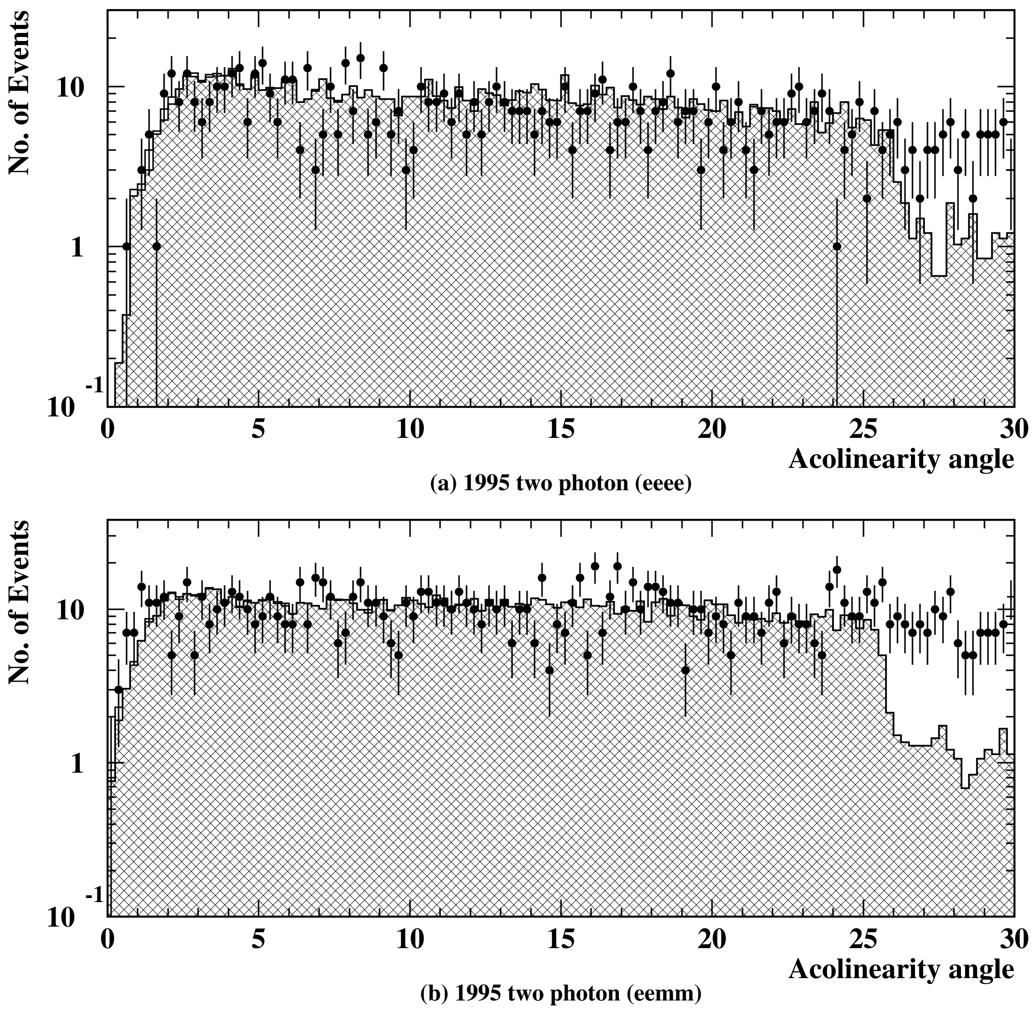

Figure 4.8: These distributions are used to check the two photon background, distribution (a) showing the $e^+e^- \rightarrow e^+e^-e^+e^-$ events while the (b) shows the $e^+e^- \rightarrow e^+e^-\mu^+\mu^-$ events. The variable plotted is acolinearity, with the region between 15 and 20 degrees being investigated for corrections. The fall off in the Monte Carlo after 26 degrees is due to a cut applied in the generation of the sample. Once again the key is similar to the muon and bhabha plots with the hatched region corresponding to the specific two photon Monte Carlo.

1994 models the background well and the sample used for 1995 overestimates it in the barrel region. The correction factors in the barrel region and endcap region are mostly of the same order for each Monte Carlo, indicating that the Monte Carlos are consistant over both angular ranges. The exception to this are the Bhabha Monte carlos which require larger correction factors in the barrel region.

These corrections are applied to background which is discussed in detail in chapter 5. It should be noted however that these corrections change the estimated background in the 95 tau sample from $(2.77 \pm 0.01)\%$ to $(3.21 \pm 0.14)\%$.

Chapter 5

Measurement of the Branching Ratios

At present OPAL has published a measurement of the topological branching ratio using data from the years 1990 and 1991 [69]. This analysis uses four years' data and also makes the measurement in the endcap region of the detector which has not been previously attempted.

5.1 Overview of analysis method

Data recorded between 1992 and 1995 were used in this analysis and the preselection cuts outlined in chapter 4 were used to select the sample of tau pairs. The analysis was done in two separate angular regions, the barrel region ($|\overline{cos\theta}| < 0.68$) and the endcap region ($0.90 > |\overline{cos\theta}| > 0.68$), where $|\overline{cos\theta}|$ is defined as the average $|cos\theta|$ of the two charged cones. The upper limit ($0.90 > |\overline{cos\theta}|$) is chosen to avoid the region close to the beam which has limited detector coverage and also to eliminate low angle scattering.

The preselection cuts yield a total of 99310 $\tau\tau$ events in the barrel region and 38659 $\tau\tau$ events in the endcap region. Four sets of Monte Carlo data [37] are used; R1508, R1513, R1520, R1535 corresponding respectively to the code versions used in years 1992, 1993, 1994 and 1995. Applying the preselection to these samples yields a total of 854485 Monte Carlo $\tau\tau$ events in the barrel region and a total of 330992 Monte Carlo $\tau\tau$ events in the endcap region. The number of events contained in each data and Monte Carlo sample are summarised in table 5.1.

Sample	Number of events in barrel region	Number of events in endcap region
Data		
1992	20506	7950
1993	19285	7495
1994	40129	15559
1995	19390	7655
Total	99310	38659
Tau Monte Carlo		
R1508	161658	62731
R1513	162897	63906
R1520	326293	126536
R1535	203637	77819
Total	854485	330992

Table 5.1: The number of data and Monte Carlo $\tau^+\tau^-$ events contained in the samples used for the analysis.

The two analyses were kept separate, since the background levels in the two regions are quite different. This is due mainly to an excess of Bhabha and muon pair events in the endcap region. Each year is also treated separately, because the Monte Carlos differ slightly from year to year (modified code and changes to calibration constants etc.). The results from the four years are finally combined however to give a weighted average.

The analysis consists of four main stages which will now be outlined and discussed in detail later in this chapter.

- Firstly the selected data are corrected for track reconstruction effects. These are effects which are not quite modelled correctly in the Monte Carlo and so must be corrected. There are two major effects, "split" tracks and "merged" tracks, the first is due to one track being reconstructed as two (see 5.2.1), and the second is where two tracks are identified as one (see 5.2.2).

- Photon conversions alter the topology of the tau decay. Conversions are extra electron pairs produced either by gamma rays (*e.g.* from π^0 decays) converting in the detector or beam pipe material or by π^0 Dalitz decays at the interaction point. These conversions can be identified with good efficiency (see 5.3) and can readily be removed, hence restoring the topology of the decay. Decays of the type $K_s^0 \to \pi^+\pi^-$ alter the topologies in a similar way to conversions however these are not rejected. Instead the Monte Carlo classifies the K_s^0 decay as a neutral track. For example a tau decay involving one charged particle and the above K_s^0 decay will be classified as a one prong decay.
- Next the background is estimated from Monte Carlo normalised to the data and is subtracted from the data. The nine toplogical bins of background free data are then used in the fitting procedure to give the tau decay branching ratios. These nine bins represent 1-1, 1-2, 1-3, 1-4, 1-5, 2-2, 2-3, 2-4 and 3-3 events[a] and are discussed in detail in section 5.5. This fitting procedure uses a reconstruction matrix method using the relevant Monte Carlo to correct for migration of topolgies due to detector and reconstruction effects. For example an event with a split track could be reconstructed as a 1-2 event whereas in reality it is a 1-1 event. From the fit the branching ratios from each year in each region of the detector are obtained.
- The systematic errors for these results are described in detail in chapter 6 and finally the four years are combined to give a weighted average for the two detector regions, this is discussed in detail in chapter 7.

Following is a more detailed description of the analysis procedure.

[a]Here a 1-1 event means an event with one charged track in each cone, a 1-2 an event with one charged track in one cone and two charged tracks in the other and so on.

5.2 Track Reconstruction Effects

5.2.1 Split tracks

Split tracks mainly occur when a track in the CJ detector is close to an anode plane. This can cause double hits in CJ and these extra hits can be reconstructed as fake tracks. Another manifestation of this anode plane effect is that when a track crosses the anode plane, it can sometimes be reconstructed as two tracks. In each case this consists of producing additional fake tracks in the sample, which have to be recognised and removed.

To show this effect the tracks were divided up into samples of cones with 1, 2, 3 and >3 prongs and the number of CJ hits for each *track* of the cone was plotted. The results for the 95 data in each region are shown in figures 5.1 and 5.2[b]. The data from other years show similar features (Appendix B). It can be seen that there is an excess of data over Monte Carlo when the number of hits is low (less than 50 hits) particularly for the unphysical topologies. The peak at 110 hits for the 1 prong cones which is seen in the data for all years except 1992 is a result of one of the CJ sectors running at a reduced efficiency. This effect was inluded in the 1994 and 1995 Monte Carlos as the CJ sector was not fixed. The peak at 159 hits in the plots correspond to the total number of sense wires in the CJ chamber and hence the maximum number of possible hits per track. This peak is present in the endcap region too, although 159 wires can only be hit up to $|cos\theta| < 0.73$, at which point the maximum number of possible hits per track decreases as:

$$\text{number of hits} = \frac{147\tan\theta}{1 - 0.268\tan\theta} - 25 \tag{5.1}$$

due to the shape of the CJ chamber (figure 2.3). This equation is only valid for $|cos\theta| > 0.73$. The equation explains the shape of the plots in the endcap, the peak at 159 hits being those tracks with $|cos\theta| < 0.73$, the plateau corresponding to tracks with the maximum number of possible hits as $|cos\theta|$ increases up to the

[b]All following plots, containing data and Monte Carlo, are normalised to the integrated luminosity.

cut off limit of 0.9, and the points below 60 hits are tracks with less hits than the maximum number of hits available.

The tracks from the unphysical topologies were investigated further by plotting the variable d_{anode}, which is defined as the difference in azimuthal angle ϕ between the nearest anode plane and the ϕ of the track at radius 104.5cm (the mid-radius of CJ). The results for the 1995 data in each region are shown in figure 5.3 and 5.4, with the other years showing a similar feature. It is seen that the data sample has a large peak at the anode plane which is missing in the Monte Carlo sample. Similar distributions can be seen for the whole data samples in figures 5.5 and 5.6 and the same excess is observed. As a further investigation of the anode plane region the data were divided into two subsets, physical and unphysical. The physical subset contained cones with one, three or five prongs and the unphysical subset contained cones with two or four prongs. The average angular distance to the anode plane of the tracks in these cones (average d_{anode}) was plotted for the two subsets. The distributions found using the 1994 data can be seen in figures 5.7 and 5.9, for the barrel and endcap respectively. Next the ratio of these distribution was plotted and the results can be seen for all years' data in figures 5.8 and 5.10. It can be seen from these distributions that close to the anode plane there is an enhancement of the data over the Monte Carlo for the unphysical topologies. This effect is directly related to the excess of two prong cones observed previously and is further evidence for the need to remove these extra tracks.

It is clear that these two effects are correlated and that the low number of CJ hits for the tracks in the data are caused by the fact that they are close to the anode plane. Now we must consider if the 2 prong cones with a low number of CJ hits are actually 1 prong cones which have been reconstructed as two tracks (split tracks). This was done by examining visually a sample of two prong events. It was seen that as one track entered CJ close to the anode wire it caused double hits, meaning that a short track was reconstructed parallel to the real track (fig. 5.11). Therefore these fake "split" tracks must be eliminated from the sample.

To eliminate these split tracks which are the cause of the effects described above the following cuts were used :

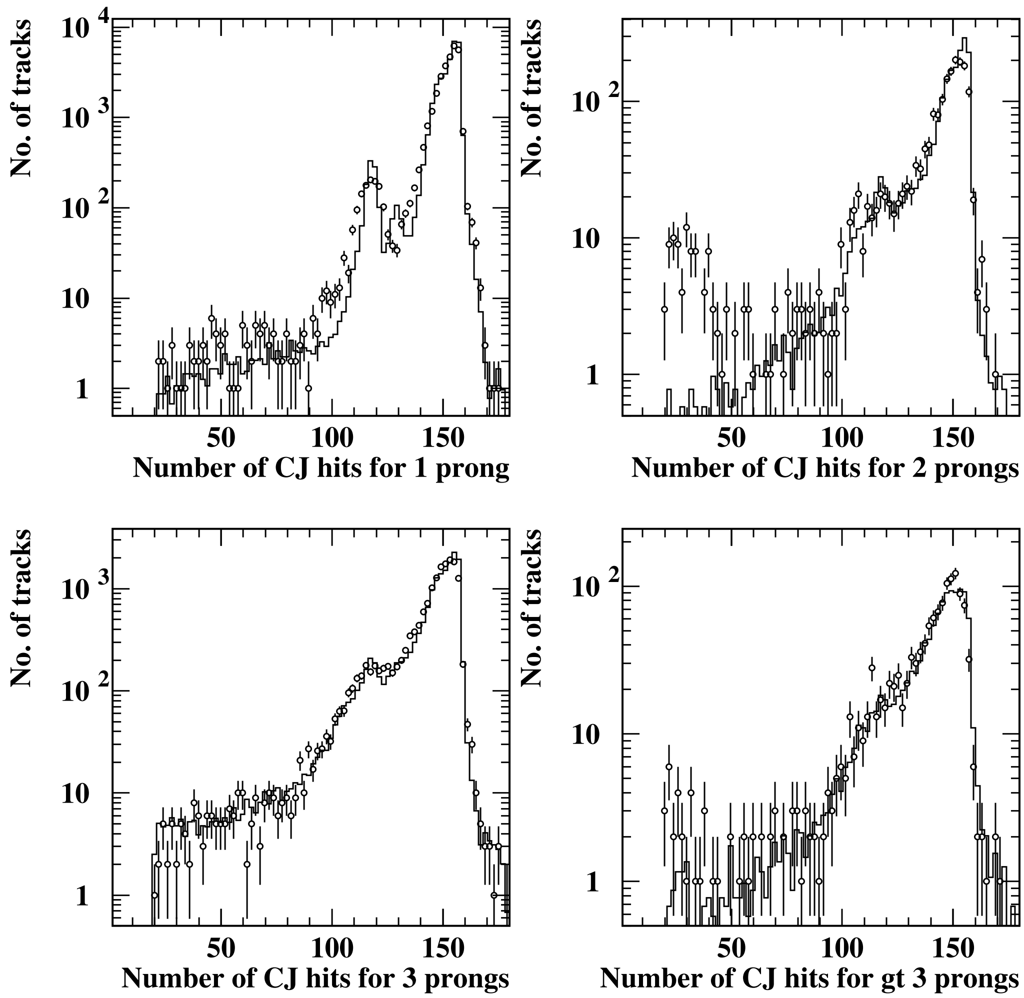

Figure 5.1: Number of hits in CJ per track for 1995 data and 1995 Monte Carlo (for barrel region). The data are represented by the points and the full line represents the Monte Carlo. This convention is adhered to in all following plots. The excess of data points over Monte Carlo at low values of number of hits is due to split tracks.

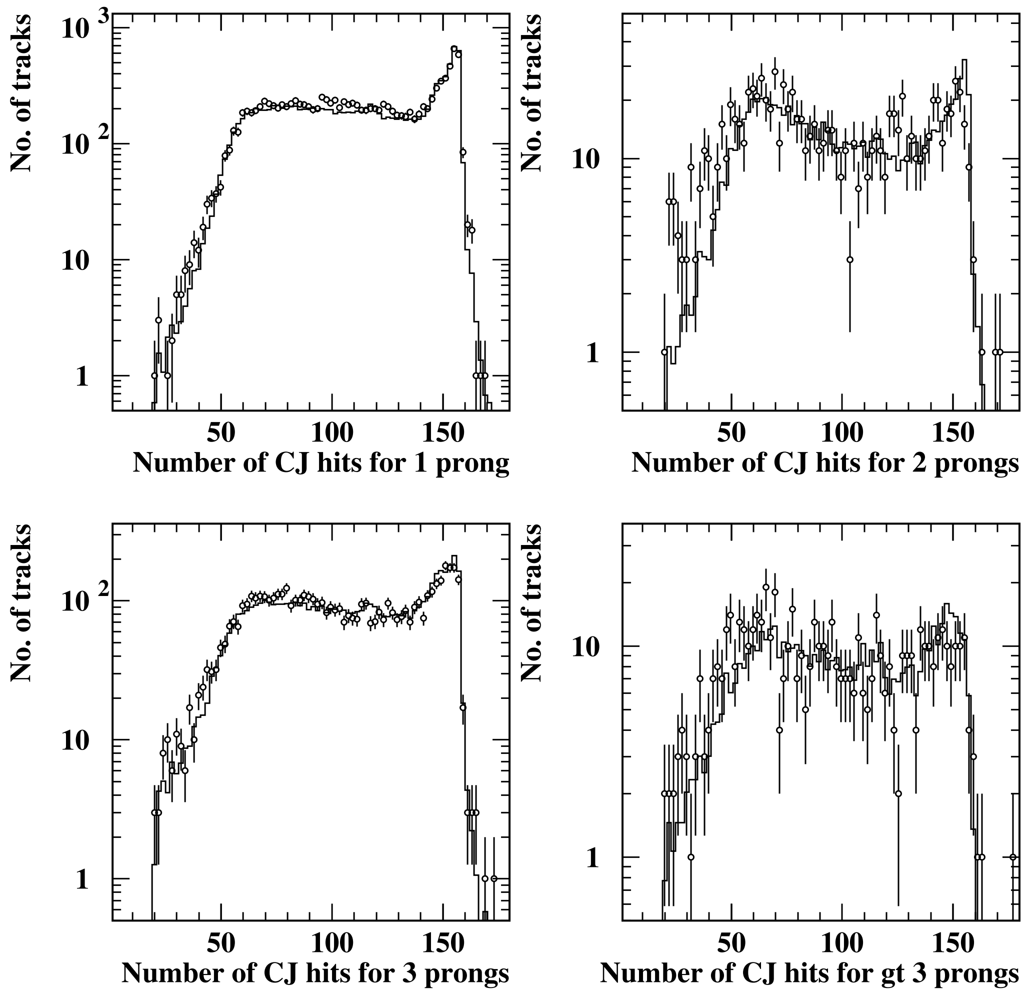

Figure 5.2: Number of hits in CJ per track for 1995 data and 1995 Monte Carlo (for endcap region). The excess of data points over Monte Carlo at low values of number of hits is due to split tracks, although this effect is not as pronounced as in the barrel region to the lower statistics. The difference in shape of these plots compared to the barrel region is due to the total possible number of hits in CJ decreasing with increasing $|cos\theta|$ (see equation 5.1 in section 5.2.1)

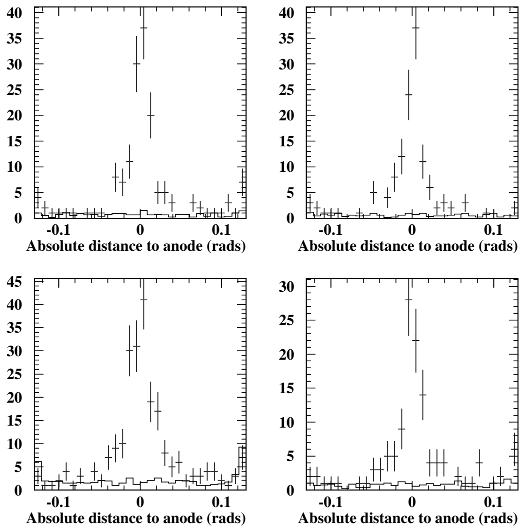

Figure 5.3: Angular distance to anode for tracks within 2 prong, or greater than 3 prong cones, with number of CJ hits per track less than 50, (for the barrel region). The distributions shown are for 1992, 1993, 1994 and 1995 data and Monte Carlo. These events correspond to the excess of data in figure 5.1.

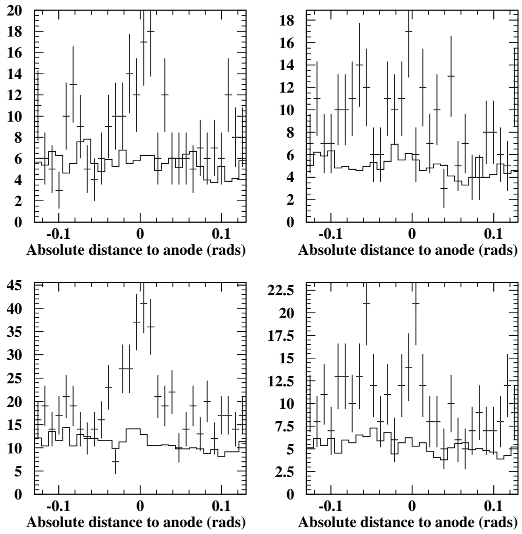

Figure 5.4: Angular distance to anode for tracks within 2 prong, or greater than 3 prong cones, with number of CJ hits per track less than 50, (for the endcap region). The distributions shown are for 1992, 1993, 1994 and 1995 data and Monte Carlo. These events correspond to the excess of data in figure 5.2.

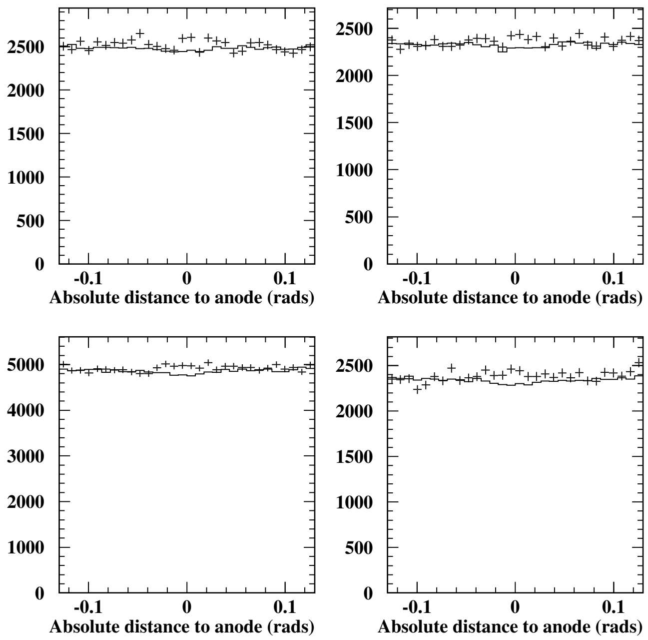

Figure 5.5: Plots of the angular distance to the anode wire in radians for 1992, 1993, 1994 and 1995 data and Monte Carlo (in the barrel region).

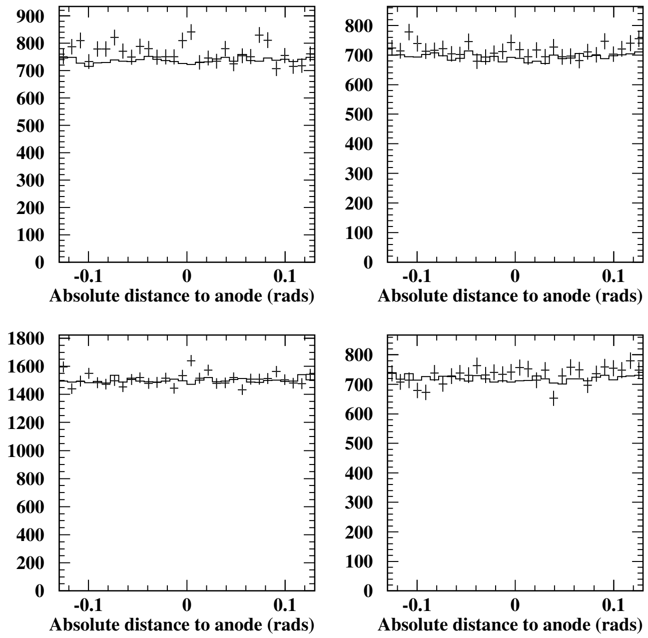

Figure 5.6: Plots of the angular distance to the anode wire in radians for 1992, 1993, 1994 and 1995 data and Monte Carlo (in the endcap region).

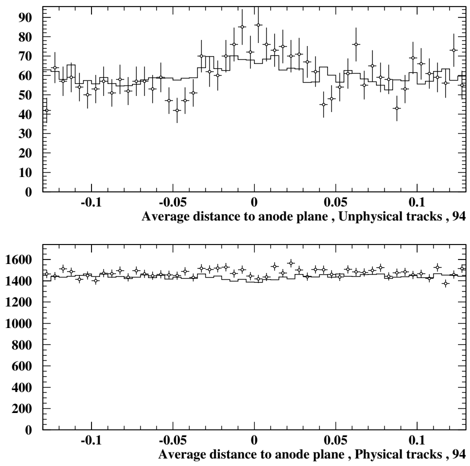

Figure 5.7: Average angular distance to the anode plane, 1994 data and Monte Carlo (in the barrel region).

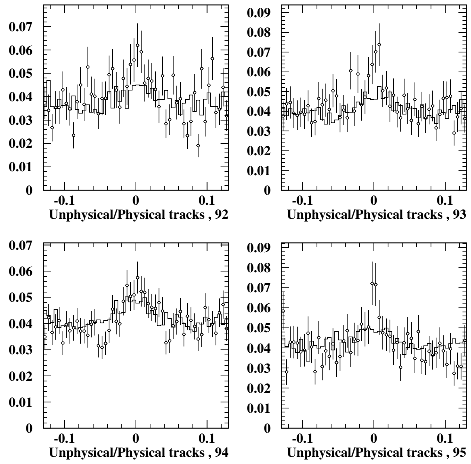

Figure 5.8: Average angular distance to anode plane of unphysical topologies divided by physical topologies for 1992, 1993, 1994 and 1995 data and Monte Carlo (in the barrel region).

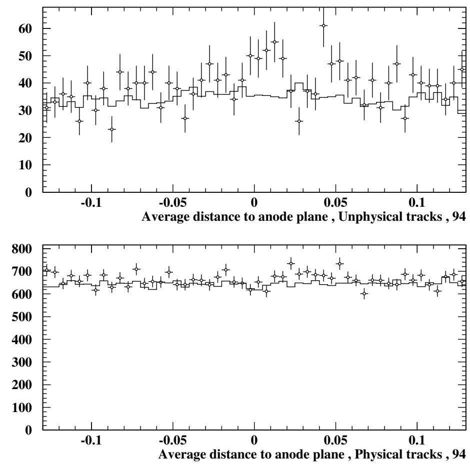

Figure 5.9: Average angular distance to the anode plane, for 1994 data and Monte Carlo in the (endcap region).

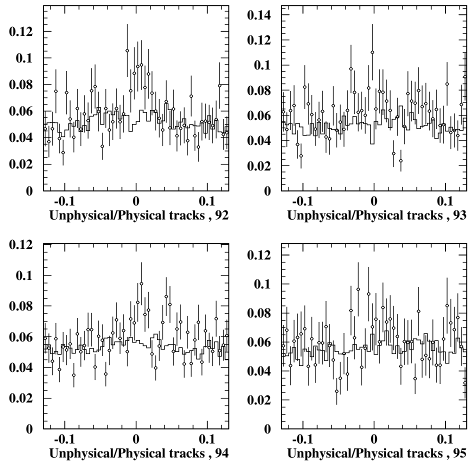

Figure 5.10: Average angular distance to anode plane of unphysical topologies divided by physical topologies for 1992, 1993, 1994 and 1995 data and Monte Carlo (in the endcap region).

CJ hits for track < 50
dE/dx of track < 5 keV/cm
Average d_{anode} of the two tracks < 0.02 radians.

The low dE/dx is again another artifact of this effect, the fake track hits do not pass the requirements made by ROPE on hits used for dE/dx measurement, hence the low value.

The plot of CJ hits after these cuts can be seen in figures 5.12 and 5.13 for 1995 in both the barrel and endcap regions. The excess of data over Monte Carlo at a low value of CJ hits is now reduced and there is a much better agreement between the data and the Monte Carlo. This indicates that the majority of the split tracks have been removed.

5.2.2 Merged tracks

Another way that the topologies can be affected is if two tracks are lying within the two hit resolution of the detector and they are reconstructed as one track. It is known that the track resolution for the Monte Carlos is worse than for the data, this being more so for 1994 and 1995 data. Therefore in the Monte Carlo there will be more events where two tracks are merged and reconstructed as one track. To correct for this a fraction of the 2 prong cones in the Monte Carlo are corrected to 3 prong cones.

A method for detecting these merged tracks is to examine the dE/dx of the tracks. One would expect a merged track to have twice the dE/dx of a normal track above the level of minimum ionisation. In this region where the dE/dx is double that of a normal track (14 to 26 keV/cm and p $>$ 2GeV/c), the number of 2 prong cones in the data and the Monte Carlo is investigated. These distributions of dE/dx for each track can be seen in figures 5.14 and 5.15. It can be seen that the correction for merged tracks need not be made in the endcap region and also for 1992 and 1993 in the barrel due to the total number of data events in the region agreeing with the Monte Carlo events within errors. It is clear however that there is an excess of Monte Carlo in the barrel region for 1994 and 1995. It is also noticed that the peak

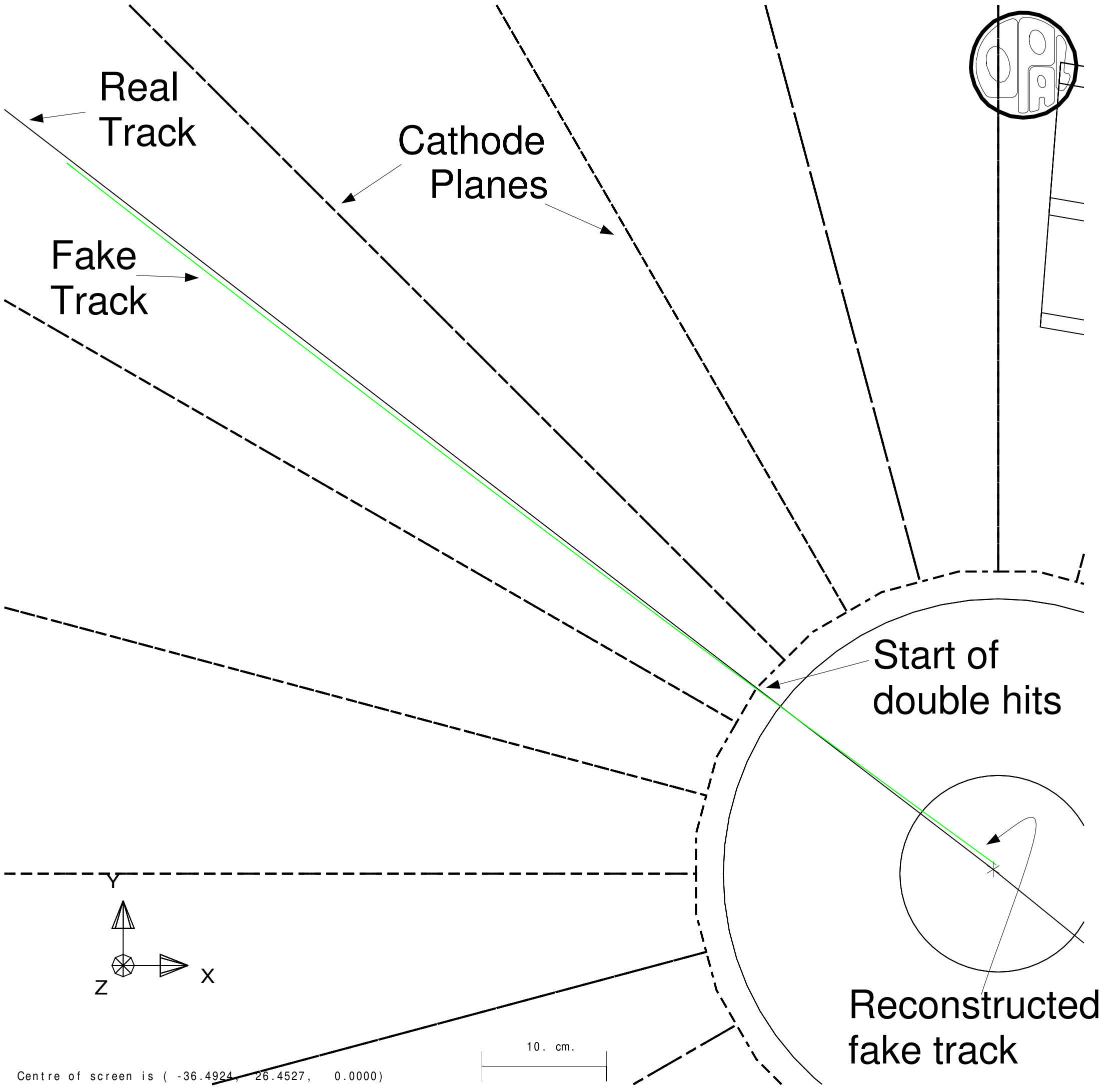

Figure 5.11: An example "split" track, caused by the real track entering the CJ chamber close and parallel to the anode plane, which in turn causes double hits which get reconstructed as a fake track. The anode planes are not shown on the diagram but lie at the angular midpoint between the cathode planes.

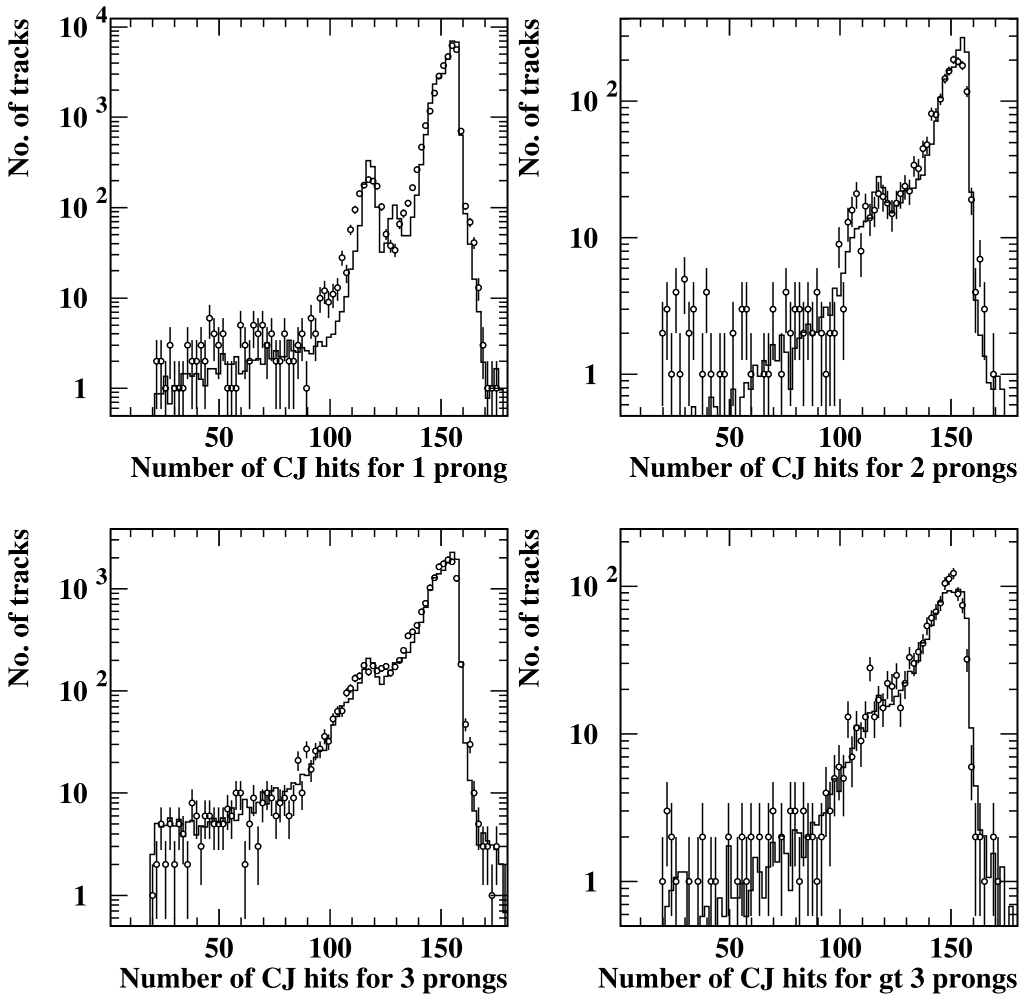

Figure 5.12: Number of hits in CJ for 95 data and Monte Carlo after the split track cuts have been implemented in the barrel region. Applying these cuts to 1992, 1993 and 1994 show very similar results.

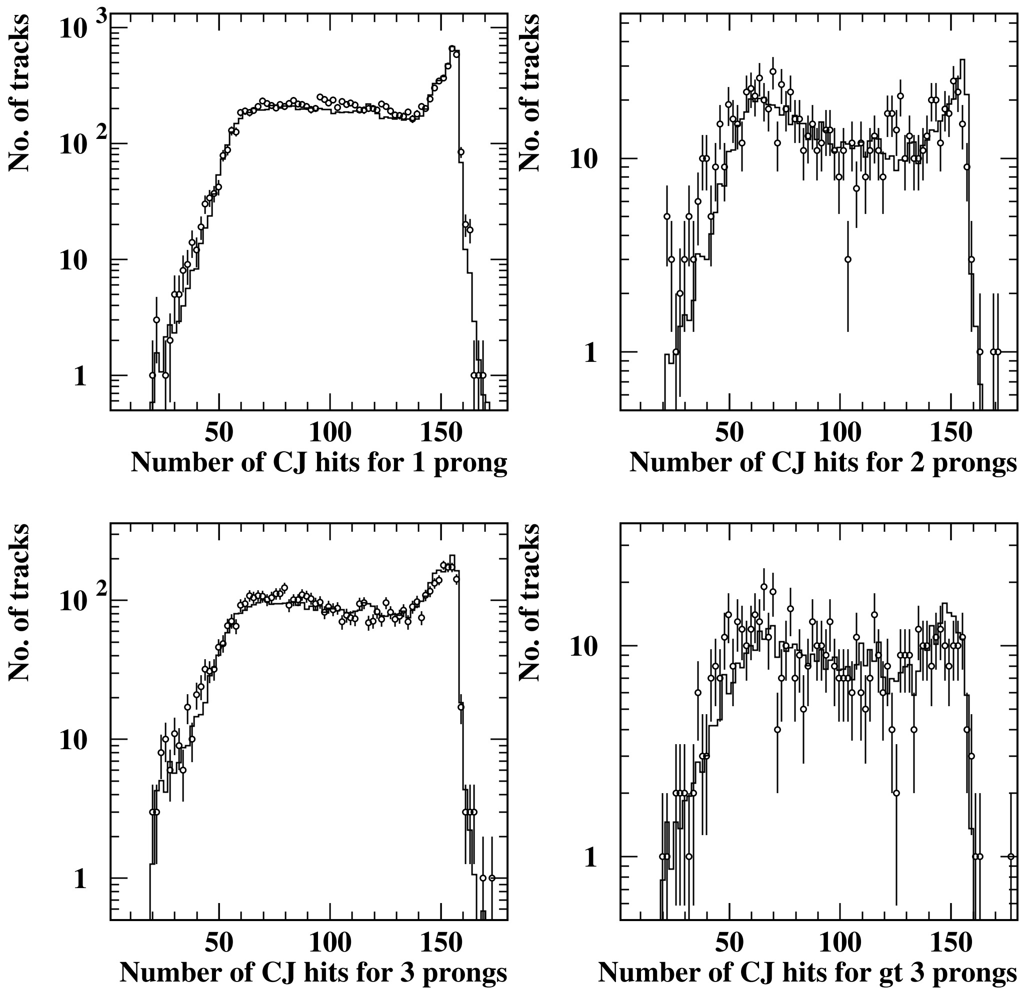

Figure 5.13: Number of hits in CJ for 1995 data and Monte Carlo after the split track cuts have been implemented in the endcap region. Applying these cuts to 1992, 1993 and 1994 show very similar results.

in the Monte Carlo is displaced slightly to towards zero, however this does not effect the merged track selection as the only concern is the total number of tracks in the region.

To calculate the correction to the Monte Carlo the number of tracks in the region, which are associated to 2 prong cones, are compared between data and Monte Carlo. The excess of Monte Carlo tracks over data tracks is then calculated as a fraction of the number of Monte Carlo tracks (ie. $\frac{Number\ of\ Monte\,Carlo\,tracks - Number\ of\ data\,tracks}{Number\ of\ Monte\,Carlo\,tracks}$). These are outlined below

94 Monte Carlo : 0.424

95 Monte Carlo : 0.447

Now the total number of 2 prong cones, which contain a track lying in the specified dE/dx region, are counted and multiplied by the above fraction. The final number arrived at is the number two prong cones which are then converted to a three prong cone in the analysis.

The introduction of these merged track corrections decreases the χ^2 for the branching ratio fit, indicating the Monte Carlo now describes the data better than before. Further investigation of this cut is conducted as a study of systemtic errors (chapter 6).

5.3 Identification of conversions

To reject conversions a conversion finder was used. For the central result the conversion finder outlined below was used. This was first outlined in [70]. For further checks two other conversion finders IDGCON [71] and IDNCON [71] were used. These are referred to in greater detail in section 6.2.

The first conversion finder uses dE/dx measurements for identification of conversions. The dE/dx measurements are obtained by measuring the amount of ionisation on each wire in CJ and then a truncated mean is used (see section 2.2.1). A summary of the first conversion finder now follows:

(a) The first procedure looks at pairs of oppositely charged particles in each τ

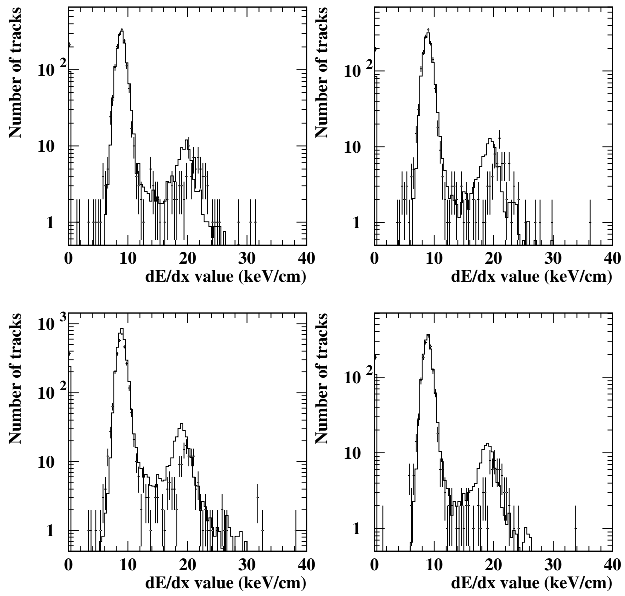

Figure 5.14: Distribution of dE/dx, for each track, for 2 prong cones in the barrel region. The plots shown are for 1992, 1993, 1994 and 1995 data and Monte Carlo. It can be seen that 1994 and 1995 have an excess of Monte Carlo over data in the region between 14 kev/cm and 26 keV/cm due to an excess of merged tracks.

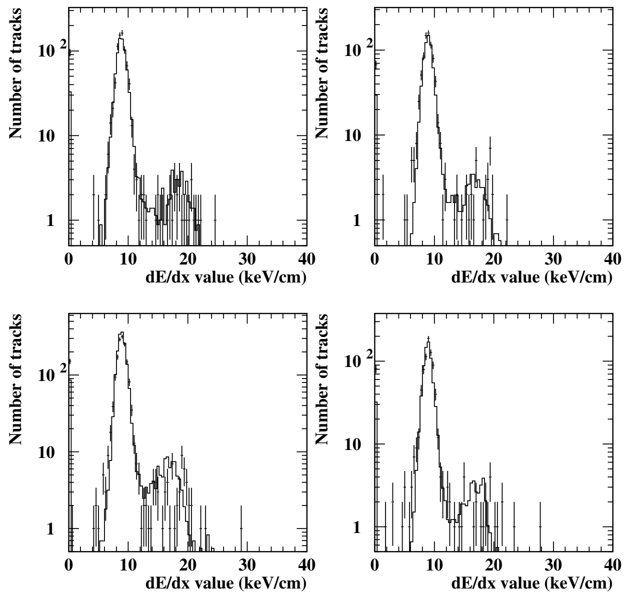

Figure 5.15: Distribution of dE/dx, for each track, for 2 prong cones in the endcap region. The plots shown are for 1992, 1993, 1994 and 1995 data and Monte Carlo. It can be seen that there is good agreement between data and Monte Carlo in the region between 14 keV/cm and 26 keV/cm.

cone and calculates their closest approach in the xy plane. For the pair with the minimum value of the separation (≤ 0.3 cm.), if the lower momentum particle of the pair has an energy loss consistent with that of an electron (or positron), then that pair is flagged as a conversion. A scaled energy loss parameter is calculated, based on the dE/dx values obtained from assuming electron and pion hypotheses for the track. This rescaled energy loss, $(dE/dx)_r$, is the fractional difference of the track dE/dx from that of a pion, with respect to the e-π difference.

$$(dE/dx)_r = [dE/dx - (dE/dx)_\pi]/[(dE/dx)_e - (dE/dx)_\pi]$$

To identify electrons the following cut is used:

$$(dE/dx)_r > 0.5$$

where $(dE/dx)_\pi$ is defined as the energy loss associated with a pion and $(dE/dx)_e$ is defined as the energy loss associated with an electron. Plots of these normalised dE/dx distributions can be seen in chapter 6 where they are discussed in length. This pair of tracks is removed from the τ cone and a further search is made for a second conversion pair. This is important for the events where high numbers of charged tracks in a cone could come from gamma conversions in the abundant 1-prong τ decays and cause significant cross-talk effects. Extra tracks could also come from the Dalitz decay of π^0s.

(b) Reconstructed events can have even prong topologies due to split tracks, missing tracks, interactions and delta rays. For all even prong cones remaining after the pair conversion search described in (a), the track with the lowest momentum is found and is classified as an electron (positron) if its rescaled energy loss satisfies

$$(dE/dx)_r > 0.5$$

The tracks classified as electrons are then removed from the sample (for example a two prong cone may then become a one prong cone).

The conversion finder was run on the Monte Carlo samples to calculate its efficiency. As it is known in the Monte Carlo exactly which tracks are from conversions, it is a simple matter to compare these to the tracks the finder flags. It was found that the conversion finder was (89.5±0.1)% efficient and the sample of selected e^+e^- pairs was (70.5±0.1)% pure (*i.e.*29.5% of rejected conversions are in fact multihadronic events), where the errors are statistical. The efficiency can also be estimated from background Monte Carlo $\mu^+\mu^-$ events which survive the τ-pair event selection cuts. Clearly these Monte Carlo $\mu^+\mu^-$ events should all fall into the 1-1 bin, therefore by analysing with and without conversion finding and comparing how many events move into the 1-1 bin one can calculate an efficiency. The method produces an efficiency estimate of $(90 \pm 4)\%$.

5.4 Background Subtraction

Although the events selected by the tau selection are relatively pure there are some non $\tau\tau$ backgrounds present. Estimates for these have been obtained from Monte Carlo studies, where the dominant processes are $e^+e^- \to e^+e^-, \mu^+\mu^-$, two-photon processes $e^+e^- \to (e^+e^-)X$ (where X$\to e^+e^-, \mu^+\mu^-$), and $e^+e^- \to q\bar{q}$. The backgrounds are given by using the selection cuts for the $\tau\tau$ events on the Monte Carlo and scaling to the integrated luminosity of the data. The backgrounds estimated from the $\tau\tau$ Monte Carlo samples are presented in the nine topological bins with the data, given in tables 5.2 and 5.3. It has been necessary to scale the calculated backgrounds by correction factors outlined in section 4.5 because of small modelling errors in the Monte Carlo simulation. The background can also be summarised in percentage fractions of the data samples, found in table 5.4. This is useful for comparison to other analyses, and they agree well with other measurements made by OPAL. Apart from the multihadronic background, which dominates the event topologies from (1-2) and higher, the other backgrounds appear in the (1-1) bin.

5.5 Branching Ratio Fit

Two methods were used to analyse the branching ratios. The main method is event based and uses a chi-squared fit to all nine topological bins while the other alternative method is a hemisphere based analysis and uses only physical topologies. This alternative method (outlined in section 6.4) was carried out as a check on the results obtained from the preferred main method. Following is an outline of the main method.

After selection, conversion rejection and background subtraction the number of charged tracks in each cone of each event is counted. The data then falls into 9 topological bins n_{ij}^{meas}. The estimated backgrounds have been subtracted from the data for these numbers.

To calculate the branching ratios the following minimum χ^2 fit is used:

$$\chi^2 = \left(\frac{n_{ij}^{meas} - n_{ij}^{fit}}{\sigma}\right)^2$$

where

$$n_{ij}^{fit} = \sum\nolimits_{k,l} \epsilon_{kl\to ij} N_{kl}$$

and $\epsilon_{kl\to ij}$ is the probability of a $\tau\tau$ event with a generated topology, kl, being reconstructed as an ij topology (tables 5.5 and 5.6). Values for $\epsilon_{kl\to ij}$ are obtained from the Monte Carlo events. The sum for each initial kl topology is less than 100% because these barrel or endcap efficiencies are expressed as a fraction of the events generated over the total angular range.

Now

$$N_{kl} = (2 - \delta_{kl}) B_k B_l N_{tot}$$

therefore the χ^2 fit is performed by allowing B_3, B_5 and N_{tot} to vary and with the constraint that

$$B_1 + B_3 + B_5 = 1.0$$

The results for the branching ratios are summarised in table 5.7, with the values fitted to the nine topological bins shown in table 5.2 for the barrel region and table 5.3 for the endcap. The errors on these fits are also given in these tables, and are only significant for the 1-1 and 1-3 topologies, although still within the statistical errors on the data in these bins. It can be seen that the results for each years' data agree very well with each other, in both the barrel and the endcap, with low χ^2s indicating a good fit. It must be noted that the errors for B1 and B3 are highly correlated.

The largest χ^2 belongs to the 1995 data result in the endcap region. Although it is larger than the other results it is still below 3/degree of freedom. The results from the barrel and endcap regions also agree very well with the only discrepancy being that the B5 results for 1992 and 1993 are almost twice as large in the endcap region as the barrel region. This difference however is still within two standard deviations. The following chapter will estimate systematic errors for these branching ratios.

	1992 data				1993 data		
i-j	n_{ij}^{meas}	n_{ij}^{B}	n_{ij}^{fit}	i-j	n_{ij}^{meas}	n_{ij}^{B}	n_{ij}^{fit}
1-1	14807	258±18	14560±55	1-1	13932	239±8	13695±56
1-2	563	8±3	602±4	1-2	539	8±2	578±3
1-3	4567	11±3	4516±51	1-3	4295	10±3	4210±53
1-4	81	11±3	60±1	1-4	66	10±3	62±1
1-5	50	5±2	48±1	1-5	63	5±2	56±1
2-2	13	7±2	5±0	2-2	8	6±2	6±0
2-3	83	17±4	82±1	2-3	78	16±3	72±1
2-4	13	14±3	1±0	2-4	11	13±3	2±0
3-3	329	9±3	323±2	3-3	293	8±2	291±2
Total	20506	340±20	20197±75	Total	19285	315±11	18972±77
	1994 data				1995 data		
i-j	n_{ij}^{meas}	n_{ij}^{B}	n_{ij}^{fit}	i-j	n_{ij}^{meas}	n_{ij}^{B}	n_{ij}^{fit}
1-1	29021	1018±21	27943±116	1-1	13945	706±8	13664±118
1-2	1091	26±6	1241±7	1-2	558	23±1	617±8
1-3	8846	28±7	8693±96	1-3	4301	27±1	4258±66
1-4	168	24±7	138±2	1-4	84	24±1	63±2
1-5	111	13±7	98±1	1-5	49	13±1	49±1
2-2	19	16±5	15±0	2-2	17	16±1	7±0
2-3	170	39±8	131±1	2-3	88	39±2	81±1
2-4	23	32±7	3±0	2-4	11	32±2	1±0
3-3	680	21±6	614±3	3-3	337	21±1	308±3
Total	40129	1217±28	388876±151	Total	19390	901±9	19048±151

Table 5.2: The measured number of events with each topology, n_{ij}, the estimated distribution for the background, n_{ij}^{B}, and the predicted number of events in each topology from the Monte Carlo using the fitted branching ratios, $n_{ij}^{fit} = \sum_{kl} \epsilon_{kl \rightarrow ij} N_{kl}$ (for the barrel region) (see section 5.5).

	1992 data				1993 data		
i-j	n_{ij}^{meas}	n_{ij}^{B}	n_{ij}^{fit}	i-j	n_{ij}^{meas}	n_{ij}^{B}	n_{ij}^{fit}
1-1	5878	165±10	5727±14	1-1	5579	169±6	5421±12
1-2	272	5±2	261±1	1-2	241	3±2	230±1
1-3	1621	3±2	1601±10	1-3	1498	2±2	1490±10
1-4	47	1±1	41±1	1-4	45	1±1	33±1
1-5	28	1±1	28±1	1-5	30	1±1	32±1
2-2	8	1±1	3±0	2-2	6	1±1	1±0
2-3	29	5±2	27±1	2-3	30	4±2	25±1
2-4	4	3±2	1±0	2-4	1	3±2	1±0
3-3	63	3±2	70±1	3-3	65	2±1	71±1
Total	7950	187±11	7760±17	Total	7495	186±7	7304±16
	1994 data				1995 data		
i-j	n_{ij}^{meas}	n_{ij}^{B}	n_{ij}^{fit}	i-j	n_{ij}^{meas}	n_{ij}^{B}	n_{ij}^{fit}
1-1	11532	371±8	11168±20	1-1	5734	182±6	5548±15
1-2	494	8±4	509±1	1-2	249	5±1	244±1
1-3	3194	6±3	3149±17	1-3	1509	5±1	1505±9
1-4	86	3±2	67±1	1-4	35	4±1	30±1
1-5	52	3±2	53±1	1-5	20	1±1	19±1
2-2	7	3±2	6±0	2-2	2	3±1	3±0
2-3	52	11±4	55±1	2-3	28	7±1	25±1
2-4	5	8±4	2±0	2-4	2	5±1	1±0
3-3	137	6±3	137±1	3-3	76	1±1	65±1
Total	15559	419±12	15146±26	Total	7655	213±7	7440±18

Table 5.3: The measured number of events with each topology, n_{ij}, the estimated distribution for the background, n_{ij}^{B}, and the predicted number of events in each topology from the Monte Carlo using the fitted branching ratios, $n_{ij}^{fit} = \sum_{kl} \epsilon_{kl \to ij} N_{kl}$ (for the endcap region)(see section 5.6).

background	contamination (%) of tau sample in barrel region due to background	contamination (%) of tau sample in endcap region due to background
$e^+e^- \to e^+e^-$	0.41±0.07	0.63±0.01
$e^+e^- \to \mu^+\mu^-$	0.72±0.04	1.07±0.01
$e^+e^- \to e^+e^-e^+e^-$	0.07±0.01	0.29±0.01
$e^+e^- \to e^+e^-\mu^+\mu^-$	0.08± 0.01	0.27± 0.01
$e^+e^- \to q\bar{q}$	0.42± 0.05	0.33± 0.01
Total	1.70±0.10	2.59±0.02

Table 5.4: Monte Carlo estimates of background contamination in the $\tau\tau$ events. Numbers are an average over the four years data samples. Except for the multi-hadronic background, which contributes to the higher multiplicity bins, the majority of the other background contributes solely to the 1-1 bin.

$\epsilon_{kl\to ij}$(%)	1992 detector			
ij	kl=1–1	kl=1–3	kl=1–5	kl=3–3
1–1	53.29±0.12	3.75±0.07	0.90±0.35	0.25±0.07
1–2	0.50±0.02	4.80±0.08	2.56±0.59	0.41 ±0.08
1–3	0.69±0.02	44.34±0.19	9.22 ±1.08	5.26±0.29
1–4	<0.1	0.42±0.02	11.78±1.20	¡0.1
1–5	<0.1	0.24±0.02	20.36±1.49	0
2–2	<0.1	<0.1	0	0.31±0.07
2–3	<0.1	0.22±0.02	0	6.93±0.33
2–4	<0.1	<0.1	0	<0.1
3–3	<0.1	0.28±0.02	0	33.75±0.62

$\epsilon_{kl\to ij}$(%)	1993 detector			
ij	kl=1–1	kl=1–3	kl=1–5	kl=3–3
1–1	53.45±0.11	4.12±0.07	1.00±0.38	0.25±0.06
1–2	0.58±0.02	4.79±0.08	2.43±0.58	0.80±0.12
1–3	0.82±0.02	44.42±0.18	11.59±1.21	5.60±0.28
1–4	<0.1	0.44±0.02	9.73±1.12	<0.1
1–5	<0.1	0.24±0.02	23.18±1.59	0
2–2	<0.1	<0.1	0	0.43±0.08
2–3	<0.1	0.24±0.02	0	6.22±0.30
2–4	<0.1	<0.1	0 <0.1	0.11±0.04
3–3		0.31±0.02	0	33.12±0.58

$\epsilon_{kl\to ij}$(%)	1994 detector			
ij	kl=1–1	kl=1–3	kl=1–5	kl=3–3
1–1	53.06±0.08	4.22±0.05	1.48±0.35	0.31±0.04
1–2	0.55±0.01	4.01±0.06	1.38±0.51	0.60±0.07
1–3	0.90±0.01	44.63±0.13	14.00±0.94	6.34±0.19
1–4	<0.1	0.50±0.02	10.64±1.02	<0.1
1–5	<0.1	0.23±0.01	21.87±1.33	0
2–2	<0.1	<0.1	0	0.27±0.06
2–3	<0.1	0.25±0.01	<0.1	5.68±0.24
2–4	0	<0.1	0	<0.1
3–3	<0.1	0.32±0.01	0	34.19±0.43

$\epsilon_{kl\to ij}$(%)	1995 detector			
ij	kl=1–1	kl=1–3	kl=1–5	kl=3–3
1–1	54.74±0.08	4.38±0.05	1.58±0.35	0.31±0.04
1–2	0.59±0.01	4.20±0.06	0.70±0.51	0.52±0.07
1–3	0.79±0.01	46.49±0.13	12.62±0.94	6.22±0.19
1–4	<0.1	0.49±0.02	12.98±1.02	<0.1
1–5	<0.1	0.26±0.01	21.23±1.33	0
2–2	<0.1	<0.1	0	0.38±0.06
2–3	<0.1	0.22±0.01	0.21	5.96±0.24
2–4	0	<0.1	0	<0.1
3–3	<0.1	0.27±0.01	0.18	36.92±0.43

Table 5.5: The efficiency and cross-contamination between decay modes,$\epsilon_{kl\to ij}$, estimated from Monte Carlo studies for the 1992, 1993, 1994 the 1995 detector configuration in the barrel region. Errors are statistical only. The sum for each initial *kl* topology is less than 100% because these barrel efficiencies are expressed as a fraction of the events generated over the total angular range.

$\epsilon_{kl\to ij}$(%)	1992 detector			
ij	kl=1-1	kl=1-3	kl=1-5	kl=3-3
1-1	21.16±0.08	1.36±0.04	0.38±0.22	<0.1
1-2	0.35±0.01	1.74±0.05	0.77±0.31	0.11 ±0.04
1-3	0.46±0.01	15.30±0.13	2.82±0.59	1.31±0.15
1-4	<0.1	0.27±0.02	3.59±0.67	<0.1
1-5	<0.1	0.11±0.01	7.55±0.95	0
2-2	<0.1	<0.1	0	0.16±0.05
2-3	<0.1	0.12±0.01	0	1.76±0.17
2-4	<0.1	<0.1	0	<0.1
3-3	<0.1	<0.1	0	7.08±0.33
$\epsilon_{kl\to ij}$(%)	1993 detector			
ij	kl=1-1	kl=1-3	kl=1-5	kl=3-3
1-1	21.55±0.01	1.39±0.04	0.29±0.20	0.12±0.04
1-2	0.33±0.01	1.68±0.05	1.29±0.43	<0.1
1-3	0.47±0.01	15.84±0.14	3.15±0.66	1.53±0.15
1-4	<0.1	0.20±0.02	3.58±0.70	<0.1
1-5	<0.1	0.11±0.01	7.87±1.02	0
2-2	<0.1	<0.1	0	<0.1
2-3	<0.1	0.12±0.01	0	1.90±0.17
2-4	<0.1	<0.1	<0.1	<0.1
3-3		0.11±0.01	0	8.07±0.34
$\epsilon_{kl\to ij}$(%)	1994 detector			
ij	kl=1-1	kl=1-3	kl=1-5	kl=3-3
1-1	21.23±0.06	1.11±0.03	0.30±0.17	<0.1
1-2	0.34±0.01	1.77±0.04	0.30±0.17	0.13±0.03
1-3	0.48±0.01	15.56±0.10	2.76±0.51	0.93±0.09
1-4	<0.1	0.25±0.01	2.86±0.52	<0.1
1-5	<0.1	0.12±0.01	7.09±0.81	0
2-2	<0.1	<0.1	0	0.12±0.03
2-3	<0.1	0.11±0.01	<0.1	0.12±0.13
2-4	0	<0.1	0	<0.1
3-3	<0.1	0.11±0.01	0	6.94±0.23
$\epsilon_{kl\to ij}$(%)	1995 detector			
ij	kl=1-1	kl=1-3	kl=1-5	kl=3-3
1-1	21.72±0.01	1.12±0.01	0.53±0.01	<0.1
1-2	0.35±0.01	1.76±0.01	0.53±0.01	0.10±0.01
1-3	0.46±0.01	15.72±0.01	1.93±0.01	1.17±0.01
1-4	<0.1	0.24±0.01	3.51±0.01	<0.1
1-5	<0.1	0.10±0.01	8.95±0.01	0
2-2	<0.1	<0.1	0	0.12±0.01
2-3	<0.1	0.11±0.01	<0.1	1.96±0.01
2-4	0	<0.1	0	<0.1
3-3	<0.1	0.12±0.01	0	7.25±0.01

Table 5.6: The efficiency and cross-contamination between decay modes, $\epsilon_{kl\to ij}$, estimated from Monte Carlo studies for the 1992, 1993, 1994 the 1995 detector configuration in the endcap region. Errors are statistical only. The sum for each initial kl topology is less than 100% because these endcap efficiencies are expressed as a fraction of the events generated over the total angular range.

Data	Monte Carlo	Barrel Region				Endcap Region			
		$B_1(\%)$	$B_3(\%)$	$B_5(\%)$	χ^2/dof	$B_1(\%)$	$B_3(\%)$	$B_5(\%)$	χ^2/dof
1992	1992	84.57±0.21	15.29±0.20	0.139±0.053	5/6	84.42±0.37	15.25±0.36	0.325±0.107	5/6
1993	1993	84.70±0.22	15.09±0.21	0.206±0.055	10/6	84.83±0.37	14.75±0.36	0.424±0.114	9/6
1994	1994	84.56±0.15	15.28±0.15	0.157±0.046	4/6	84.59±0.27	15.15±0.26	0.260±0.086	8/6
1995	1995	84.55±0.22	15.29±0.21	0.158±0.052	5/6	85.00± 0.37	14.86± 0.37	0.134± 0.082	16/6

Table 5.7: Branching ratios for the 1992, 1993, 1994 and 1995 data and Monte Carlos. It must be noted that the errors on B1 and B3 are highly correlated.

Chapter 6

Systematic Studies

This chapter outlines the systematic studies investigated for the analysis. The main areas of systematic uncertainty can be grouped into four areas. Firstly is track reconstruction, which includes detecting split tracks and merged tracks. The sensitivity of the branching ratios to these sets of cuts must be estimated by varying them. The second area is identifying and removing conversions. To investigate this area the criteria for the conversion identification are varied and two alternative conversion finders are used as a check. Event selection is also another source of systematic uncertainty, the angular region from which the tau sample is selected is varied for this error. Finally there are uncertainties in the estimated background which is varied to derive a systematic error for this effect. This chapter outlines these systematic errors and contains a detailed account of how they were obtained.

6.1 Track Reconstruction

Several effects come under the banner of track reconstruction effects, all of which are described below.

6.1.1 Split and Merged Tracks

The cuts used to correct for these effects were varied to examine the sensitivity of the final results to them. For the split track effect the distance to the anode plane, the maximum dE/dx value and number of hits in CJ were varied, all of which define a split track as discussed in detail in section 5.2.1. The distance from the anode plane was varied from 0.01 radians to 0.03 radians, the maximum dE/dx was varied up to 10 KeV/cm and the number of CJ hits was varied from 20 to 50 hits. For the track merging effect the region in dE/dx over which a track is tagged as merged was varied by allowing the upper and lower limits to vary by $\pm$2KeV/cm.

The results are shown in summary tables (table 6.1 for the barrel region and table 6.2 for the endcap region). It can be seen that varying the parameters in the merged track cut makes only a small difference. However varying the parameters in the split track identification, (from the defaults of less than 50 CJ hits, less than 5keV/cm per track energy loss and average distance to the anode plane of less than 0.02 radians), changes the endcap result by up to ($\pm$0.21)% with little difference in the result for the barrel region.

This change in result is seen in the endcap region and not the barrel region due to the decrease in the maximum number of CJ hits available as $|cos\theta|$ increases (section 5.2). As the range of the split track identification parameters is increased a larger proportion of tracks in the endcap become classified as a split track. This is due to more tracks falling beneath the limit on the number of hits per track (set at 50 hits) used to identify split tracks. Fewer hits per track may also have an effect on the dE/dx measurement as the total number of hits available for this measurement is reduced and some of these may not pass the ROPE requirements necessary. If the result is that none of these hits can be used for the dE/dx measurement then the track will be classified as having zero dE/dx. In turn the number of tracks classified as split will increase due to the limit of 5 keV/cm on the identification cuts.

6.1.2 Anode Plane Effect (Anode wires and CJ hits)

To examine further the effect of the split track cut the region around the anode plane was investigated. To examine the significance of the effect the region concerned was excluded from the analysis, first by requiring that the number of CJ hits per track be greater than 50 and then by requiring that the distance from the anode plane of each track be greater than 0.02 radians. These values were then varied down to 20

	B1(%)				B3(%)				B5(%)			
	92	93	94	95	92	93	94	95	92	93	94	95
Conversion Finder: dE/dx cut	±0.04	±0.02	±0.02	±0.05	±0.05	±0.02	±0.01	±0.04	±0.015	±0.004	±0.007	±0.010
$\pi^0 s$	±0.04	±0.02	±0.03	±0	±0.05	±0.02	±0.02	±0	±0.015	±0.004	±0.003	±0
Anode/CJ	±0.12	±0.15	±0.08	±0.02	±0.07	±0.12	±0.07	±0.03	±0.045	±0.050	±0.040	±0.001
Split Tracks	±0.02	±0.02	±0.02	±0.01	±0.02	±0.02	±0.01	±0.02	±0.001	±0	±0	±0
Merged Tracks	±0	±0	±0.10	±0.10	±0	±0	±0.10	±0.10	±0	±0	±0.005	±0.005
Track Separation	±0.01	±0.01	±0	±0.01	±0.01	±0.01	±0	±0.01	±0.001	±0.002	±0	±0.002
Event Selection	±0.06	±0.02	±0.05	±0.05	±0.04	±0.02	±0.05	±0.05	±0.020	±0.030	±0.034	±0.009
Lepton bg	±0.04	±0.02	±0.02	±0.02	±0.04	±0.02	±0.04	±0.03	±0.002	±0.001	±0.001	±0
Multih. bg	±0.05	±0.05	±0.05	±0.05	±0.04	±0.03	±0.03	±0.04	±0.030	±0.017	±0.017	±0.011
Total	±0.17	±0.16	±0.15	±0.14	±0.11	±0.13	±0.14	±0.13	±0.060	±0.064	±0.056	±0.018

Table 6.1: Summary of systematic errors in the barrel region.

	B1(%)				B3(%)				B5(%)			
	92	93	94	95	92	93	94	95	92	93	94	95
Conversion Finder: dE/dx cut	± 0.03	± 0.01	± 0.08	± 0.07	± 0.04	± 0.01	± 0.04	± 0.07	± 0.017	± 0.014	± 0.032	± 0.007
$\pi^0 s$	± 0.06	± 0.15	± 0.13	± 0	± 0.05	± 0.13	± 0.07	± 0	± 0.007	± 0.030	± 0.017	± 0
Anode/CJ	± 0.13	± 0.02	± 0.16	± 0.09	± 0.15	± 0.06	± 0.16	± 0.10	± 0.024	± 0.025	± 0.035	± 0.012
Split Tracks	± 0.13	± 0.06	± 0.21	± 0.12	± 0.13	± 0.05	± 0.20	± 0.09	± 0.002	± 0.02	± 0.006	± 0
Merged Tracks	± 0	± 0	± 0	± 0	± 0	± 0	± 0	± 0	± 0	± 0	± 0	± 0
Track Separation	± 0.13	± 0.05	± 0.20	± 0.10	± 0.12	± 0.05	± 0.20	± 0.10	± 0.013	± 0.005	± 0.003	± 0.012
Event Selection	± 0.08	± 0.04	± 0.07	± 0.02	± 0.12	± 0.01	± 0.07	± 0	± 0.025	± 0.021	± 0.002	± 0.014
Lepton bg	± 0.04	± 0.03	± 0.04	± 0.06	± 0.04	± 0.03	± 0.04	± 0.06	± 0.001	± 0.001	± 0.002	± 0.002
Multih. bg	± 0.03	± 0.05	± 0.06	± 0.04	± 0.02	± 0.02	± 0.05	± 0.04	± 0.022	± 0.026	± 0.012	± 0.001
Total	± 0.25	± 0.18	± 0.38	± 0.21	± 0.27	± 0.16	± 0.35	± 0.20	± 0.047	± 0.054	± 0.052	± 0.023

Table 6.2: Summary of systematic errors in the endcap region.

hits and zero distance. It seems clear that if the anode region is cut out the analysis should be unaffected by split tracks and therefore give results as a "perfect" albeit lower statistics analysis. However once the anode region is discarded it is found that the Monte Carlo has an excess number of events in the 1-2 bin. This effect was also noted in the published paper [69] and an error was assigned to it. Therefore the systematic error derived from discarding the anode region can also be considered as a systematic error for the incorrect modelling of 1-2 events in the Monte Carlo. The results for the barrel and endcap region are shown in tables 6.1 and 6.2.

6.1.3 Track Separation

The distributions of the closest separation in position at the mid radius of CJ and the difference in phi at the vertex between two tracks, in data and Monte Carlo, are shown in figures 6.1, 6.2, 6.3 and 6.4. The Monte Carlo slightly underestimates the number of events at low separation in all years but 1994 where there is a slight excess of Monte Carlo over data, as seen in the figures. In order to examine what effect this incorrect modelling has on the branching ratios the result is evaluated as a function of a cut on the closest two track separation. If the smallest separation between two tracks is less than the cut then the total number of tracks in that cone is reduced by one. The cut was varied over a range, from zero up to 1cm. The resulting changes in branching ratios for the barrel and endcap region are shown in tables 6.1 and 6.2. It is noted that this cut has an insignificant effect on the results in the barrel region but a visible effect on the results in the endcap region.

6.2 Conversion finding

Three different conversion finders were studied to estimate the systematic error contribution from this source. The tracks which were flagged due to conversions were checked using the Monte Carlo tree variables. These numbers were then used to calculate the efficiencies and purities. The additional conversion finders to the one used for the main analysis were, IDGCON [71] and IDNCON [71]. IDNCON uses an neural network which has been trained to identify conversions and a simple cut

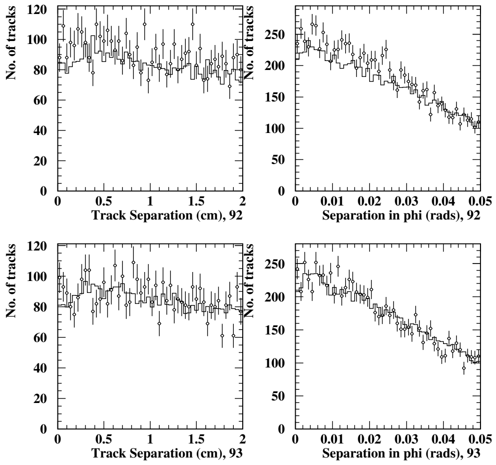

Figure 6.1: For each cone the two tracks with the closest minimum separation (straight line and phi) were calculated. These are plotted for years 92 and 93 and compared with the Monte Carlo for the barrel region.

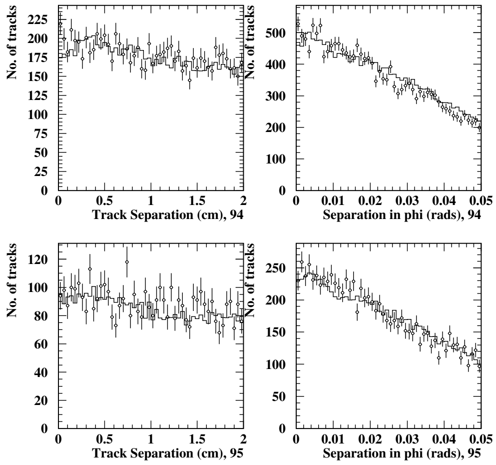

Figure 6.2: Closest minimum separation (straight line and phi) plotted for years 94 and 95 and compared with the Monte Carlo for the barrel region.

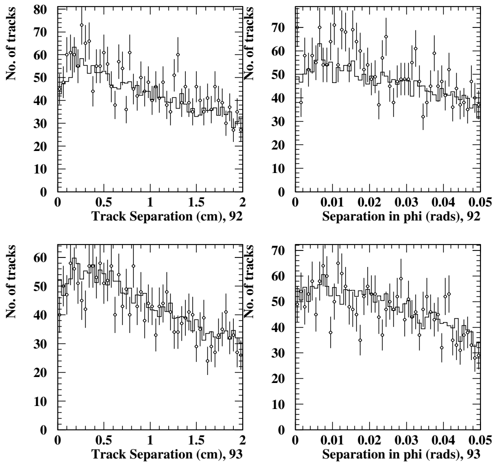

Figure 6.3: Closest minimum separation (straight line and phi) plotted for years 92 and 93 and compared with the Monte Carlo for the endcap region.

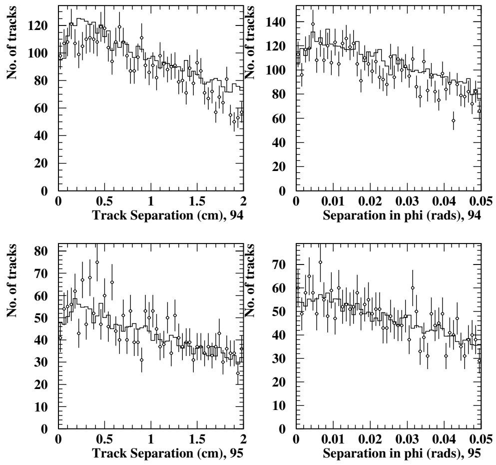

Figure 6.4: Closest minimum separation (straight line and phi) plotted for years 94 and 95 and compared with the Monte Carlo for the endcap region.

can be made on the probability of the track being a conversion. IDGCON uses an algorithm which calculates a normalised distance between two tracks. The default cuts were used to isolate conversion track candidates. Further details of IDGCON can be found in [72]. The efficiency and purity of each conversion finder are shown in table 6.3. The results show that the conversion finder used for the main analysis compares favourably with the other two conversion finders.

The two alternative conversion finders were used to calculate the branching ratios. The variation in the final branching ratio from using IDGCON and IDNCON are summarised in table 6.4 along with the variation if no conversion finding is used. It can be seen that although the results are mainly within the error derived from repeating the analysis with no conversion finding, they still differ by a large margin from the results obtained from the default conversion finder. The explanation for this can be placed upon the fact that both IDGCON and IDNCON are double arm conversion finders optimised for B analysis, where conversions usually have a momentum above 2GeV. In this analysis $\simeq$60% of conversions have momentum below 2 GeV. The default conversion finder also contains a single prong algorithm not available to the other two conversion finders (ie. checking even topologies for electrons from conversions, section 5.3). Therefore the systematic error will not be directly derived from these alternative conversion finders, they are seen instead as an overall check on the capabilities of finding conversions in this analysis.

To derive the systematic error for the default conversion finder two effects must be considered. Firstly one can check the effect of the efficiency on the result by varying the normalised dE/dx cut between 0.4 and 0.6. This contributes an error to the final result as summarised in tables 6.1 and 6.2. Secondly the number of π^0's could be modelled incorrectly in the Monte Carlo. Hence the normalised dE/dx is compared between data and Monte Carlo. It can be seen that the Monte Carlo does not model the data correctly in all cases (figures 6.5, 6.6, 6.7 and 6.8) and so corrections are applied to the reconstruction matrix as outlined in table 6.5 and new branching ratios are calculated. The correction factors vary from year to year due to changes in the π^0 modelling, and therefore conversion modelling, in the Monte Carlo. Assuming the differences in dE/dx distribution reflect purely the variation in the π^0 modelling the difference between these new results and the central result can be assigned as an error, summarised in tables 6.1 and 6.2.

Conversion Finder	Barrel Efficiency	Barrel Purity	Endcap Efficiency	Endcap Purity
Default	(89.5±0.1)%	(70.5±0.1)%	(87.5±0.1)%	(76.5±0.1)%
IDGCON	(90.5±0.1)%	(65.0±0.1)%	(88.3±0.1)%	(71.3±0.1)%
IDNCON	(95.2±0.1)%	(63.3±0.1)%	(94.0±0.1)%	(67.5±0.1)%

Table 6.3: Efficiencies and purities for the three conversion finders. The values presented are averages of the conversion finders acting on the four Monte Carlo data sets.

6.3 Background

To estimate the effect of the background on the result the multihadron and leptonic background were independently varied by ±10%. The leptonic background lies mainly in the 1-1 bin whereas the multihadronic background mainly lies outside the 1-1 bin. The effect on the central result is shown in the summary tables. It can be seen that varying the lepton background has a similar size effect as varying the multihadronic background. Both the barrel region and the endcap region show approximately the same variation in results.

6.4 Alternative method

In the method outlined in section 5.5 the χ^2 fit is performed over all the nine event multiplicity bins (see tables 5.2 and 5.3). Not all of these however are physically possible for a tau decay and some are solely due to detector and reconstruction

	B1(%)				B3(%)				B5(%)			
	92	93	94	95	92	93	94	95	92	93	94	95
Barrel												
No Conversion Finding	±0.25	±0.02	±0.07	±0.06	±0.22	±0.05	±0.07	±0.07	±0.031	±0.073	±0.009	±0.003
IDGCON	±0.20	±0.01	±0.03	±0.14	±0.13	±0.07	±0.05	±0.11	±0.063	±0.083	±0.025	±0.043
IDNCON	±0.16	±0.15	±0.05	±0.07	±0.20	±0.15	±0.05	±0.14	±0.038	±0.002	±0.008	±0.053
Endcap												
No Conversion Finding	±0.75	±0.60	±1.72	±0.26	±0.75	±0.43	±1.50	±0.24	±0.003	±0.172	±0.216	±0.022
IDGCON	±0.48	±0.25	±0.48	±0.12	±0.55	±0.17	±0.45	±0.03	±0.062	±0.089	±0.010	±0.088
IDNCON	±0.11	±0.28	±0.12	±0.12	±0.12	±0.20	±0.09	±0.10	±0.004	±0.078	±0.031	±0.022

Table 6.4: Variations in Branching Ratio results, with respect to the default conversion finder, due to changing the conversion finding algorithm. IDGCON and IDNNCON are standard OPAL conversion finding routines. Results obtained with no conversion finding are also included.

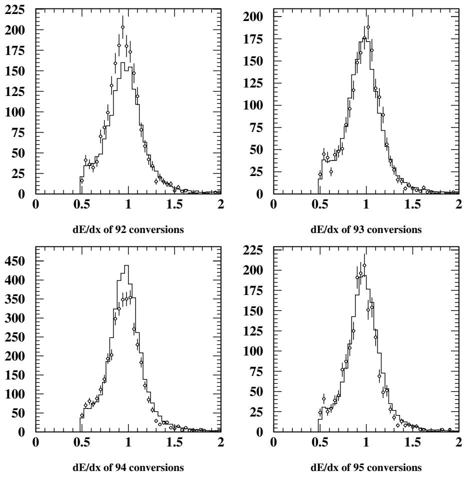

Figure 6.5: Distribution of normalised dE/dx for double prong conversions in the barrel region. Standard cut to identify a conversion is that the normalised dE/dx must be greater than 0.5.

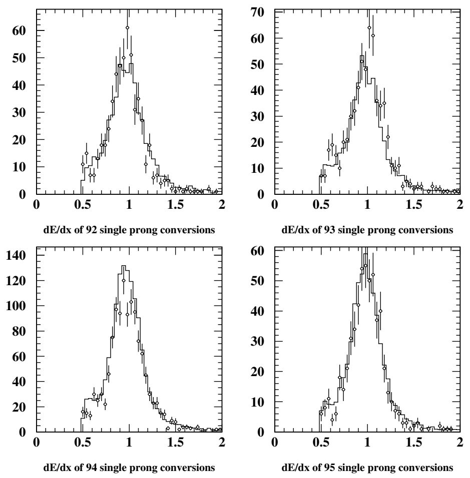

Figure 6.6: Distribution of normalised dE/dx for single prong conversions in the barrel region.

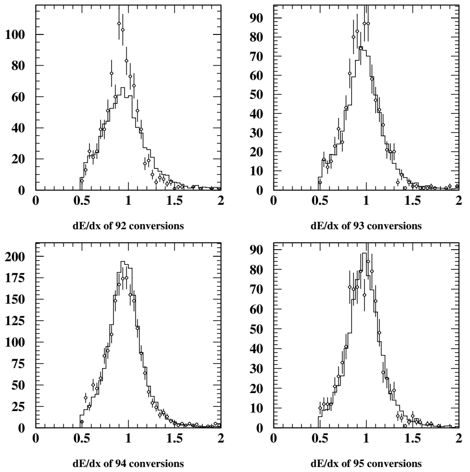

Figure 6.7: Distribution of normalised dE/dx for double prong conversions in the endcap region.

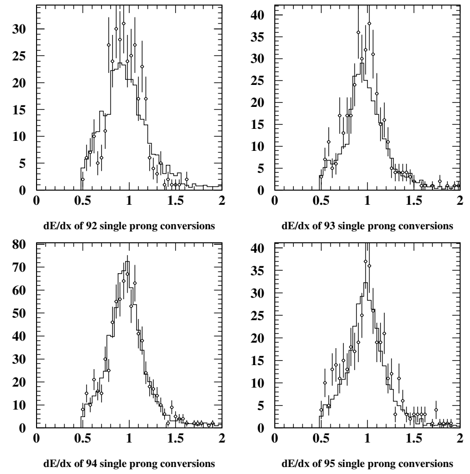

Figure 6.8: Distribution of normalised dE/dx for single prong conversions in the endcap region.

	92	93	94	95
Barrel				
Double Prong	+25%	0%	-18%	0%
Single Prong	+17%	-10%	+22%	0%
Endcap				
Double Prong	+35%	+17%	-13%	0%
Single Prong	0%	+27%	0 %	0%

Table 6.5: Correction to reconstruction matrix elements due to incorrect π^0 modelling in Monte Carlo. The corrections are estimated from the dE/dx distributions shown in figure 6.5. Double prong corrections apply to the matrix elements $\epsilon_{11\rightarrow 13}$, $\epsilon_{13\rightarrow 33}$ and $\epsilon_{13\rightarrow 15}$ while single prong corrections are applied to the matrix elements $\epsilon_{11\rightarrow 12}$, $\epsilon_{13\rightarrow 14}$ and $\epsilon_{13\rightarrow 23}$.

effects in particular the bins 1-2, 1-4, 2-2, 2-3, 2-4 and all bins with 0 tracks. This *cone* based method uses the studies made on the Monte Carlo (tables 5.5 and 5.6) to make the following approximation about the observed events. All cones with 0 tracks after conversion finding are placed in the 1 prong bin and the cones with 2 or 4 tracks are placed in the 3 prong bin as these are the topologies that the unphysical prongs are most likely to have originated from before the detector effects. After this process only the physical bins 1-1, 1-3, 1-5 and 3-3 are left. The reconstruction of these events are further summed into just three bins 1 prong, 3 prong and 5 prong. A migration matrix is calculated from the Monte Carlo sample, similar to that used in the main method but this time it is only a 3 by 3 matrix. It is defined as follows:

$$(\mathrm{M})(\tau_g)=(\tau_f)$$

where (τ_g) and (τ_f) are column vectors containing the number of 1, 3 and 5 prong tau decays. (g-generated, f-found). M is the matrix derived from the Monte Carlo, M_{11} represents the probability of a 1 prong decay remaining a 1 prong decay, M_{12} is the probability of a 3 prong decay becoming a 1 prong decay, M_{13} is the probability of a 5 prong decay becoming a 1 prong decay, M_{21} is the probability of a 1 prong decay becoming a 3 prong decay etc.

The results of this simplified method are presented in table 6.6, and are very consistent with the results obtained in the main analysis.

6.5 Variations in Monte Carlo

As this analysis relies heavily on the Monte Carlo the effect of calculating the branching ratios with different Monte Carlo samples was also examined. These are shown in table 6.7 for the barrel region and table 6.8 for the endcap. It can be seen that the results are in agreement with each other within errors. They also agree with the "default" results where the 92 Monte Carlo was used with the 92 data, the 93 Monte Carlo with the 93 data and so on (table 5.7).

The Monte Carlo has changed from year to year due to several effects. Firstly minor hardware changes must be introduced, for example the upgrade in the silicon

Data	Monte Carlo	Barrel Region			Endcap Region		
		$B_1(\%)$	$B_3(\%)$	$B_5(\%)$	$B_1(\%)$	$B_3(\%)$	$B_5(\%)$
1992	1992	84.63±0.24	15.27±0.23	0.106±0.055	84.14±0.42	15.28±0.41	0.277±0.104
1993	1993	84.78±0.25	15.00±0.24	0.220±0.053	84.78±0.42	14.88±0.41	0.344±0.111
1994	1994	84.63±0.18	15.22±0.17	0.150±0.040	84.77±0.30	15.03±0.29	0.208±0.083
1995	1995	84.51±0.25	15.36±0.24	0.125±0.059	85.08±0.42	14.79±0.41	0.128±0.077

Table 6.6: Branching ratios for the 1992, 1993, 1994 and 1995 data and Monte Carlos using the alternative analysis.

microvertex detector. Secondly there were minor improvements in the simulation of the detector which were incorporated into GOPAL and finally the most recent measurements of the tau branching ratios must be included. The most major specifc change to the Monte Carlo was a change in the resolution of tracks and hence a change in the double track resolution. This change happened between the 93 and 94 Monte Carlos.

6.6 Summary

The errors assigned to the effects discussed in the previous sections are summarised in table 6.1 for the barrel and table 6.2 for the endcap.

It is seen that the systematic errors in the barrel region are dominated by the anode plane effect. This error could be improved if the Monte Carlo correctly modelled the number of two prong events in the data sample, then the anode plane regions could be excluded completely without biasing the results. In the endcap region the systematic error for split tracks and track separation is of the same level of the anode plane effect. This is because of the uncertainty in track reconstruction increasing as $|cos\theta|$ increases, due to a decrease in the maximum number of hits available per track in CJ.

The results for each year have systematic errors of the same order. The only significant deviation is the B5 error for the 1995 sample (in both the barrel and endcap regions) which is less than half that of the other years, the reason for which is a smaller error from the anode plane effect.

A combined error from all years was calculated for each effect. To do this a statistically weighted average of the four numbers was taken, leaving an error for conversion finding on B1, an error for conversion finding on B3 etc. for both barrel and endcap.

Finally the combined errors for each effect were added in quadrature, resulting in a total systematic error for B1, B3 and B5. These are the errors quoted in the final result 7.1. It should be noted that the weighted average of the actual results (quoted in chapter 7 as a combined average) does not use these systematic errors in the weighting, only the statistical errors.

Data	Monte Carlo	$B_1(\%)$	$B_3(\%)$	$B_5(\%)$	χ^2/dof
1992	1993	84.61±0.21	15.27±0.21	0.122±0.048	5/6
1992	1994	84.72±0.21	15.16±0.20	0.115±0.049	5/6
1992	1995	84.76±0.21	15.12±0.20	0.117±0.051	4/6
1993	1992	84.66±0.22	15.12±0.21	0.218±0.059	8/6
1993	1994	84.82±0.22	15.00±0.21	0.188±0.057	8/6
1993	1995	84.86±0.22	14.96±0.21	0.185±0.058	7/6
1994	1992	84.41±0.15	15.40±0.15	0.185±0.041	8/6
1994	1993	84.46±0.15	15.38±0.15	0.163±0.038	9/6
1994	1995	84.60±0.15	15.24±0.15	0.164±0.044	3/6
1995	1992	84.36±0.21	15.46±0.21	0.179±0.053	8/6
1995	1993	84.40±0.21	15.44±0.21	0.154±0.049	9/6
1995	1994	84.52±0.21	15.34±0.21	0.149±0.051	7/6

Table 6.7: Systematic study using different Monte Carlo samples for the 1992, 1993, 1994 and 1995 data and Monte Carlos in the barrel region.

Data	Monte Carlo	B_1(%)	B_3(%)	B_5(%)	χ^2/dof
1992	1993	84.74±0.36	14.91±0.35	0.344±0.105	14/6
1992	1994	84.66±0.37	15.02±0.36	0.316±0.116	7/6
1992	1995	84.49±0.37	15.21±0.36	0.306±0.0.094	7/6
1993	1992	84.55±0.38	15.05±0.37	0.401±116	5/6
1993	1994	84.78±0.38	14.81±0.37	0.407±0.126	7/6
1993	1995	84.60±0.38	15.03±0.37	0.376±0.102	5/6
1994	1992	84.35±0.27	15.38±0.26	0.267±0.079	5/6
1994	1993	84.62±0.27	15.09±0.26	0.290±0.078	11/6
1994	1995	84.40±0.27	15.34±0.26	0.259±0.070	8/6
1995	1992	84.98±0.38	14.90±0.37	0.121±0.093	14/6
1995	1993	85.16±0.37	14.70±0.36	0.145±0.092	10/6
1995	1994	85.22±0.38	14.67±0.37	0.107±0.101	16/6

Table 6.8: Systematic study using different Monte Carlo samples for the 1992, 1993, 1994 and 1995 data and Monte Carlos in the endcap region.

Chapter 7

Final Results and Discussion

7.1 Results

Using a selection outlined in chapter 4 a sample of tau pairs was extracted from the 1992, 1993, 1994 and 1995 data. The total number of tau pairs found was 99310 in the barrel region and 38659 in the endcap region. Also used were the Monte Carlo samples R1508, R1513, R1520 and R1535, providing a total of 854485 simulated tau pairs in the barrel region and 330992 tau pairs in the endcap region. Both the data and the Monte Carlo were then subjected to conversion finding using the conversion finder outlined in section 5.3. After removal of conversions and correction for track reconstruction effects the topological branching ratios were found using a minimum χ^2 fit. The results obtained are shown in table 7.1. Where the first error is statistical and second is systematic.

The largest systematic errors in the barrel region are due to the anode region effect in 1992 and 1993 data but due to the track merging effect in the 1994 and 1995 data. In the endcap region the largest systematic error is also due to the anode plane effect but the split tracks and track separation errors are also significant. These systematic errors could be improved if the Monte Carlo modelled the number of two prong events correctly, then the anode plane region could be excluded without biasing the analysis. The analysis in the endcap region is limited by the number of hits in the tracking chamber reducing as $|cos\theta|$ increases, thus reducing the accuracy in track reconstruction.

The results from the barrel region and the endcap region agree well with each other within errors, with the endcap region having both larger statistical errors due to lower statistics, and larger systematic errors.

It can be seen from figures 7.1, 7.2 and 7.3, that these results agree with the previous published OPAL topological branching ratios paper which only used data from 1990 and 1991. They also agree within errors with the published OPAL 3 [73] prong and OPAL 5 [74] prong analysis which used data from 1991 up to 1994. The TAU94 exclusive and inclusive sums shown in these figures were obtained from the "Third Workshop on Tau Lepton Physics" [75] and consist of the weighted sums of all the exclusive modes and a weighted average of the inclusive measurements. These number are used in preference to the TAU96 [59] numbers due to a recent clarification by the Particle Data Group (PDG) in the treatment of K_s^0 decays. The PDG define 3 prong decays to include pions from $K_s^0 \to \pi^+\pi^-$. The analysis in this thesis treats these as one prong decays. Therefore careful consideration must be made as to which numbers this analysis can be directly compared to. The TAU96 results specifically took account of the treatment of K_s^0 decays as 3 prongs and hence cannot be used as a direct comparison. The world fits included in these figures treat the K_s^0 decays in the same manner that this thesis does.

Although it is not possible to predict the topological ratios from theory many of the exclusive branching ratios have been calculated [76]. These results for one prong branching ratios can be seen alongside the OPAL one prong exclusive branching ratios in table 7.2. To make a comparison to the branching ratios measured in this thesis the remaining branching ratios not calculated by theory must be added to the total. The world fits from the Particle Data Group [54] were used to do this. There have been no precise calculations of the three prong and five prong branching ratios however the results from this analysis can be compared with separate OPAL analyses measuring these ratios (see figures 7.1, 7.2 and 7.3). It can be seen that the results are all in good agreement with each other indicating internal consistency within the OPAL data and the lack of any new unexpected branching ratios.

		92	93	94	95	combined
Barrel	B1(%)	84.57±0.21±0.17	84.70±0.22±0.16	84.56±0.15±0.15	84.55±0.22±0.14	84.59±0.10±0.14
	B3(%)	15.29±0.20±0.11	15.09±0.21±0.13	15.28±0.15±0.14	15.29±0.21±0.13	15.25±0.09±0.12
	B5(%)	0.139±0.053±0.060	0.206±0.055±0.064	0.157±0.046±0.056	0.158±0.052±0.018	0.164±0.026±0.047
Endcap	B1(%)	84.42±0.37±0.25	84.83±0.37±0.18	84.59±0.27±0.38	85.00±0.37±0.21	84.69±0.17±0.27
	B3(%)	15.25±0.36±0.27	14.75±0.36±0.16	15.15±0.26±0.35	14.86±0.37±0.20	15.03±0.16±0.25
	B5(%)	0.325±0.107±0.047	0.424±0.114±0.054	0.260±0.086±0.052	0.134±0.082±0.023	0.259±0.047±0.042

Table 7.1: Summary of final results including a combined weighted average.

7.2 Comparison with Other Experiments

Four other experiments have recently measured the topological branching ratios as this analysis does, they are ALEPH, DELPHI, L3 and CELLO. Following is a discussion of the methods used by these experiments and a comparison of their results.

L3

The L3 detector [17] is based at the LEP collider and data was taken at the mass of the Z^0 peak. The tau selection [61] cuts based mainly on calorimetric quantities and arrive at a sample of 2540 tau pairs (this paper was published in 1991, so more recent data are not included). For the multiplicity measurement at least one well measured track was required per event with the track criteria being a good track fit, a minimum number of track hits and a distance of closest approach to the beam position. Also due to problems in simulating the double track resolution near the borders of the central tracking chamber the regions within 15 mrads of the anode and cathode planes are eliminated from the analysis. Using Monte Carlo the probabilities of a track of i charged particles being observed as j charged particles is calculated, much the same as in this thesis. Also calculated from the Monte Carlo is the efficiency of observing a one, three or five prong decay and the estimated background observed. All these quantities are used to calculate the number of tracks predicted and are then fitted to the observed multiplicity. The free parameters in the fit are B1 and B3, with B5 being calculated from the fact that the sum of the three ratios is constrained to be one. As it is known that B1 and B3 are highly correlated this would not appear to be the best method to obtain the results and may go some way to explaining why only a limit on B5 is obtained. Systematic uncertainties are obtained from the uncertainty in deriving the parameters in the fit from Monte Carlo, background uncertainties and the influence of excluding the sector border regions. The final results have a statistical error six times the size of the analysis in the barrel region from this thesis and the systematic errors are approximately twice as large. The one prong branching ratio is also approximately 1% higher than that measured in this analysis with the three prong branching ratio being correspondingly 1% lower.

CELLO

The CELLO detector was based at the PETRA e^+e^- collider with a centre of mass energy ranging from 35.0 GeV to 46.8 GeV, corresponding to an average centre of mass energy of 42.8 GeV. The selection procedure used by CELLO [64] did not include tau pairs where both tau leptons decay to either electrons or muons due to large background contamination and included cuts to reduce photon conversions, bhabha events by calorimeter energy, muon pairs by hits in the muon chamber, two photon events by acolinearity and multihadronic events by multiplicity. All events were subjected to a visual scan and background events were removed, with the remaining background estimated from Monte Carlo. The final sample consisted of 4116 events. The Monte Carlo was then used to calculate the expected multiplicity via a matrix similar to that in this thesis. Then to calculate the branching ratios the observed multiplicity was fitted to the predicted multiplicity by a likelihood function. Systematic errors were estimated by varying the selection cuts and also the matrix elements. The resulting systematic errors are approximately twice the value of those in this thesis with the statistical errors being approximately four times as large. The values of the branching ratios agree with this thesis within errors.

DELPHI

The DELPHI detector [16] is based at the LEP collider and data was taken at centre of mass energies of 89.2 GeV, 91.2 GeV and 93.2 GeV. For the measurement of the topological branching ratios [62] a sample of 63000 tau pair events was used. These events were selected by first rejecting cosmic rays, multihadronic events and two photon events, and then further rejecting Bhabha events and muon pair events. The total tau pair selection efficiency was 80% with a total background of 2%. Before the measurement photon conversions were rejected by their identification in the electromagnetic calorimeter. Decays of the type $K_s^0 \to \pi^+\pi^-$ were assigned as one prongs. First the one prong ratio was measured. To select a one prong decay further requirements were made; there must be one measured track with an energy greater than 3 GeV, and also there must be a signal in the vertex detector. This selection gave a sample of 92543 candidate one prong decays, with a selection efficiency of 98.8% and an estimated background of 3.3%. The corresponding one prong ratio was B1=(85.15±0.10±0.19)% where the first error is statistical and the second is systematic. Next the three prong ratio was measured. In this selection it was required that there were at least two signals in the vertex detector to suppress photon conversions. This selection gave 14865 candidate three prong decays, with a selection efficiency of 80% and an estimated background of 6%. The corresponding three prong measurement is B3=(14.95±0.11±0.17)%. Next the two measurements were combined with the world average five prong measurement, although from the paper it is unclear how this was done. The final one prong and three prong ratios are B1=(85.06±0.10±0.17)% and B3=(14.85±0.10±0.17)% where the first error is statistical and the second is systematic. These errors are of the same order as the measurement in this thesis but the results are approximately 1.5 sigma higher.

ALEPH

The ALEPH detector [15] is based at the LEP collider and the data was taken at centre of mass energies 89.4 GeV, 93.0 GeV and at the Z^0 peak. The collaboration select their tau events using a standard tau selection procedure. The total sample of tau pairs is not mentioned in the paper [63], however the data set of 1991-1993 for this thesis correspond to approximately 50000 tau pairs and the ALEPH data set should be similar. However their method is slightly different to the analysis in this thesis. Each hemisphere is first classed by its multiplicity, 1 to 7, with two extra categories 2+ and 4+ for cones which have two overlapping tracks. Those hemispheres with a principal class of 0 to 3 are then divided into 9 sub classes. These nine sub classes are: high multiplicity vertex radial distance less than 25cm, high multiplicity vertex radial distance greater than 25cm, single prong conversion, double prong conversion, vertex with multiplicity 2 (no conversion), pure good tracks only, one bad track, two bad tracks and three bad tracks. Thus each hemisphere is assigned to one of 50 classes. The whole event therefore has a total of 1225 classes which are further divided into events with zero total charge or with a charge imbalance. The probability to reconstruct an event in a certain class depends on the true topology of the event and are summarised in a matrix derived from the Monte Carlo. A likelihood fit is then calculated to extract the branching ratios in a similar way to the previously mentioned analyses. The advantage of this extended event classification is the ability to examine systematic effects in greater detail. The result is systematic errors for B1 and B3 of the same order as this thesis but an error for B5 which is approximately 6 times lower. The dominant systematical error in the analysis derives from the uncertainty in the selection procedure. Statistical errors are of the same order as this thesis and the B1 result is approximately 0.8% higher with B3 being correspondingly 0.8% lower than the results presented in this thesis. The value of B5 is also approximately 0.06% lower than the results in this thesis. These results are consistent with the previous ALEPH results. However the ALEPH results have always had a B1 approximately 1% higher than OPAL results, including comparison with the published OPAL results, but no reason has been found for this discrepancy.

CLEO

At this point some mention should also be made of the CLEO [78] experiment based at the Cornell Electron Storage Ring. Although they have not made a fit to B1, B3 and B5 as this thesis does, their huge data sample of over a million tau pair decays has made it possible to measure many branching ratios very accurately. The centre of mass energy for the experiment is 10.6 GeV. The measurements most relevant to this thesis are, B3=$(14.22\pm0.10\pm0.37)$% and B5=$(0.097\pm0.005\pm0.011)$% [79].

Also included on figures 7.1, 7.2 and 7.3, are the Branching Ratio fits from the Particle Data Group. This is obtained from a global fit to all the exclusive branching ratios, details of which can be found in [54], and is therefore in effect the sum of all the presently measured exclusive branching ratios. The World Fits are at present dominated by ALEPH results due to an analysis which carried out a global fit to all hadronic decay modes of the tau [80]. It is unsurprising therefore to notice that the PDG96 fits are well matched to the ALEPH topological branching ratio re-

Decay Mode	OPAL	Theory
$e^- \bar{\nu}_e \nu_\tau$	17.78±0.10±0.09	17.9±1.0±1.6
$\mu^- \bar{\nu}_\mu \nu_\tau$	17.45±0.12±0.04	17.4±1.0±1.6
$h^- \nu_\tau$	12.1±0.7±0.5	11.67±0.06
$h^- \pi^0 \nu_\tau$	26.25±0.36±0.52	25.1±0.6
$h^- \geq 2\pi^0 \nu_\tau$	9.89±0.34±0.55	
$K^- 2\pi^0 \nu_\tau$		0.12±0.04
$\pi^- 3\pi^0 \nu_\tau$		1.08±0.05
$\pi^- K^0 \nu_\tau$	1.04±0.13±0.09	
$K^- K^0 \nu_\tau$	0.10±0.07±0.02	0.12±0.03
$\pi^- \pi^0 K^0 \nu_\tau$	0.48±0.12±0.07	
$K^- \pi^0 K^0 \nu_\tau$	0.18±0.09±0.03	
$h^- K^0 K^0 \nu_\tau$		0.044±0.032
$\pi^- \geq 0\pi^0 \geq 0K^0 \nu_\tau$	1.43±0.08±0.08	
Sum of modes not theoretically calculated (from PDG)		11.76±0.28
Total	86.22±1.29	85.19±2.00
Barrel analysis 84.59±0.10±0.14		
Endcap analysis 84.69±0.17±0.27		

Table 7.2: A comparison of theoretical predictions [76] of one prong exclusive branching ratios, OPAL one prong exclusive branching ratio measurements and the one prong topological branching ratio measured by this analysis. Where h can be either a pion or a kaon.

sults. However the World *Averages* for the branching ratios are, B1=(84.59$\pm$0.33)%, B3=(14.63$\pm$0.35)%, B5=(0.102$\pm$0.011)%. This brings the PDG values in line with the results obtained by this thesis.

7.3 Summary

The topological branching ratios measured in this thesis agree well with the previous OPAL analysis and also separate three and five prong OPAL analyses. The results are also consistent with the world averages indicating that there are no significant problems in the tau sector.

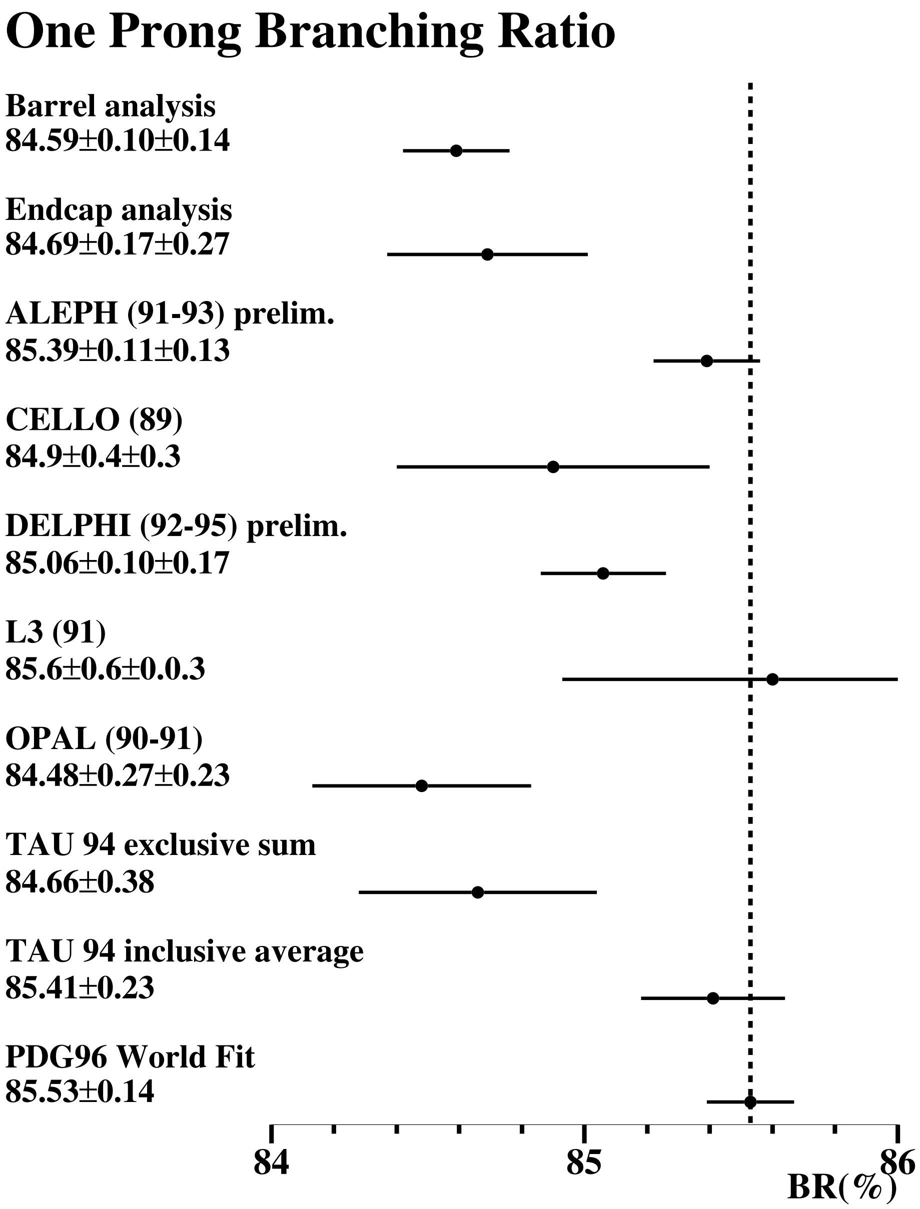

Figure 7.1: Summary of one prong results.

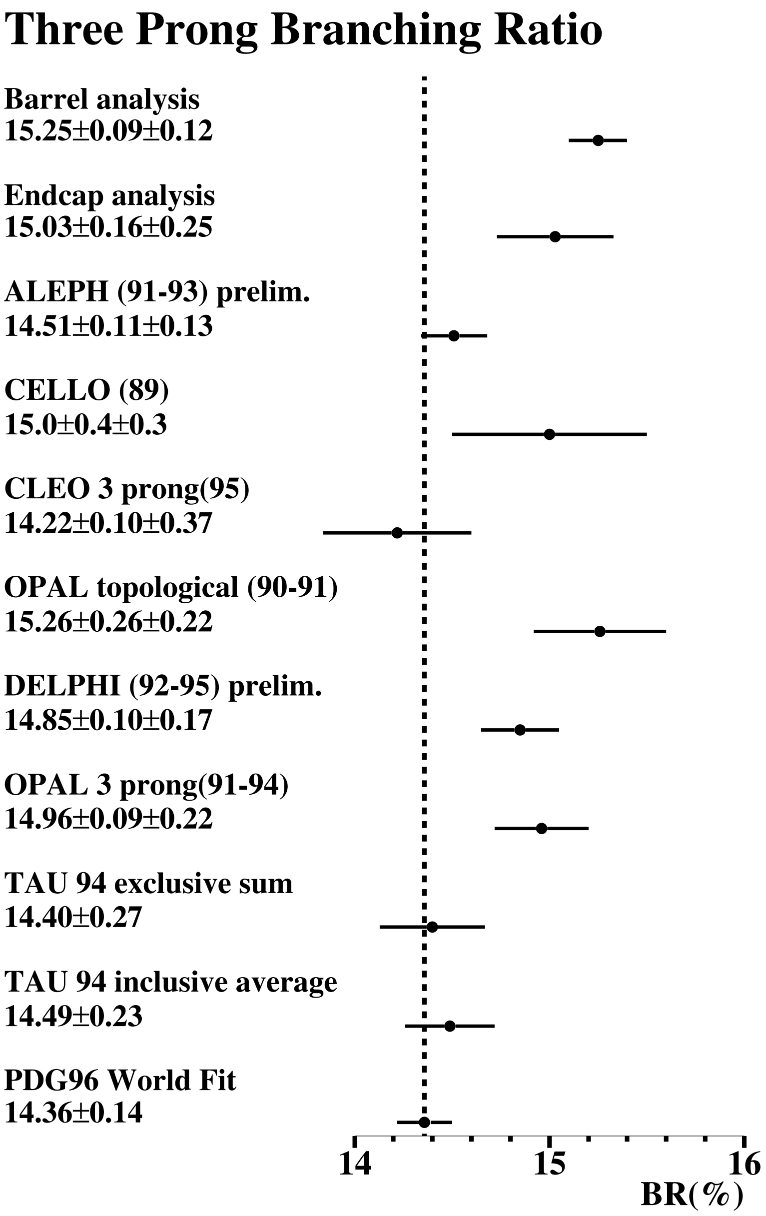

Figure 7.2: Summary of three prong results.

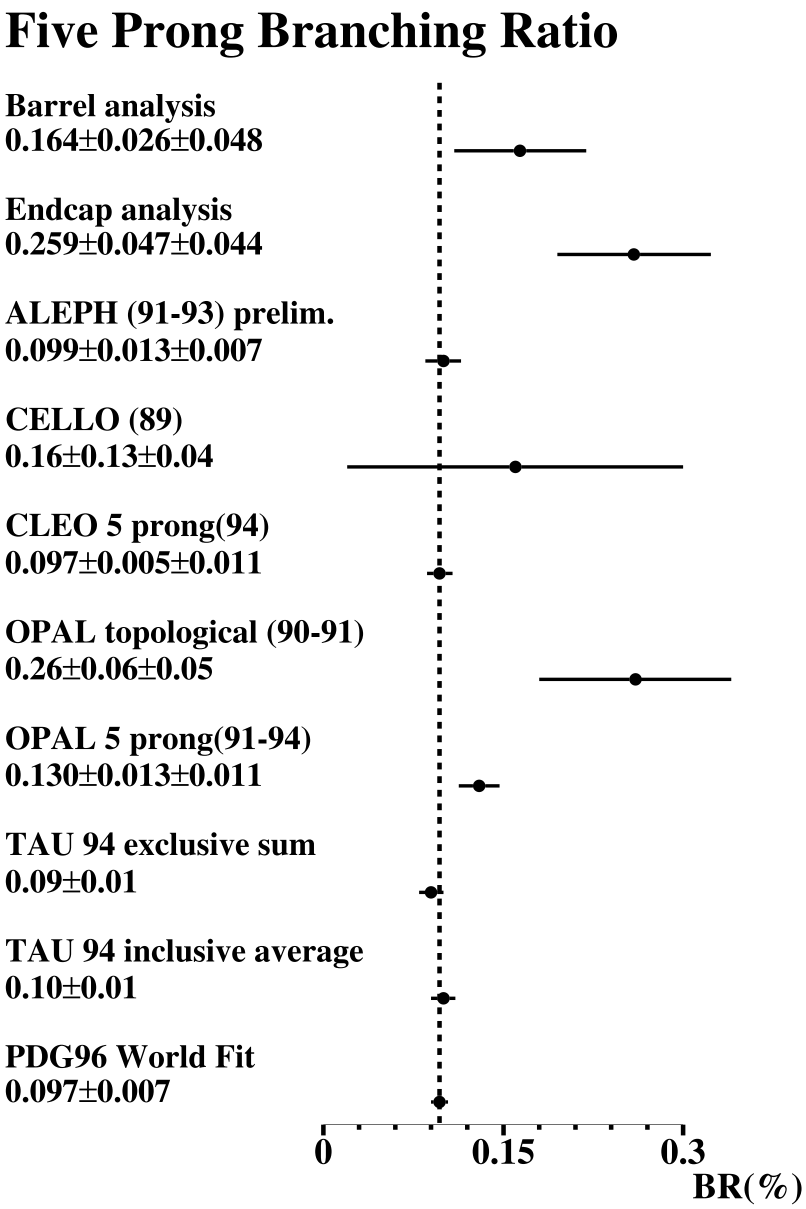

Figure 7.3: Summary of five prong results.

Appendix A

Control sample details

Following are tables containing the figures used to correct the background in the tau sample for the endcap region. The process is outlined in detail in section 4.5 but a brief summary follows.

Control samples were obtained of bhabha events, muon pair events, multi-hadronic events and two photon events. Using these control samples the region adjacent to the tau selection cuts were examined and compared with the relevant Monte Carlo. These regions should simulate any background which will enter the tau sample. Correction factors are then calculated from the figures and this correction is applied to the background outlined in chapter 5.

Event sample	Number of events
	1992
MC $e^+e^- \to \mu^+\mu^-$	41 ± 2.9
MC $e^+e^- \to \tau^+\tau^-$	61 ± 2.8
All Data	112 ± 10.6
DATA $e^+e^- \to \mu^+\mu^-$	51 ± 11.0
Ratio $\frac{DATA(e^+e^-\to\mu^+\mu^-)}{MC(e^+e^-\to\mu^+\mu^-)}$	1.24± 0.28
Event sample	Number of events
	1993
MC $e^+e^- \to \mu^+\mu^-$	35 ± 2.6
MC $e^+e^- \to \tau^+\tau^-$	58 ± 2.8
All Data	116 ± 10.8
DATA $e^+e^- \to \mu^+\mu^-$	58 ± 11.2
Ratio $\frac{DATA(e^+e^-\to\mu^+\mu^-)}{MC(e^+e^-\to\mu^+\mu^-)}$	1.65± 0.34
Event sample	Number of events
	1994
MC $e^+e^- \to \mu^+\mu^-$	82 ± 3.5
MC $e^+e^- \to \tau^+\tau^-$	128 ± 4.3
All Data	249 ± 15.8
DATA $e^+e^- \to \mu^+\mu^-$	121 ± 16.4
Ratio $\frac{DATA(e^+e^-\to\mu^+\mu^-)}{MC(e^+e^-\to\mu^+\mu^-)}$	1.48± 0.14
Event sample	Number of events
	1995
MC $e^+e^- \to \mu^+\mu^-$	38 ± 2.0
MC $e^+e^- \to \tau^+\tau^-$	48 ± 1.6
All Data	107 ± 10.3
DATA $e^+e^- \to \mu^+\mu^-$	59 ± 10.5
Ratio $\frac{DATA(e^+e^-\to\mu^+\mu^-)}{MC(e^+e^-\to\mu^+\mu^-)}$	1.55± 0.29

Table A.1: Shown for each year is the muon pair control sample in data and in Monte Carlo.

Event sample	Number of events
	1992
MC $e^+e^- \to e^+e^-$	943 $\pm$ 31.5
MC $\mathrm{e}^+\mathrm{e}^- \to \tau^+\tau^-$	168 $\pm$ 4.7
All Data	1305 $\pm$ 36.1
DATA $e^+e^- \to e^+e^-$	1137 $\pm$ 36.4
Ratio $\frac{DATA(e^+e^-\to e^+e^-)}{MC(e^+e^-\to e^+e^-)}$	1.21 $\pm$ 0.06
Event sample	Number of events
	1993
MC $e^+e^- \to e^+e^-$	2015 $\pm$ 28.5
MC $\mathrm{e}^+\mathrm{e}^- \to \tau^+\tau^-$	159 $\pm$ 4.6
All Data	2199 $\pm$ 46.9
DATA $e^+e^- \to e^+e^-$	2040 $\pm$ 47.1
Ratio $\frac{DATA(e^+e^-\to e^+e^-)}{MC(e^+e^-\to e^+e^-)}$	1.01 $\pm$ 0.03
Event sample	Number of events
	1994
MC $e^+e^- \to e^+e^-$	2861 $\pm$ 40.7
MC $\mathrm{e}^+\mathrm{e}^- \to \tau^+\tau^-$	535 $\pm$ 8.8
All Data	2619 $\pm$ 51.2
DATA $e^+e^- \to e^+e^-$	2084 $\pm$ 52.0
Ratio $\frac{DATA(e^+e^-\to e^+e^-)}{MC(e^+e^-\to e^+e^-)}$	0.73 $\pm$ 0.02
Event sample	Number of events
	1995
MC $e^+e^- \to e^+e^-$	1333 $\pm$ 26.9
MC $\mathrm{e}^+\mathrm{e}^- \to \tau^+\tau^-$	140 $\pm$ 3.8
All Data	1740 $\pm$ 41.7
DATA $e^+e^- \to e^+e^-$	1600 $\pm$ 41.9
Ratio $\frac{DATA(e^+e^-\to e^+e^-)}{MC(e^+e^-\to e^+e^-)}$	1.20 $\pm$ 0.04

Table A.2: Shown for each year is the bhabha control sample in data and in Monte Carlo.

Event sample	Number of events
	1992
MC $e^+e^- \to q\bar{q}$	25 ± 4.4
MC $e^+e^- \to \tau^+\tau^-$	56 ± 2.7
All Data	80 ± 8.9
DATA $e^+e^- \to q\bar{q}$	24 ± 9.3
Ratio $\frac{DATA(e^+e^- \to q\bar{q})}{MC(e^+e^- \to q\bar{q})}$	0.96±0.41
Event sample	Number of events
	1993
MC $e^+e^- \to q\bar{q}$	26 ± 4.6
MC $e^+e^- \to \tau^+\tau^-$	46 ± 2.3
All Data	73 ± 8.5
DATA $e^+e^- \to q\bar{q}$	27 ± 9.7
Ratio $\frac{DATA(e^+e^- \to q\bar{q})}{MC(e^+e^- \to q\bar{q})}$	1.03±0.41
Event sample	Number of events
	1994
MC $e^+e^- \to q\bar{q}$	116 ± 14.2
MC $e^+e^- \to \tau^+\tau^-$	124 ± 4.1
All Data	159 ± 12.6
DATA $e^+e^- \to q\bar{q}$	35 ± 13.3
Ratio $\frac{DATA(e^+e^- \to q\bar{q})}{MC(e^+e^- \to q\bar{q})}$	1.07±0.43
Event sample	Number of events
	1995
MC $e^+e^- \to q\bar{q}$	45 ± 4.2
MC $e^+e^- \to \tau^+\tau^-$	33 ± 1.8
All Data	80 ± 8.9
DATA $e^+e^- \to q\bar{q}$	47 ± 9.1
Ratio $\frac{DATA(e^+e^- \to q\bar{q})}{MC(e^+e^- \to q\bar{q})}$	1.04 ± 0.12

Table A.3: Shown for each year is the multihadron control sample in data and in Monte Carlo.

Event sample	Number of events
	1992
MC $e^+e^- \to e^+e^-\mu^+\mu^-$	336 $\pm$ 13.1
MC $e^+e^- \to \tau^+\tau^-$	0 $\pm$ 0
All Data	282 $\pm$ 16.8
DATA $e^+e^- \to e^+e^-\mu^+\mu^-$	282 $\pm$ 16.8
Ratio $\frac{DATA(e^+e^-\to e^+e^-\mu^+\mu^-)}{MC(e^+e^-\to e^+e^-\mu^+\mu^-)}$	0.84 $\pm$ 0.06
Event sample	Number of events
	1993
MC $e^+e^- \to e^+e^-\mu^+\mu^-$	473 $\pm$ 6.9
MC $e^+e^- \to \tau^+\tau^-$	0 $\pm$ 0
All Data	406 $\pm$ 20.1
DATA $e^+e^- \to e^+e^-\mu^+\mu^-$	406 $\pm$ 20.1
Ratio $\frac{DATA(e^+e^-\to e^+e^-\mu^+\mu^-)}{MC(e^+e^-\to e^+e^-\mu^+\mu^-)}$	0.86 $\pm$ 0.05
Event sample	Number of events
	1994
MC $e^+e^- \to e^+e^-\mu^+\mu^-$	628 $\pm$ 8.8
MC $e^+e^- \to \tau^+\tau^-$	0 $\pm$
All Data	588 $\pm$ 24.2
DATA $e^+e^- \to e^+e^-\mu^+\mu^-$	588 $\pm$ 24.2
Ratio $\frac{DATA(e^+e^-\to e^+e^-\mu^+\mu^-)}{MC(e^+e^-\to e^+e^-\mu^+\mu^-)}$	0.94$\pm$ 0.04
Event sample	Number of events
	1995
MC $e^+e^- \to e^+e^-\mu^+\mu^-$	536 $\pm$ 7.5
MC $e^+e^- \to \tau^+\tau^-$	0 $\pm$ 0
All Data	410 $\pm$ 20.2
DATA $e^+e^- \to e^+e^-\mu^+\mu^-$	410 $\pm$ 20.2
Ratio $\frac{DATA(e^+e^-\to e^+e^-\mu^+\mu^-)}{MC(e^+e^-\to e^+e^-\mu^+\mu^-)}$	0.76 $\pm$ 0.05

Table A.4: Shown for each year is the two photon muon pair control sample in data and in Monte Carlo.

Event sample	Number of events
	1992
MC $e^+e^- \to e^+e^-e^+e^-$	212 ± 11.3
MC $e^+e^- \to \tau^+\tau^-$	$0 \pm$
All Data	194 ± 13.9
DATA $e^+e^- \to e^+e^-e^+e^-$	194 ± 13.9
Ratio $\frac{DATA(e^+e^- \to e^+e^-e^+e^-)}{\mathrm{MC}(e^+e^- \to e^+e^-e^+e^-)}$	0.92 ± 0.08
Event sample	Number of events
	1993
MC $e^+e^- \to e^+e^-e^+e^-$	306 ± 5.9
MC $e^+e^- \to \tau^+\tau^-$	0 ± 0
All Data	239 ± 15.5
DATA $e^+e^- \to e^+e^-e^+e^-$	239 ± 15.5
Ratio $\frac{DATA(e^+e^- \to e^+e^-e^+e^-)}{\mathrm{MC}(e^+e^- \to e^+e^-e^+e^-)}$	0.78 ± 0.05
Event sample	Number of events
	1994
MC $e^+e^- \to e^+e^-e^+e^-$	467 ± 8.3
MC $e^+e^- \to \tau^+\tau^-$	0 ± 0
All Data	373 ± 19.3
DATA $e^+e^- \to e^+e^-e^+e^-$	373 ± 19.3
Ratio $\frac{DATA(e^+e^- \to e^+e^-e^+e^-)}{\mathrm{MC}(e^+e^- \to e^+e^-e^+e^-)}$	0.80 ± 0.04
Event sample	Number of events
	1995
MC $e^+e^- \to e^+e^-e^+e^-$	395 ± 7.0
MC $e^+e^- \to \tau^+\tau^-$	0 ± 0
All Data	266 ± 16.3
DATA $e^+e^- \to e^+e^-e^+e^-$	266 ± 16.3
Ratio $\frac{DATA(e^+e^- \to e^+e^-e^+e^-)}{\mathrm{MC}(e^+e^- \to e^+e^-e^+e^-)}$	0.67 ± 0.04

Table A.5: Shown for each year is the two photon ee control sample in data and in Monte Carlo.

Appendix B

Plots of number of hits in CJ

This appendix contains plots of the number of hits for each track in CJ, with the samples being divided into subsets depending on the number of tracks in the associated cone. These plots are discussed in detail in chapter 5 and are included here for completeness. The significant excess of data points of Monte Carlo points at a low number of CJ hits can be seen in the plots of 2 prong cones. These indicate the presence of split tracks which in turn are rejected from the samples by cuts outlined in chapter 5.

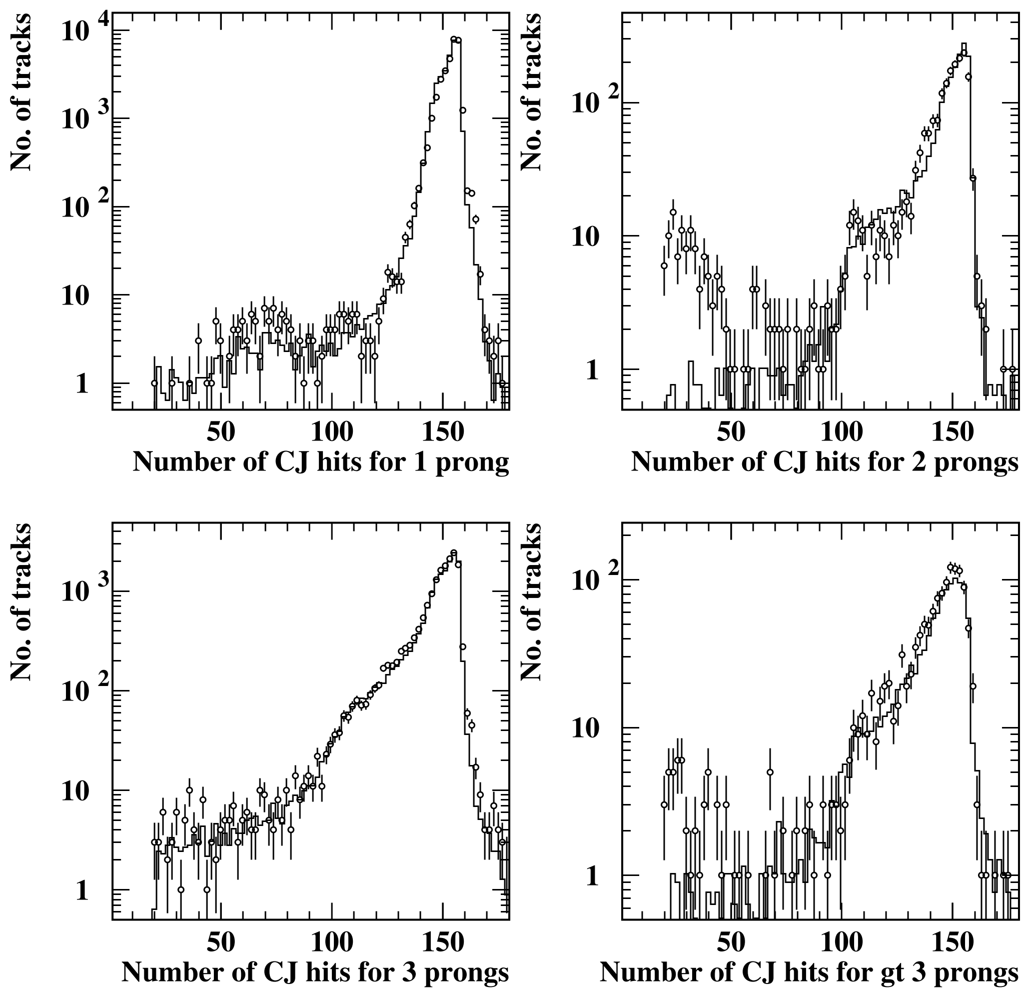

Figure B.1: Number of hits per track in CJ for 92 data and Monte Carlos for the barrel region.

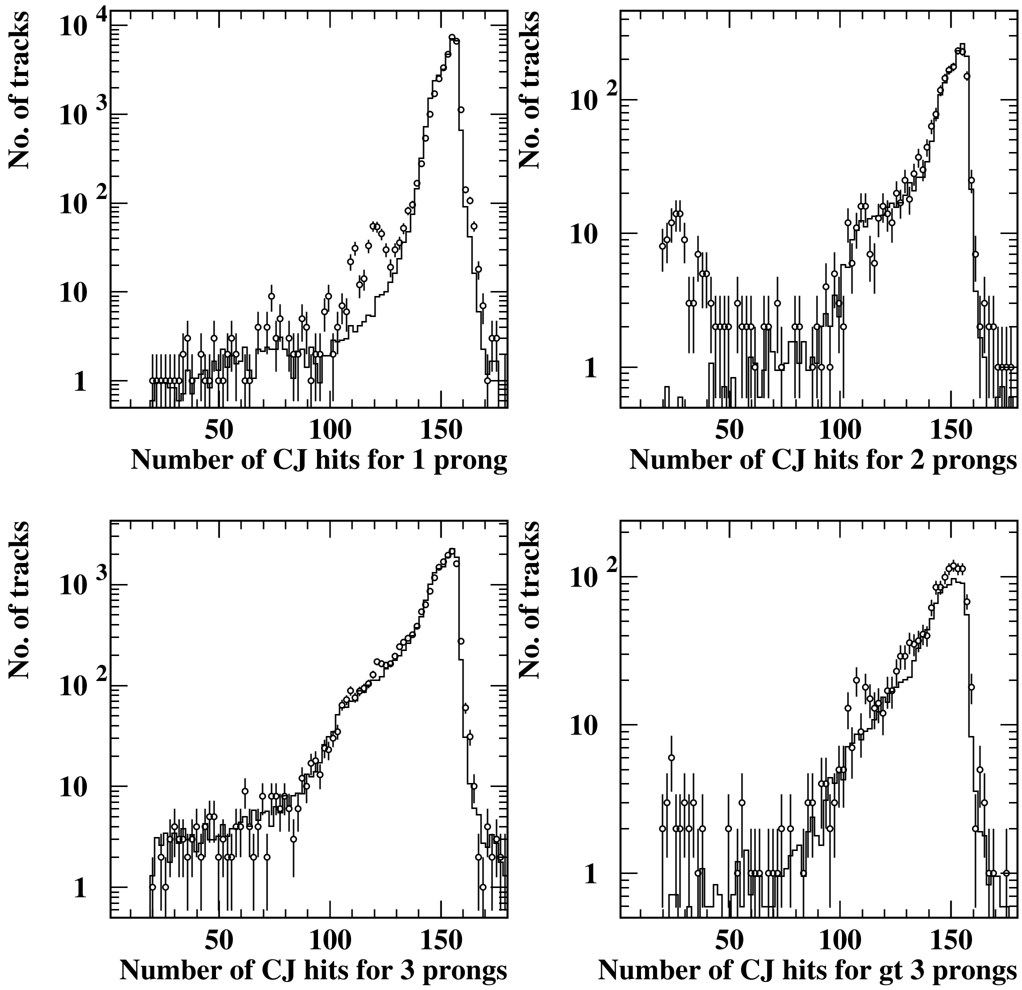

Figure B.2: Number of hits per track in CJ for 93 data and Monte Carlos for the barrel region.

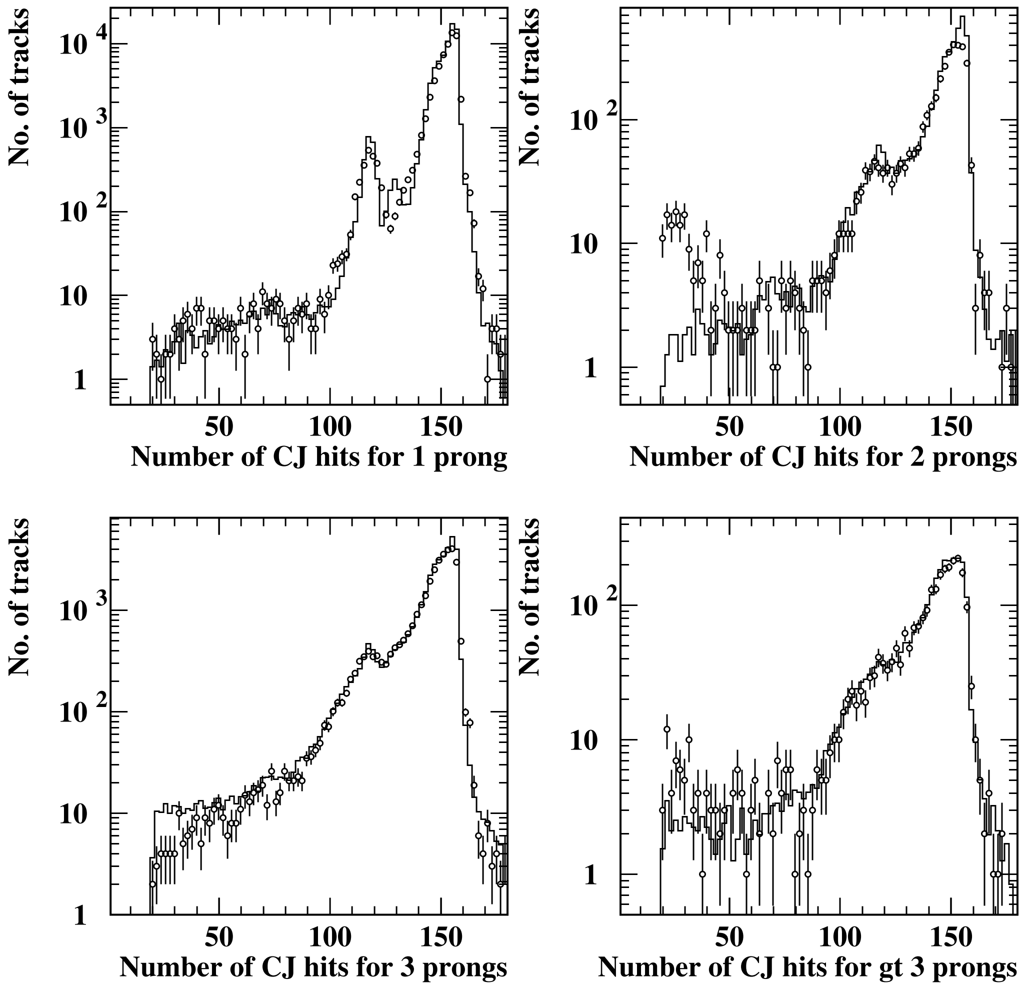

Figure B.3: Number of hits per track in CJ for 94 data and Monte Carlos for the barrel region.

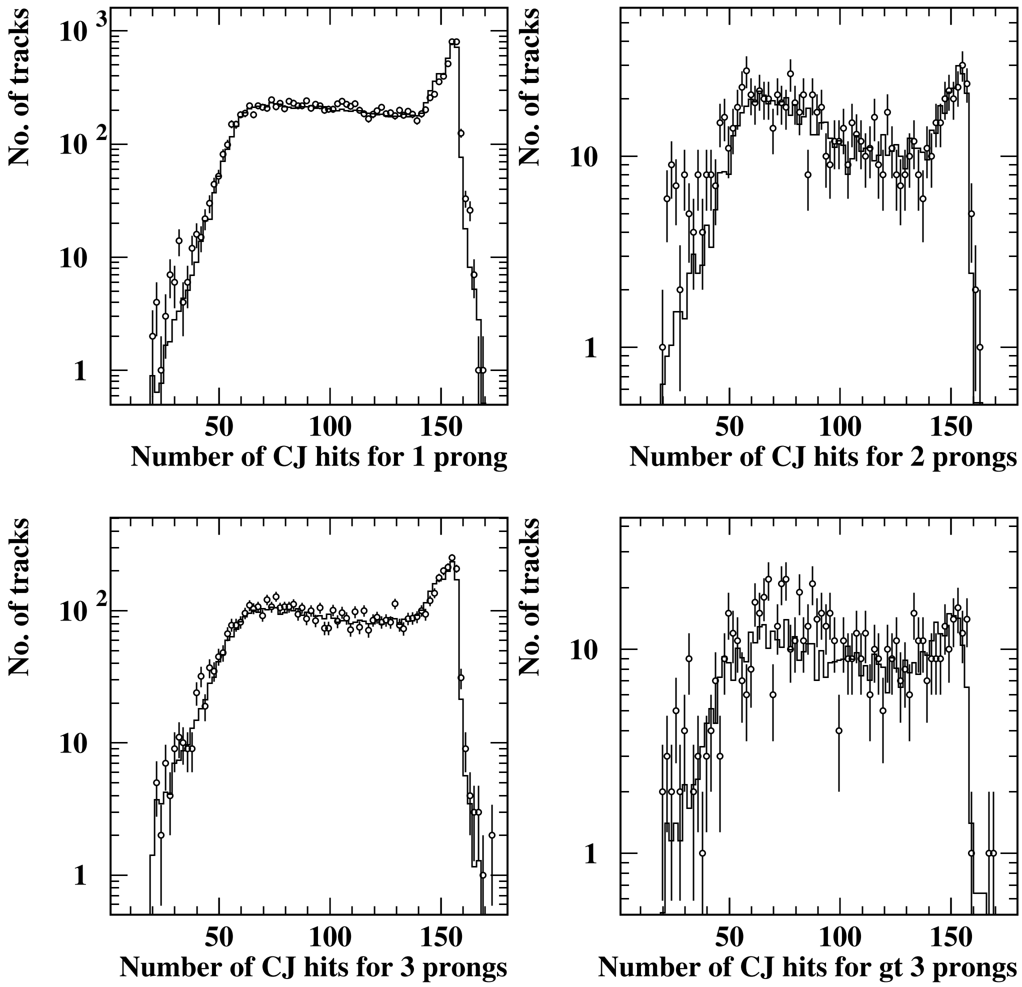

Figure B.4: Number of hits per track in CJ for 92 data and Monte Carlos for the endcap region.

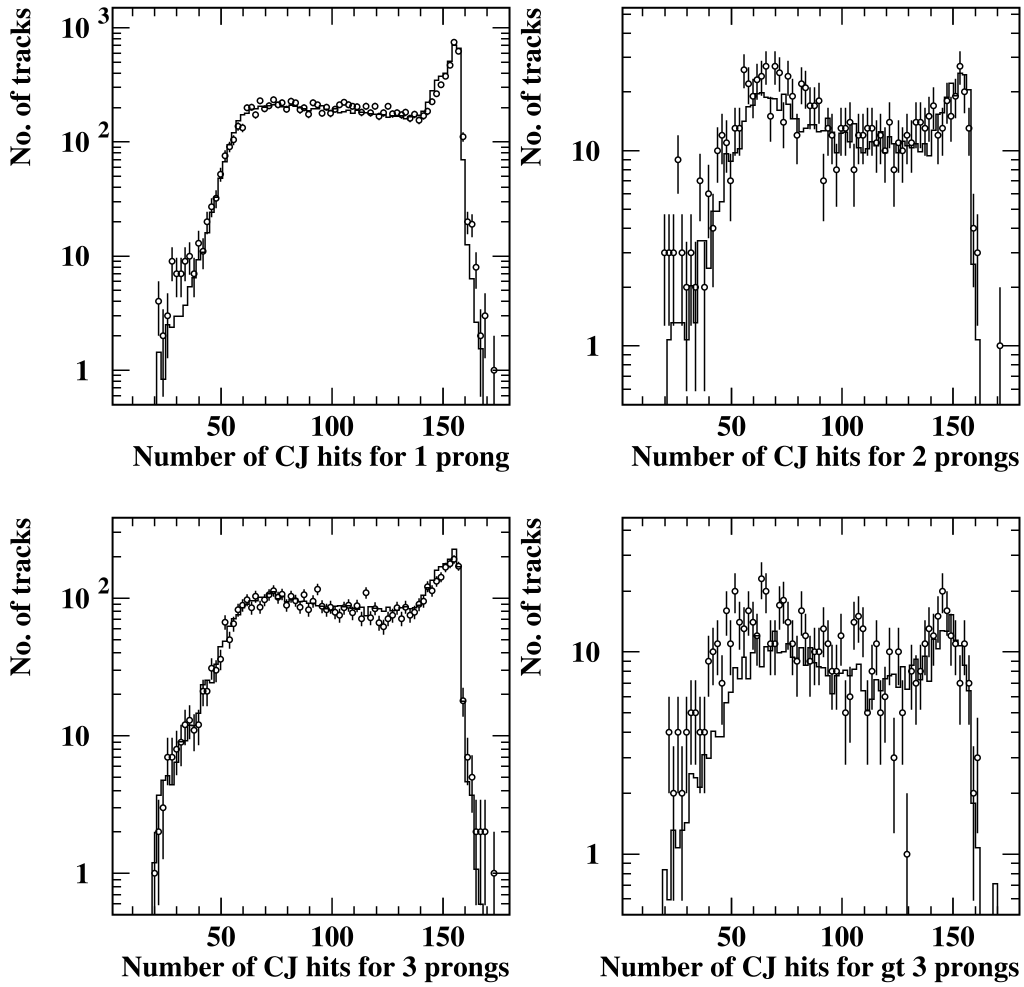

Figure B.5: Number of hits per track in CJ for 93 data and Monte Carlos for the endcap region.

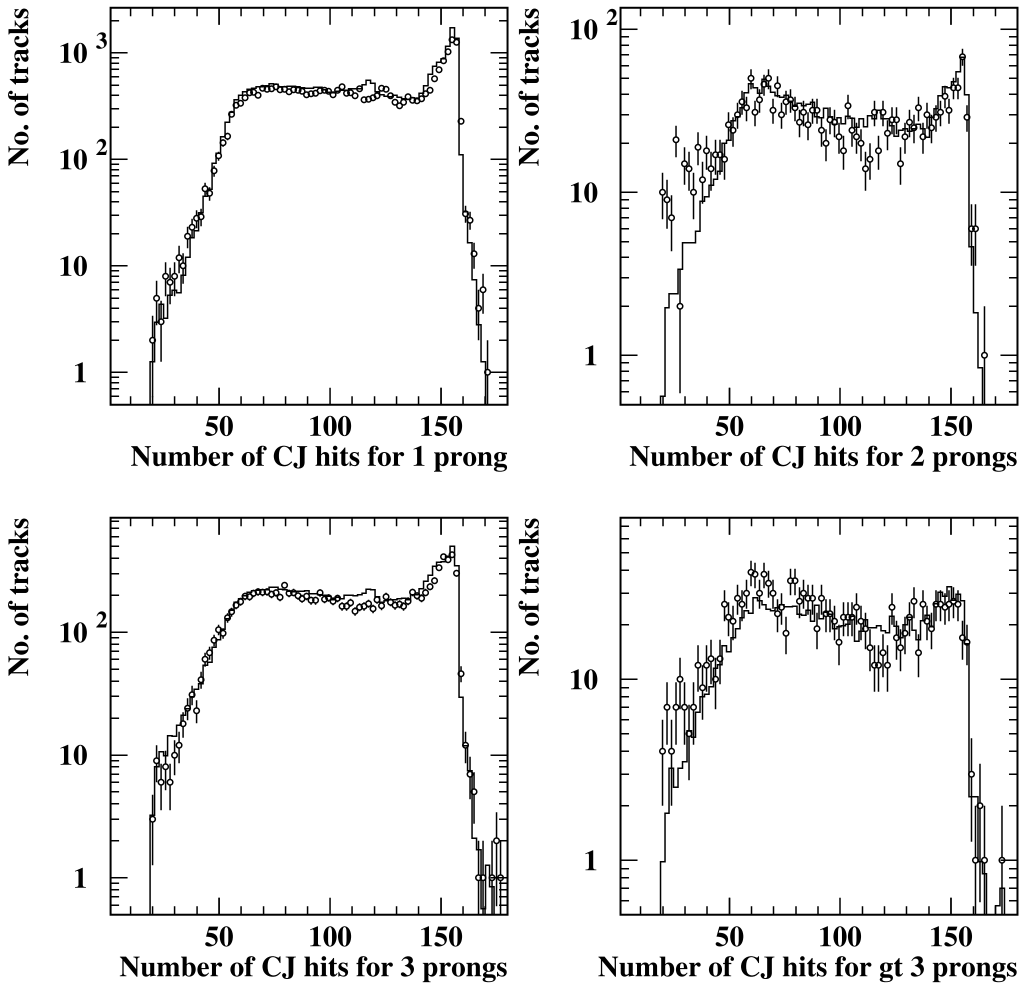

Figure B.6: Number of hits per track in CJ for 94 data and Monte Carlos for the endcap region.

References

[1] F. Halzen and A.D. Martin, 'Quarks and Leptons : An Introductory Course in Modern Particle Physics', John Wiley & Sons (1984).

[2] D.H. Perkins, 'Introduction to High Energy Physics, Third Edition', Addison Wesley (1987).

[3] CDF Collaboration, F. Abe *et al.*, Phys. Rev. Lett. **74** (1995), 2626.
D0 Collaboration, S. Abachi *et al.*, Phys. Rev. Lett. **74** (1995), 2632.
The original 'discovery' papers are referenced in these papers, which describe the latest results.

[4] M.Kobayashi and T.Maskawa, Prog. Theor. Phys. **49** (1973) 652

[5] P.A.M.Dirac, Proc. Roy. Soc **A117** (1928) 610, and also 'Principles of Quantum Mechanics' (1947), Oxford Press.

[6] R.P. Feynman, 'Quantum Electrodynamics', Benjamin (1961).

[7] W.Heisenberg, Z.Phys. **43** (1927) 172,
'Quantum Mechanics' (McGraw and Hill) 3rd Edition (1968)

[8] G.'t Hooft, Nucl. Phys. **B33** (1971), 173; Nucl. Phys. **B35** (1971), 167; Utrecht preprint THU-92/25 (1992).

[9] A. Salam, in : 'Elementary Particle Theory', ed. N. Svartholm, Almqvist and Wikel (1968), 361.
S. Weinberg, Phys. Rev. Lett. **19** (1967), 1264.

[10] S.L. Glashow, Nucl. Phys. **22** (1961), 579.

[11] P.W. Higgs, Phys. Lett. **12** (1964), 132; Phys. Rev. Lett. **13** (1964), 508; Phys. Rev. **145** (1966), 1156.

[12] M.Biasini, OPAL Technical Note TN503, (1997).
D.Abbaneo et al. , LEPEWWG/97-01 (1997).

[13] S. Myers and E. Picasso, *The design, construction and commissioning of the CERN Large Electron-Positron collider*, Contempory Physics, volume **31**, number 6, (1990).

[14] OPAL Collaboration, K. Ahmet *et al.*, Nucl. Instr. and Meth. **A305** (1991), 275.

[15] ALEPH Collaboration, Nucl. Instr. and Meth. **A294** (1990), 121.

[16] DELPHI Collaboration, Nucl. Instr. and Meth. **A303** (1991), 233.

[17] L3 Collaboration, Nucl. Instr. and Meth. **A289** (1990), 35.

[18] Haber and Kane, 'Is Nature Supersymmetric?', Scientific American **254**, 52.
OPAL Collaboration, Phys.Lett **B389** (1996) 616.

[19] P.P. Allport *et al.* (OPAL), Nucl. Instr. and Meth. **A324** (1993) 34.

[20] R.D. Heuer and A. Wagner, Nucl. Instr. and Meth., **A265** (1988), 11.
H.M. Fischer *et al.*, Nucl. Instr. and Meth., **A252** (1986), 492.

[21] H.Breuker *et al.*, CERN-EP/87-97 (1987).

[22] H. Mes et al., Nucl. Instr. and Meth. **A265** (1988) 445.

[23] P. Mattig, *'Photon Energy Resolution in the Lead Glass Calorimeters'*, OPAL Technical Note, TN-324 (1995).

[24] A. Ji-Gang et al., Nucl. Instr. and Meth. **A267** (1988) 386.

[25] A. H. Ball et al., IEEE Trans. Nucl. Sci. **37** (1990).

[26] J. Allison et al., Nucl. Instr. and Meth. **A236** (1985) 284.

[27] G.T.J. Arnison et al., Nucl. Instr. and Meth. **A294** (1990) 431.

[28] OPAL Collaboration, K. Ahmet et al., Nucl. Instr. and Meth. **A305** (1991) 275.

[29] B.E. Anderson *et al.*, IEEE Trans. Nucl. Sci. **41** (1994), 845.

[30] M. Arignon *et al.* (OPAL), Nucl. Instr. and Meth. **A313** (1992) 103.

[31] M. Arginon *et al.*, Nucl. Instr. and Meth., **A333** (1993), 330; CERN-PPE/93-48 (1993).

[32] J. Baines et. al., Nucl. Instr. and Meth. **A325** (1993) 271.

[33] D. Charlton, et al., Nucl. Instr. and Meth. **A325** (1993) 129.

[34] S. Weisz, D. Lellouch, C. Hawkes, M. Redmond and O. Schaille, *The ROPE Users Guide* Version 407, OPAL internal note.

[35] D. Ward and P. Ward, *The GOPAL Primer* Version 131, OPAL internal note.

[36] J. Allison *et al.*, Nucl. Instr. and Meth. **A294** (1990) 431.

[37] S. Jadach, B.F.L. Ward, and Z. Was, Comp. Phys. Comm., **66** (1991) 276; KORALZ

[38] T. Sjostrand, Comp. Phys. Comm. **39** (1986) 347; JETSET

[39] S. Jadach, J.H. Kuhn, and Z. Was, **CERN-TH-5856/90** (1990); TAUOLA.

[40] M.L. Perl, *The Discovery of the Tau Lepton*, **SLAC-PUB-6584** (1994).

[41] M.L. Perl *et al.* (MARK I), Phys. Rev. Lett. **35** (1975) 1489.

[42] Feldman et al., (MARK I) Phys. Rev. Lett. **38** (1977) 117. Cavalli-Sforza et al. Phys. Rev. Lett. **36** (1976) 558.

[43] Burmester et al. (PLUTO) Phys. Lett. **683** (1977) 297

[44] Burmester et al.(PLUTO) Phys. Lett. **683** (1977) 301

[45] BES Collaboration, J.Z. Bai et al., Phys. Rev. Lett. **69** (1992) 3021
BES Collaboration, *'Final Result on the Mass of the τ lepton'* presented at the 27^{th} International Conference on High-Energy Physics in Glasgow, 1994.
BES Collaboration, *'Tau Lepton Experiment at BES Detector.'* presented at the Tau Workshop, Montreux, 1994.

[46] ARGUS Collaboration, H. Albrecht et al., Phys. Lett. **B 292** (1992) 221.

[47] CLEO Collaboration, R. Balest et al., Phys. Rev. **D 47** (1993) R3671.

[48] W.Marciano and A.Sirlin , Phys. Rev. Lett. **61** (1988) 1815.

[49] A.C.Mueller, B.M.Sherrill, Annu. Rev. Nucl. Part. Sci **43** (1993) 457.

[50] J.A. Jaros et al., MARK II Collaboration, Phys. Rev. Lett. **51** (1983) 955.

[51] K. Abe et al., SLD Collaboration, *'Measurement of the Tau Lifetime'*, SLAC-PUB-95-6767 (1995)

[52] OPAL Collaboration, P. Acton et al. *'Measurement of the Tau Lifetime'* CERN-PPE/93-09 Zeit. fuer Physik **C59** (1993) 183-194

[53] OPAL Collaboration, R. Akers *et al.* *'Updated Measurement of the Tau Lifetime'*, CERN-PPE/94-129 Physics Letters **B338** (1994) 497-506

[54] Particle Data Group, Phys. Rev. **D54** (1996).

[55] J. C. Clayton, *Measurement of the Leptonic Branching Ratios of the τ Lepton using the OPAL detector at LEP*, PhD Thesis, University of Birmingham (1995)

[56] R.P.Feynman , Phys. Rev. Lett. **23** (1969) 1415

[57] OPAL collaboration, OPAL Physics Note, PN285 (1997).

[58] F.J.Gilman and S.H.Rhie , Phys.Rev. **D31** (1985) 1066

[59] Fourth International Workshop on Tau Lepton Physics (TAU96), Colorado, September 16 - 19, 1996.

[60] M.A.Thomson, OPAL TN490 - LEP1 Tau Pair Cross Section and Forward-Backward Asymetry, June 1997.

[61] The L3 collaboration, B.Adeva *etal.* , Phys.Lett. **B265** (1991) 451

[62] The DELPHI collaboration, S.Amato *etal.*, DELPHI 97-128 CONF 107 (1997)

[63] The ALEPH collaboration, Contribution to the 28th International conference on High Energy Physics, Warsaw, Poland, 25-31 July 1996

[64] The CELLO collaboration , Phys.Lett. **B222** (1989) 163

[65] Makoto Sasaki et al. , Tau Platform Manual (1993).

[66] OPAL Collaboration, R. Akers *et al.* Physics Note **PN154** (1994).

[67] OPAL Collaboration, R. Akers *et al.* Physics Note **PN172** (1995).

[68] OPAL Collaboration, R. Akers *et al.* CERN-PPE/95-06 (1995).

[69] P.D.Acton et al., Phys. Lett. **B288** (1992) 373.

[70] W.G.Scott , OPAL TN182 (1993)

[71] Herve Lafoux , OPAL TN290 (1995)

[72] Valerie Gibson , OPAL TN367 (1996)

[73] The OPAL Collaboration, R. Akers et al. , Zeit. f. Physik **C68** (1995) 555-567

[74] L. Stumpf, R. Sobie , OPAL TN319 (1995)

[75] B.K.Heltsley , Nucl.Phys B(proc.suppl)40 (1995) 413.

[76] S.Gentile, M.Pohl, CERN-PPE/95-147 (1995)

[77] The CELLO collaboration, H.J.Behrend et al., Phys. Scr. **23** 610 (1981)

[78] The CLEO Collaboration, Y.Kubota et al., Nucl.Inst.Methods.Phys.Res. **A320** 66 (1992)

[79] Phys Rev Lett **75**, 3809 (1995). Phys Rev Lett **73**, 934 (1994).

[80] The ALEPH collaboration, D.Buskulic et al., Z.Phys. **C70** 579 (1996)